DOE/ER/13797--T1

Final Report

to

The Department of Energy

for

a program of research entitled:

HIGH-FREQUENCY ACOUSTIC SENSORS FOR OPERATION IN A GASEOUS MEDIUM

(G. L. Report No. 4979)

Contract No. DE-FGO3-87ER13797

Expiration: August 31, 1990

RECEIVED
OCT 28 1994
OSTI

Principal Investigator:
Gordon S. Kino

Edward L. Ginzton Laboratory
Stanford University
Stanford, California 94305-4085

MASTER

DISTRIBUTION OF THIS DOCUMENT IS UNLIMITED

DISCLAIMER

Portions of this document may be illegible in electronic image products. Images are produced from the best available original document.

Abstract

Photothermal microscopy is a technique for measuring thermal properties on a small scale by using focussed laser beams as heat sources and as temperature probes. Typically used for nondestructive evaluation (NDE) of materials, its main advantage is its ability to measure types of flaws that are not visible optically or acoustically. Examples of these kinds of defects include disbonds and poor adhesion in layered media, subsurface cracks or crystal damage in opaque solids, and electrical defects in active circuits. Because of the optical nature of photothermal microscopy, sub-micron resolutions can be obtained in many of these thermal measurements.

The greatest limitation of these systems is their relatively poor signal-to-noise ratios and, consequently, slow imaging speeds. To circumvent this problem, a variety of approaches to the detection of thermal waves has been pursued in recent years. This thesis compares the relative merits of a common class of techniques that rely on direct observation of physical changes in the heated sample, including a novel approach to interferometric measurement of the thermal expansion. It is found that the optimum approach depends not only on the physical properties of the sample being studied, but also upon the resolution of the experiment and the damage threshold of the specimen. These points are illustrated in an assortment of examples of photothermal NDE.

Finally, this dissertation describes our applications of photothermal microscopy to the study of the anisotropic thermal properties of the new high-T_c superconductors. Because of their micron resolution, photothermal techniques are well suited for studying single-crystal specimens which tend to be too small or irregularly shaped for conventional bulk methods. By adding a high-vacuum cryostat to the microscope, we have been able to study the influence of the superconducting transition on the thermal conductivity. Our measurements of the anisotropic thermal conductivity demonstrate that the heat flow along

the superconducting planes is enhanced below the transition, and that no such enhancement exists in the non-superconducting direction. These effects can be explained as a product of the electron-phonon coupling. Furthermore, we present evidence that thermal and optical changes in these materials can begin as much as 10 or 15 K above the superconducting transition.

Acknowledgements

There are a number of people I wish to thank for their valuable contributions to this thesis. I would like to thank Professor Gordon Kino for his support and steady supply of good ideas over the years. I am fortunate to have worked for someone who not only had such reliable physical intuition, but who was so personable and enthusiastic as well. I also wish to thank Professor Pierre Khuri-Yakub for his valuable assistance in the design and operation of these experiments. I am just one of the many people at the Ginzton Laboratory who have benefitted from his practical experience and acute engineering sense. Aharon Kapitulnik also deserves special recognition for his assistance in the high-T_c superconductor studies. Without his physical insight and expertise in the field (not to mention his endless supply of high-quality samples) this work would not have been possible.

I would also like to thank a number of other people including Dave Mitzi for supplying the single-crystal bismuth superconductors, Steve Anlage for the YBa_2Cu_3O films, and Al Rosencwaig for originally drawing our attention to the potential of thermal-wave microscopy in the study of these materials. I am also grateful to Lance Goddard and Tom Carver for constructing many of the samples for our NDE studies, and to the students of the low-temperature-physics group for patiently obliging my "occasional" use of their equipment. Of course, I especially thank the many students of the Kino/Khuri-Yakub research group for both their technical assistance and for their friendly companionship. It has been a real pleasure working with them.

Finally, I wish to thank my family, and especially my wife Andrea, for their love, support, and encouragement.

Contents

Abstract iii

Acknowledgements v

List of Illustrations ix

Chapter 1: Introduction 1

References 7

Chapter 2: Theory of the thermal and acoustic response of a periodically heated material 8

2.1 Introduction 8

2.2 The thermoacoustic wave equations 9

2.3 One-dimensional solution 10

2.4 Three-dimensional solution 16

2.4.1 Temperature profile 17

2.4.2 Surface displacement 21

2.5 Thermal effects of the environment 30

References 33

Chapter 3: Experimental configuration and sensitivities of Various Detection Schemes 34

3.1 Introduction 34

3.2 Experimental layout 35

3.3 Objective lenses 38

Contents (continued)

3.4 Theoretical sensitivities of the various methods 45

3.5 Comparison of signal strengths 49

3.6 Experimental check of the sensitivity 53

References 56

Chapter 4: Photothermal NDE 57

4.1 Introduction 57

4.2 Imaging of disbonds and cracks 58

4.3 Imaging of electrical samples 65

4.4 NDE of silicon flip-chip devices 76

References 84

Chapter 5: Photothermal measurements of high-T_c superconductors 85

5.1 Introduction 85

5.2 Motivation 87

5.3 Anisotropy 91

5.4 Spot-size effects 98

5.5 Room-temperature results 99

5.6 Non-linear effects at low temperatures 108

5.7 The low-temperature environment 111

5.8 Low-temperature thermal conductivity of single-crystal Bi-Sr-Ca-Cu-O materials 115

5.9 Behavior above T_c 119

Contents (continued)

5.10 Suggestions for future research 126

References 128

Appendix: Numerical evaluation of the temperature and displacement profiles 130

DISCLAIMER

This report was prepared as an account of work sponsored by an agency of the United States Government. Neither the United States Government nor any agency thereof, nor any of their employees, makes any warranty, express or implied, or assumes any legal liability or responsibility for the accuracy, completeness, or usefulness of any information, apparatus, product, or process disclosed, or represents that its use would not infringe privately owned rights. Reference herein to any specific commercial product, process, or service by trade name, trademark, manufacturer, or otherwise does not necessarily constitute or imply its endorsement, recommendation, or favoring by the United States Government or any agency thereof. The views and opinions of authors expressed herein do not necessarily state or reflect those of the United States Government or any agency thereof.

List of Illustrations

Figure ..... page

1.1 Sketch of the various responses of a sample to periodic heat 2

1.2 The three sample-based techniques used for the detection of the local temperature 4

2.1 Calculated surface temperature as a function of the modulation frequency 21

2.2 Profiles of the temperature in the two frequency extremes 21

2.3 Amplitudes of the surface displacement, surface temperature, and slope as a function of the modulation frequency 29

2.4 Resolution of the three methods as a function of frequency 30

3.1 Photograph of the photothermal microscope 36

3.2 Schematic of the microscope 36

3.3 The deflection method for the measurement of the surface displacement 38

3.4 The Wollaston and Mirau interferometers used for the measurement of surface displacement 39

3.5 Theoretical and measured phase noise in a 250 Hz bandwidth as a function of the static path-length difference 41

3.6 Optical intensity at the photodetector measured as a function of the axial position of the Mirau interferometer 44

3.7 Theoretical calculation of the Mirau depth response 45

3.8 Displacement signal for a 3.4×10^{-3} Å vibration, optical noise level, and Johnson noise level from the split-transducer calibration 54

3.9 Displacement as measured by the Mirau interferometer demonstrating sample resonances 55

4.1 Effect of a perfectly-insulating crack on the temperature profile 58

4.2 Theoretical plot of the AC temperature as the lasers are scanned over a crack 59

List of Illustrations (continued)

Figure ..... page

4.3 Theoretical plot of the AC surface displacement as the lasers are scanned over a crack 60

4.4 Measured surface displacement as the lasers are scanned over a crack 61

4.5 Displacement signal, using the Wollaston prism detector, showing the acoustic effects of a crack 62

4.6 Optical and photothermal images of the ac-plane in a single-crystal $Bi_2Sr_2CaCu_2O_x$ fiber 63

4.7 Optical and thermal images of two gold films on a silicon substrate 64

4.8 Thermal image of a blister in the gold film 65

4.9 Sketch of the sample used in the demonstration of electrical-flaw detection, and the measured surface displacement in the vicinity of the flaw 67

4.10 Color images showing the extent of the heated region 68

4.11 Frequency behavior of the surface displacement at the peak shown in Figure 4.9b 69

4.12 Sketch of narrow conducting strips to be imaged at high resolution 70

4.13 Profiles of measured AC reflectivity of the device shown in Figure 4.12 71

4.14 Theoretical calculation of the AC temperature profile at the three frequencies 72

4.15 Two-dimensional optical and thermal images of the bar pattern 73

4.16 Optical and thermal images of the same device as in Figure 4.15 but taken using an argon laser probe rather than the usual diode laser probe 74

4.17 Theoretical calculation of the AC surface displacement at 200 kHz 75

4.18 Measured displacement (Mirau method) at 200 kHz 75

4.19 Schematic of the silicon flip-chip device 77

List of Illustrations (continued)

Figure ..... **page**

4.20 Acoustic images of the flip-chip device 79

4.21 Thermal image of a single row of solder bumps 80

4.22 Sequence of thermal images of the region near the hot spot in the center of Figure 4.21 81

4.23 Thermal phase lag from a subsurface flaw 83

5.1 Thermal conductivity of $La_{2-x}Sr_xCuO_4$ and $YBa_2Cu_3O_{7-\delta}$ as a function of temperature (reprinted with permission from [5.1]) 88

5.2 Lattice thermal conductivity vs. T/T_c from BRT theory (reprinted with permission from [5.2]) 89

5.3 Theoretical amplitude and phase contours of the temperature profile in an anisotropic medium 96

5.4 Radial dependence of the temperature profile along both axes of an anisotropic material and in an isotropic material 97

5.5 Optical and photothermal images of a thin polycrystalline film of Y-Ba-Cu-O . 100

5.6 Schematic of the phase measurement 101

5.7 Measured thermal phase lag along both axes of single-crystal quartz 102

5.8 Photomicrographs of the ac-plane of a typical single-crystal Bi-Sr-Ca-Cu-O chip and a single-crystal fiber 104

5.9 Room-temperature thermal diffusivity along the Cu-O planes of single-crystal Bi-Sr-Ca-Cu-O 105

5.10 Room-temperature thermal diffusivity across the Cu-O planes of single-crystal Bi-Sr-Ca-Cu-O 106

5.11 Phase lag in the ac-plane as a function of the crystal orientation 107

5.12 Schematic of the high-vacuum cryostat 113

List of Illustrations (continued)

Figure ..... page

5.13 Thermal phase lag, as a function of temperature, along the Cu-O planes of an 88 K - phase Bi-Sr-Ca-Cu-O chip 115

5.14 Thermal diffusivity, as a function of temperature, along the Cu-O planes of an 88 K - phase Bi-Sr-Ca-Cu-O chip 116

5.15 Thermal conductivity as determined from the diffusivity data of Figure 5.14 and published heat capacity curves [5.13,5.14] 117

5.16 Thermal conductivity of the Cu-O planes measured on a second specimen from the same 88 Kelvin T_c batch as above 118

5.17 The anisotropic thermal conductivity of the 88 K - phase Bi material 119

5.18 Amplitude of the photothermal signal, as a function of temperature, from the Cu-O planes of 88 K - phase Bi-Sr-Ca-Cu-O 120

5.19 Amplitude of the photothermal signal from the Cu-O planes of a 72 K - phase Bi-Sr-Ca-Cu-O chip 121

5.20 Amplitude of the photothermal signal from the Cu-O planes of an 80 K - phase Bi-Sr-Ca-Cu-O chip 122

5.21 Simultaneous measurement of the resistivity and the photothermal amplitude .. 123

A.1 Cross section of the effective beam profile for heating near a thermally-insulating crack 131

A.2 The space and the spatial-frequency domains involved in the transform expressions 132

Chapter 1

Introduction

As electronic device technology has approached ever smaller dimensions, the need for non-destructive evaluation (NDE) tools with higher resolutions has increased. In some of the more traditional areas of NDE, such as optical and acoustic microscopy, resolutions have been improved by increasing frequencies [1] or by employing novel, near-field techniques [2,3]. The past decade has also seen the refinement of scanning electron microscopy and the introduction of probe-based tunneling microscopies that can characterize materials down to atomic scales [4].

A push for finer-resolution thermal measurements has occurred as well. Employing periodic heat sources, thermal-wave microscopy can be used to measure the thickness and adhesion of thin films, to locate cracks, flaws, and other thermal inhomogeneities in devices, and to characterize the basic thermal (and sometimes electronic) properties of the material itself. To achieve high resolutions, focussed laser beams are used both as heat sources and as temperature probes. Thus the lateral resolution of thermal microscopy can approach that of optical microscopy, i.e. about a micron or less. Furthermore, the highly dispersive and strongly damped nature of thermal waves gives us great control over the spatial extent of our measurement. Films as thin as 100 Å have been characterized using high-frequency thermal waves [5,6], while low-frequency experiments probe deep into the bulk, revealing the thermal properties of the underlying substrate [7].

The versatility and high resolution of thermal-wave microscopy is offset by the very weak nature of the photothermal signals which are based on small perturbations either in the sample itself or in the surrounding medium. Figure 1.1 shows the typical responses of a laser-heated solid in an air environment. Since these effects are weak, every experiment involves a difficult compromise between signal-to-noise and imaging speed. In fact, it is

for this reason that the measurements are performed with periodic signals; lock-in detection is essential. The situation is worse at high resolutions where the intensities of the tightly focussed pump and probe beams must be curtailed to avoid damaging the sample.

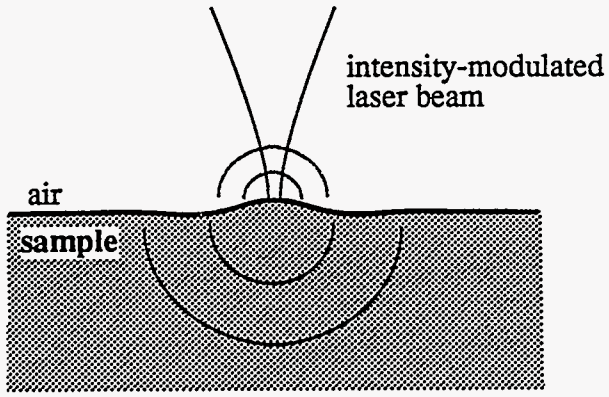

Figure 1.1 Sketch of the various responses of a sample to periodic heat, including thermal and acoustic wave generation in both the sample and the air, and local thermal expansion of the sample.

Because of the weak nature of photothermal signals, a vast array of detection schemes have been developed in the last few years, each with its own particular advantages and drawbacks. We can broadly categorize these schemes into two groups, those that measure temperature by measuring changes in a coupling medium (usually air) in contact with the sample, and those that monitor the sample directly. Neither type is universally superior to the other; the best approach depends on the properties of the particular sample, the type of information sought, the resolution, and various other constraints such as damage thresholds and environmental limitations. Ideally, the photothermal microscope has enough flexibility to adapt to the situation at hand. Thus it is important to have a firm theoretical understanding of the noise limitations of competing methods.

Among the more common methods of the first type are photothermal deflection in air (or "Mirage Effect" microscopy [8]), gas microphone cells [9], and acoustic detection in air using focussed transducers [10]. The first method infers the temperature of the

sample by measuring the temperature of the air in contact with it. Since the heated air has a slightly lower refractive index, an optical probe is deflected by the thermal gradients. To increase the sensitivity, the probe beam is usually directed parallel to the surface so that a small deflection can be amplified over a long distance. The other two methods measure the acoustic waves caused by the thermal expansion of the air above the sample. The main advantage of all of these techniques is that they are insensitive to vibrations of the sample. (The thermal expansion coefficient of air is at least 100 times as great as that of most solids so that sample vibrations are a small contribution to acoustic waves in the air.) This is by no means a trivial advantage; spurious signals and noise caused by acoustic resonances in the sample can easily overwhelm the desired signal in any method that is sensitive to these effects. A disadvantage of air-coupled measurements is that they tend to be somewhat inflexible. In the first two methods, the resolution is determined by the size of the thermal source. Therefore, they cannot be used to check electrically heated samples for which the size, or even the number, of the sources is often unknown. In the third method, the detection probe has better resolution, about 300 μm, but the frequency range of the measurement is limited by the severe acoustic impedance mismatch between the air and the transducer. Of course, none of these methods would work in a vacuum environment (which we will need for the studies in Chapter 5).

The second group of photothermal methods include modulated reflectance, surface displacement and deflection spectroscopy, and infrared radiometry. If the refractive index of the material is sufficiently temperature dependent, the modulated reflectance method is the most direct; the periodic surface temperature gives rise to a periodic fluctuation in a reflected probe beam (see Figure 1.2a). This method, pioneered by Rosencwaig [11], has the advantage of being more straightforward to interpret. For this reason, we use this method in the high-temperature superconductor studies in Chapter 5. The displacement and deflection methods, Figure 1.2b and 1.2c, are instead based on the thermal expansion of the heated material. This expansion is measured either interferometrically (displacement) or

by monitoring the angular scattering off of the side (deflection). Despite the extreme sensitivities that can be achieved with interferometry, the displacement method is susceptible to sample resonances and so has had limited usefulness in the past. However, we have developed a novel approach to displacement microscopy that circumvents this problem. We will show that this method can be competitive in a practical sense, especially at slightly relaxed resolutions of a few microns or more. We use all three of the above techniques in this work. The final method, IR radiometry, is an entirely different branch of thermal microscopy and will not be used. For completeness, a brief theoretical comparison of IR radiometry with the other methods is included in Appendix B. In short, this technique would not fare well in the majority of our applications due to its limited resolution and equally poor sensitivity.

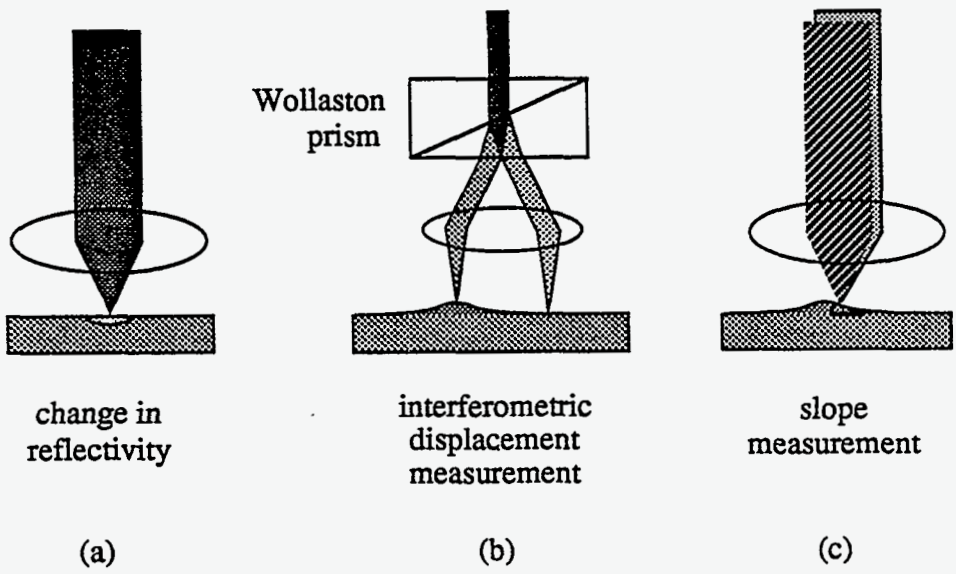

Figure 1.2 The three sample-based techniques used in this thesis for the detection of the local temperature.

Since we will be using a variety of photothermal methods, we begin this thesis with a detailed analysis of the thermal and acoustic behavior of a periodically heated material, with emphasis on the importance of the various thermal and optical parameters (such as

conductivity, heat capacity, and the thermal expansion coefficient). The theory for one-dimensional and point-source geometries is well established in the literature [12]; we extend the theory to cover thermal sources of arbitrary shape and size. This intermediate range is important when making quantitative measurements with real systems.

Chapter 3 contains a description of our experimental arrangement. Special emphasis is placed on the noise limitations of the various methods. Using the photothermal theory of Chapter 2, we derive expressions that compare the relative sensitivities of each method under arbitrary operating conditions.

In Chapter 4 we present a sampling of the NDE capabilities of our system. Where possible, the differences between the three approaches are demonstrated. Particular emphasis is placed on the location of electrical flaws, for which these photothermal methods are particularly well suited. The final example, measurement of bond quality in a semiconductor flip-chip device, is a good demonstration of the types of information uniquely available through photothermal microscopy.

The final chapter describes our studies of the thermal properties of high-temperature superconductors. In many ways, photothermal microscopy is ideally suited for the study of these materials, since single-crystal specimens tend to be small and irregularly shaped. The emphasis in this chapter is much more quantitative than in the NDE studies of Chapter 4. Hence we begin Chapter 5 by modifying our theory to include the effects of crystal anisotropy and of using a probe of finite size. We then present our measurements of single-crystal $Bi_2Ca_2Sr_1Cu_2O_x$ superconductors. By enclosing the experiment in a high-vacuum, low-temperature environment, described in Section 5.7, we were able to extend the measurements to the transition region. We conclude with our results on the effects of the superconducting transition on the amplitude and phase of the photothermal signal, and its implications about the nature of the electron-phonon scattering. We demonstrate a strong enhancement in the thermal conductivity in a direction along the superconducting planes of these layered materials. This enhancement is in accord with measurements made

by other researchers on polycrystalline materials, however, by conducting the measurement on single-crystal specimens, we avoid the complications of mixed orientations and grain-boundary scattering present in the ceramic measurements. Furthermore, we show for the first time that such an enhancement does not exist in the direction normal to the superconducting planes. The results of these measurements demonstrate a coupling between the phonons and the electrical carriers that is clearly affected by the superconducting transition. We have also discovered that thermal and optical changes can begin as much as 10 or 15 K above T_c, including an abrupt change in the temperature dependence of the refractive index, and an early onset of the enhancement in the thermal conductivity. These effects may be the result of thermal fluctuations in the pairing and further measurements could provide valuable insight into the physical nature of the pairing.

Chapter 1 References

1. B. Hadimioglu, L.J. La Comb Jr. D.R. Wright, B.T. Khuri-Yakub, and C.F. Quate, "High efficiency, multiple layer ZnO acoustic transducers at millimeter-wave frequencies," *Appl. Phys. Lett.* **50** (23), 1642 (1987).
2. A. Lewis, M. Isaacson, A. Harootunian, and A. Muray, "Development of a 500Å spatial resolution light microscope," *Ultramicroscopy* **13** (3), 227 (1984).
3. E. Betzig, M. Isaacson, and A. Lewis, "Collection mode near-field scanning optical microscopy," *Appl. Phys. Lett.* **51** (25), 2088 (1987).
4. H.K. Wickramasinghe, "Scanned-probe microscopes," *Scientific Am.* **261** (4), 98 (1989).
5. R. Stearns, *Photoacoustic Techniques for the Quantitative Characterization of Materials*, Ph.D. Dissertation, Stanford University, 1985.
6. A. Rosencwaig, J. Opsal and D. Willenborg,"Thin-film measurementrs with thermal waves," *Appl. Phys. Lett.* **43** (2), 166 (1983).
7. A. Rosencwaig, "Thermal-wave imaging," *Science* **218** (1982).
8. A. C. Bocarra, D. Fournier, and J. Badoz, "Thermo-optical spectroscopy: Detection by the 'mirage effect',",*Appl. Phys. Lett.* **36**, 130 (1980).
9. A. Rosencwaig, "Photo-acoustic spectroscopy of solids," *Rev. Sci. Instrum.* **48**, 1133 (1977).
10. R. Stearns and G.S. Kino, "Photoacoustic techniques for the measurement of electronic properties of semiconductors," in *Photoacoustic and Thermal-Wave Phenomena in Semiconductors,* Ed. A. Mandelis, New York: North-Holland, 1987.
11. A. Rosencwaig, J. Opsal, W.L. Smith and D.L. Willenborg, "Detection of thermal waves through optical reflectance," *Appl. Phys. Lett.* **46**, 1013 (1985).
12. J. Opsal and A. Rosencwaig, "Thermal-wave depth profiling: Theory," *J. Appl. Phys.* **53** (6), 4240 (1982).

Chapter 2

Theory of the Thermal and Acoustic Response of a Periodically Heated Material

2.1 Introduction

This chapter lays the theoretical foundation for the experiments that follow. As indicated in the introduction, there are a vast number of effects to consider when the sample is heated. Of course, the most direct response to the driving flux is an increase in temperature, and with it, a change in any temperature-sensitive property such as the refractive index. The thermal expansion of the material subsequently generates stresses and strains, causing the material to deform. If the heat source is optical, it may alter the electronic properties of the material as well. Examples include the generation of free carriers in semiconductor materials, or the destruction of Cooper pairs in superconductors.

To complicate matters further, not only is the sample heated, but so also is any ambient medium, such as air, in contact with the it. Since all of these changes may affect our optical probe, we need a firm understanding of their relative magnitudes under various conditions. We would like to know if we can design experiments that respond to only one effect, so that our data can be more easily interpreted. We will find that the magnitude of our photothermal signal depends on the effect we choose to monitor and the value of various thermal parameters such as thermal conductivity and heat capacity. The modulation frequency also plays an important role in determining the dependence of these signals on the thermal parameters.

In this thesis, we restrict our attention to those effects that occur in the sample itself; we do not rely on a coupling medium to infer the temperature of the sample. We do so because it is possible to obtain adequate results without the further complexity of coupling

through air; in fact, the most interesting samples we will examine have additional constraints that render the use of a coupling medium either ineffective or impossible. Therefore, the following theory describes the temperature profiles and surface displacements of the samples themselves. We examine the relative strengths of the various sample-based approaches and evaluate their dependence on the thermal conductivity, the heat capacity, the operating frequency, and the size of the heat source. For completeness, a brief discussion of the contribution to the signal from small fluctuations in the air is also included.

2.2 The Thermoacoustic Wave Equations

The thermal and acoustic responses of a heated material are governed by a pair of coupled differential equations for the temperature, θ, and the local displacement, $\mathbf{u}$. For an isotropic material the equations are [1]

$$\kappa\nabla^2\theta - C\frac{\partial\theta}{\partial t} - T_o\,\alpha\,(3\lambda+2\mu)\frac{\partial}{\partial t}\nabla\bullet\mathbf{u} = h \tag{2.1}$$

$$\mu\nabla^2\mathbf{u} + (\lambda+\mu)\,\nabla\nabla\bullet\mathbf{u} - \rho\frac{\partial^2\mathbf{u}}{\partial t^2} - \alpha\,(3\lambda+2\mu)\,\nabla\theta = \mathbf{M} \tag{2.2}$$

where κ, ρ, C, T_o, and α are the thermal conductivity, density, heat capacity per volume (density times the specific heat), ambient temperature and the thermal expansion coefficient, and λ and μ are the Lamé constants. The driving terms, h and $\mathbf{M}$, on the right hand sides represent the heat and momentum flux delivered to the material by the heating source. In this work, all external sources are optical, so the force term $\mathbf{M}$ (arising from the radiation pressure) is negligible.

A term by term examination of these equations reveals that they consist of the standard thermal diffusion equation and the acoustic wave equation, each with an additional

coupling term due to the thermal expansion. These extra terms come from the fundamental constitutive relations between the stress, strain, and temperature. Known as the Duhamel-Neumann relations, they are derived by a free-energy analysis of the heated material [1],

$$T_{ij} = 2\mu S_{ij} + (\lambda \sum_{1}^{3} S_{ii} - (3\lambda+2\mu)\alpha\theta)\, \delta_{ij} \tag{2.3}$$

where T_{ij} and S_{ij} are the stress and strain tensors. Note that the temperature only affects the longitudinal constitutive relation; thermal expansion is purely dilational.

A full solution to the coupled thermoacoustic equations is quite complex, and for most boundary conditions the calculations have to be done numerically (Ref. 2 outlines the general form of a Green's function approach). Fortunately, for most solids the equations can be simplified considerably by neglecting the displacement term in the thermoacoustic equation (2.1) for the temperature (we will justify this approximation below). We can then use (2.1) to solve directly for the temperature profile, given the heat source, and then use this profile in (2.2) to calculate the displacement. The expressions we derive will more clearly illustrate the dependence of temperature and displacement on the sample properties and operating conditions. We will find that our ability to measure thermal properties depends on the effect we choose to monitor, the size of our excitation, and the modulation frequency.

2.3 One-dimensional Solution

To determine the validity of the decoupled-equation approximation mentioned in Section 2.2, we examine a case for which a simple analytic solution exists. The simplest case is a semi-infinite slab heated uniformly at its surface. The solutions obtained will also demonstrate some of the characteristics of thermal waves, such as their highly localized nature and their phase versus frequency behavior. In a real measurement, the one

dimensional solutions pertain to any situation in which the spatial extent of the heating spot is much greater than the thermal wavelength (i.e. at high frequencies).

We proceed by assuming that the approximation holds. We can then solve directly for θ, use (2.2) to solve for **u**, and finally substitute **u** back into the thermal diffusion equation, (2.1), to determine the error in neglecting the acoustic term in our calculation of θ.

Neglecting the thermal expansion term, the homogeneous one-dimensional equation for the temperature generated by a sinusoidal heat source, $e^{j\omega t}$, is

$$\frac{\partial^2\theta}{\partial z^2} - j\frac{\omega C}{\kappa}\theta = 0 . \tag{2.4}$$

A quantity we will use throughout this work is the thermal propagation constant,

$$k_t \equiv (1+j)\sqrt{\frac{\omega C}{2\kappa}} = (1+j)\sqrt{\frac{\omega}{2D}} \tag{2.5}$$

where D is the thermal diffusivity. With this definition, the diffusion equation resembles Helmholtz's equation (except that k_t^2 is imaginary) and can be written as

$$\frac{\partial^2\theta}{\partial z^2} - k_t^2\theta = 0 , \tag{2.6}$$

which has solutions of the form

$$\theta = \theta_o e^{\pm k_t z} . \tag{2.7}$$

For thick slabs, only the $-k_t$ solution is bounded at large z and is therefore the only physical solution.

This simple formula contains the basic characteristics of thermal waves. The complex nature of k_t causes the wave to decay in a distance on the order of length $\sqrt{2D/\omega}$. For most materials this number is quite small, typically about 1 μm for

frequencies of a few megahertz. (By comparison, the acoustic wavelength at the same frequencies is about a millimeter.) Hence, thermal-wave techniques can be used to characterize thin films without needing to know the properties of the substrate. With sources of finite size, this exponential decay also confines the thermal wave laterally, allowing high resolution in all three dimensions.

These short thermal wavelengths are also useful in phase measurements over small distances. For example, film thicknesses can be measured at moderate frequencies by measuring the thermal phase lag through the film. In Ref. 3, the thickness of SiO_2 films on silicon were measured with a 2 MHz photoacoustic system to a thickness resolution of about 50 Å. We will take advantage of the small thermal wavelength in the application discussed in Chapter 5 where we measure the anisotropic thermal conductivity of small single-crystal high-T_c superconductors.

Returning to our one-dimensional example, we proceed by assuming that the heat source is absorbed entirely at the surface. This assumption means that we ignore terms of order $e^{-z/\delta}$ where δ is is the absorption depth, typically on the order of 100 Å to 1000 Å in opaque solids. Except for silicon, which has an optical absorption depth of about 5000 Å at 514 nm, this length is negligible compared to the thermal and acoustic wavelengths in our work, and can be assumed to be zero. (For a one-dimensional treatment that includes the effects of absorption depth see Ref. 4.) Therefore, the homogeneous solutions still apply, with the driving term becoming a boundary condition at the surface:

$$-\kappa \left.\frac{\partial\theta}{\partial z}\right|_{z=0} = I_o e^{j\omega t} \tag{2.8}$$

where I_o is the intensity of the heat input. Solving for the surface temperature, θ_o, gives

$$\theta_o = \frac{I_o}{\kappa k_t} = \frac{I_o}{\sqrt{\omega C \kappa}} e^{-j\pi/4} . \tag{2.9}$$

In the one-dimensional, or high-frequency, limit, (2.9) indicates that the periodic surface temperature depends on both thermal constants, κ and C. The amplitude decreases as $\omega^{1/2}$ and has a phase lag of 45° behind the source. Later in this chapter we will examine low-frequency, three-dimensional sources and find that their response depends on different parameters. First, we continue with our verification of the uncoupled-equation approximation.

In the one-dimensional case, only a purely longitudinal acoustic wave is generated. This is governed by (2.2), rewritten as

$$\frac{\partial^2 u_z}{\partial z^2} + k_l^2 u_z = \alpha \left(\frac{3\lambda+2\mu}{\lambda+2\mu}\right) \frac{\partial \theta}{\partial z} \tag{2.10}$$

where $k_l \equiv \omega/\sqrt{(\lambda+2\mu)/\rho}$ is the propagation constant of a longitudinal acoustic wave. Substituting the temperature profile, (2.7), into the above and solving for u_z gives

$$u_z = Ae^{-jk_l z} - \alpha' \frac{k_t}{k_t^2 + k_l^2} \theta_o e^{-k_t z} \tag{2.11}$$

where θ_o, again, is the surface temperature given by (2.9) and α' is defined as $\alpha\left(\frac{3\lambda+2\mu}{\lambda+2\mu}\right)$.

The first term of this expression describes the thermally generated acoustic waves. The second represents the local thermal expansion. The amplitude of the acoustic term, A, depends on the boundary condition at the surface of the sample. The most common case is a stress-free surface, for which the boundary condition is

$$T_{zz} = (\lambda+2\mu) S_{zz} - \alpha (3\lambda+2\mu) \theta_o = 0, \tag{2.12}$$

or

$$\left.\frac{\partial u_z}{\partial z}\right|_{z=0} = \alpha' \theta_o \ . \tag{2.13}$$

After some algebra we get the final form of u_z:

$$u_z = \frac{\alpha'}{k_t^2 + k_l^2} \theta_o \left(jk_l e^{-jk_l z} - k_t e^{-k_t z} \right) . \tag{2.14}$$

This solution consists of a +z travelling acoustic wave and an exponentially damped expansion near the surface. At the surface the expansion term is greater than the travelling-wave term by the ratio

$$\left| \frac{k_t}{k_l} \right| = \frac{\sqrt{\omega C/\kappa}}{\omega/v_l} \cong 10^5 - 10^6 \ / \sqrt{f} \tag{2.15}$$

for typical solids (v_l is the longitudinal acoustic wave velocity). Thus for frequencies less than about 100 GHz, the surface displacement is dominated by thermal expansion. We will find in Section 2.5 that this is true for any size heating spot; the surface displacement is determined mainly by the local expansion. It is for this reason that displacement interferometry can have fine resolutions; the acoustic signal far from the heat source is much weaker than the highly-localized thermal expansion.

Since $k_t >> k_l$, the expression for the surface displacement can be simplified to

$$u_z(0) = -\frac{\alpha' \theta_o}{k_t} = \frac{\alpha' I_o}{\omega C} e^{+j\pi/4} . \tag{2.16}$$

Unlike temperature, the high-frequency surface displacement is *independent* of the thermal conductivity. This is because the displacement depends on an integral of the temperature throughout the volume. Even though the surface temperature decreases at high thermal

conductivities, the extent of the heated volume increases and the two effects cancel. For low-frequency (or small) sources the spatial extent of the heated area is determined by 1/r effects, rather than the exponential decay, and the dependence on κ returns. Hence, we reach an important conclusion concerning two of our methods: when trying to measure the thermal conductivity, displacement techniques are useless whenever the heated area exceeds the thermal wavelength.

Finally, to complete our examination of the decoupled-equation approximation, we substitute the formula for u_z back into the thermal equation to check the relative importance of the expansion term. The resulting equation is

$$\frac{\partial^2\theta}{\partial z^2} - k_t^2\theta - j\frac{\omega T_o\alpha^2}{\kappa}\frac{(3\lambda+2\mu)^2}{\lambda+2\mu}\frac{\partial u_z}{\partial z} = 0 \tag{2.17}$$

The solution, given a surface temperature of θ_o, can be shown to be

$$\theta = \theta_o e^{-k_t z} + \theta_o\left(\frac{j\omega T_o\alpha^2}{\kappa}\frac{(3\lambda+2\mu)^2}{\lambda+2\mu}\frac{1}{k_t^2+k_l^2}\right)$$

$$\times\left\{\frac{k_l^2}{k_t^2+k_l^2}\left(e^{-k_t z} - e^{-jk_l z}\right) - \frac{k_t}{2}z\,e^{-k_t z}\right\} \tag{2.18}$$

The first term is the solution with which we started. The second term represents the acoustic perturbation to the temperature. Again, we will always be operating at far less than 100 GHz so that $k_t >> k_l$. Therefore, the second term is of order

$$\frac{T_o\alpha^2}{C}\frac{(3\lambda+2\mu)^2}{\lambda+2\mu} \tag{2.19}$$

We want this term to be much less than 1. In solids at room temperature, the heat capacity, C, approaches $3nk_B$ or about 2×10^6 J/m^3°C. The expression involving the acoustic constants is typically about 5×10^{11} N/m^2 [5], and the thermal expansion coefficient is usually around 10^{-5} /°C. Thus the acoustic perturbation term is on the order of 8×10^{-3}. The solids that come closest to violating the approximation are metals with large thermal expansion coefficients for which the perturbation is still only about 5%. It is interesting to note that for air at atmospheric pressure the acoustic term is 0.4, and the decoupled-equation approximation is questionable. This has important implications for methods that rely upon the detection of thermal or acoustic waves generated in an ambient above the surface of the sample (as in, for example, "Mirage Effect" detection or in photoacoustic cells).

2.4 Three-dimensional Solution

The results of the one-dimensional analysis above are useful for demonstrating the basic nature of thermal waves and for checking the validity of the decoupled-equation approximation. They also serve as a reference for the behavior of the material in the high-frequency limit (thermal wavelength much less than the heating spot size). In many instances, however, it is better to operate in the low-frequency regime where the response of the sample depends on different material constants. For example, as shown above, low frequencies must be used if the thermal conductivity is to be measured with a displacement technique. Another incentive for switching to low frequencies is that the signals usually get stronger. Working at low frequencies does not necessarily imply a loss of resolution; the heated area will still be limited by the size of the heating beam.

2.4.1 General form for the periodic temperature

In solving for the general three-dimensional response, we again assume that the heat is absorbed entirely at the surface. The penetration depth can be included in a straightforward manner, but since the correction is minor for the opaque samples studied in this thesis, it is omitted for the sake of physical clarity. We further assume that the heating source has cylindrical symmetry, as is most common, and work in two dimensions, r and z. (In Chapter 5 we will be concerned with anisotropic measurements and this restriction will be dropped, but the general approach will be the same.)

Inside the material the temperature obeys the homogeneous diffusion equation. In cylindrical coordinates, the general solution is of the form

$$\theta \sim J_0(\beta r)\, e^{-\sqrt{\beta^2+k_t^2}\, z} \tag{2.20}$$

where J_0 is the Bessel function of order zero. To match the boundary conditions at the sample surface, we construct a superposition of the various radial components, β,

$$\theta(r,z) = \int_0^\infty A(\beta)\, J_0(\beta r)\, e^{-\sqrt{\beta^2+k_t^2}\, z}\, d\beta\ . \tag{2.21}$$

$A(\beta)$ is determined by the boundary condition at the surface. Matching the temperature gradient to the heat input at the surface, J(r), gives

$$-\kappa \left.\frac{\partial\theta}{\partial z}\right|_{z=0} = \kappa \int_0^\infty \sqrt{\beta^2+k_t^2}\, A(\beta)\, J_0(\beta r)\, d\beta = J(r). \tag{2.22}$$

Taking the Hankel transform of both sides by multiplying by $2\pi\, J_0(2\pi qr)$ and integrating over r dr, we obtain

$$2\pi\kappa \int_0^\infty d\beta\ A(\beta)\, \sqrt{\beta^2+k_t^2} \int_0^\infty J_0(\beta r)\, J_0(2\pi qr)\, r dr = H(q) \tag{2.23}$$

where H(q) is defined as the Hankel transform of J(r). The Bessel functions are orthogonal, so the left-hand side simplifies to

$$2\pi\kappa \int_0^\infty d\beta\ A(\beta)\ \sqrt{\beta^2+k_t^2}\ \delta\left(q - \frac{\beta}{2\pi}\right) \tag{2.24}$$

giving,

$$A(2\pi q) = \frac{1}{2\pi\kappa} \frac{2\pi q}{\sqrt{(2\pi q)^2+k_t^2}} H(q)\,. \tag{2.25}$$

Thus the final formula for the periodic temperature variation is given by the following transform:

$$\theta(r,z) = \frac{1}{2\pi\kappa} \int_0^\infty \frac{e^{-\sqrt{\beta^2+k_t^2}\ z}}{\sqrt{\beta^2+k_t^2}}\ H\left(\frac{\beta}{2\pi}\right) J_o(\beta r)\ \beta\, d\beta\,. \tag{2.26}$$

This formula is the basis for nearly all of the thermal analysis in this work. It applies for all cylindrical heat sources and operating frequencies; the sole approximation being that the penetration depth is small. The transformed heating profile, H, contains the geometric effects of the source (both size and shape), while k_t contains the frequency dependence. The positional dependence appears in the exponential decay and as the transform variable.

The origins of equation (2.26) can be understood in another way by evaluating the transform of the first two terms, scaled by $4\pi\kappa$,

$$\frac{1}{4\pi\kappa} \int_0^\infty \frac{e^{-\sqrt{\beta^2+k_t^2}\ z}}{\sqrt{\beta^2+k_t^2}} J_o(\beta r)\, \beta d\beta = \frac{e^{-k_t\sqrt{r^2+z^2}}}{4\pi\kappa\sqrt{r^2+z^2}}\,. \tag{2.27}$$

The right-hand side of (2.27) is recognized as the thermal response of an infinite medium to a point source of flux (the Green function in spherical coordinates is $G(r) = e^{-k_t r}/4\pi r$). Hence (2.26) is equivalent to the convolution,

$$\theta(r,z) = 2 \int_0^\infty G(r-r') \, h(r') \, dr' \, . \tag{2.28}$$

Note that this convolution involves the Green function for an *infinite* medium with a factor of two to account for the boundary conditions. The sample surface was assumed to be a perfect thermal insulator; the only heat flow across the surface is that of the input beam. By symmetry, this is physically identical to an infinite medium with twice the input heat at z=0, hence the simple convolution expression applies. We will not be as fortunate in our examination of the acoustic response because the boundary condition is more complicated and there are subsurface sources.

Now that we have a completely general expression for θ, we can examine which thermal parameters are important in the low- and high-frequency extremes. First, recall that $H(\beta/2\pi)$ is the Hankel transform of the heat source, so its highest spatial-frequency component is approximately $\beta=1/r_h$, where r_h is the radius of the heating spot.

For high frequencies, k_t is much greater than $1/r_h$ and the radicals in (2.26) are dominated by k_t over the finite range of H. The formula for θ becomes

$$\theta(r,z) \cong \frac{e^{-k_t z}}{2\pi\kappa k_t} \int_0^\infty H(\tfrac{\beta}{2\pi}) \, J_0(\beta r) \, \beta d\beta = \frac{e^{-k_t z}}{\kappa k_t} h(r) \tag{2.29}$$

which is identical to (2.9) for a one-dimensional source. Again, the magnitude of the AC surface temperature depends on both thermal constants, κ and C.

At the low-frequency extreme, k_t is much less than $1/r_h$. In the region outside the spot, $r > r_h$, $J_0(\beta r)$ dies off rapidly so that H is roughly constant over the finite range of the integrand. In this case, the integral of (2.26) can be solved analytically to give

$$\theta(r,z) \cong \frac{P_h}{2\pi\kappa} \frac{e^{-k_t\sqrt{r^2+z^2}}}{\sqrt{r^2+z^2}} \qquad (r >> r_h) \tag{2.30}$$

which is, again, the solution for a point source in spherical coordinates. The photothermal behavior outside the region of a small heated spot resembles that of a point source regardless of the shape of the spot, analogous to the electrostatic potential about a small distribution of like charges. Notice that within $\sqrt{2D/\omega}$ of the source, where the exponential damping is minimal, the temperature depends *solely* on the thermal conductivity. At low frequencies the temperature profile approaches that of a DC source and the time dependent terms involving C disappear. Hence, by measuring the temperature at these two frequency extremes, we can determine two independent thermal parameters, κ and C.

Figure 2.1 shows the amplitude and phase of the surface temperature at the center of a Gaussian source of radius r_h (i.e. $H(\beta/2\pi) = P_h \exp(-(.5r_h\beta)^2)$). Equation (2.26) was evaluated numerically using the Fast-Fourier-Transform techniques outlined in the appendix. The plot exhibits the features described above, namely, the leveling off at low frequencies to the DC value of $P_o/ 2\sqrt{\pi}\,\kappa r_h$ (as determined by evaluating (2.26) for r, z, and $k_t = 0$), a $1/\sqrt{f}$ dependence at high frequencies, and a knee where $1/k_t$ equals the spot size.

The spatial dependences of the temperature, under the two frequency extremes, are shown in Figure 2.2 As expected, the low-frequency amplitude is dominated by a 1/r decay while at high frequencies the amplitude follows the heating profile. Note that the extent of the heated area is roughly the same as the optical spot size, even in the low-frequency limit. By switching to low frequencies we sacrifice only 50 % in the resolution. The same cannot be said of the displacement method, as we show in the next section.

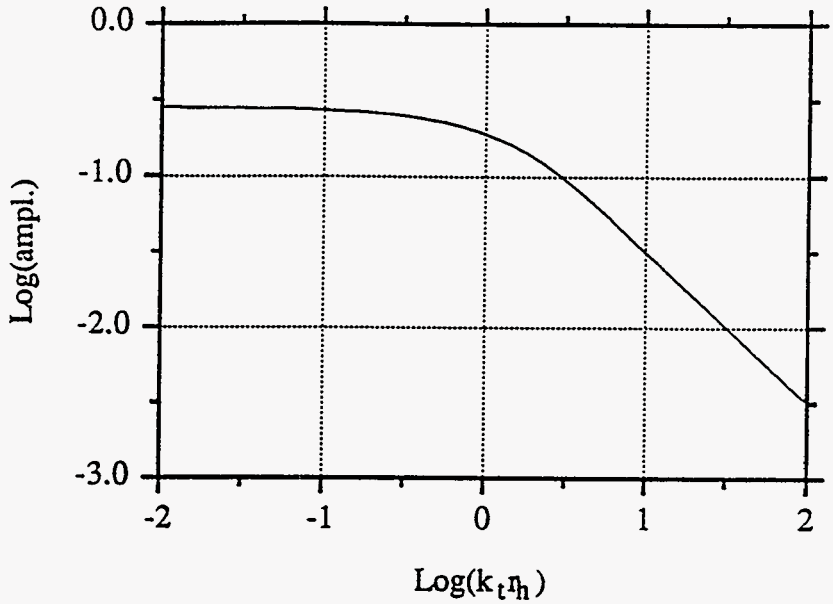

Figure 2.1 Calculated surface temperature as a function of the modulation frequency.

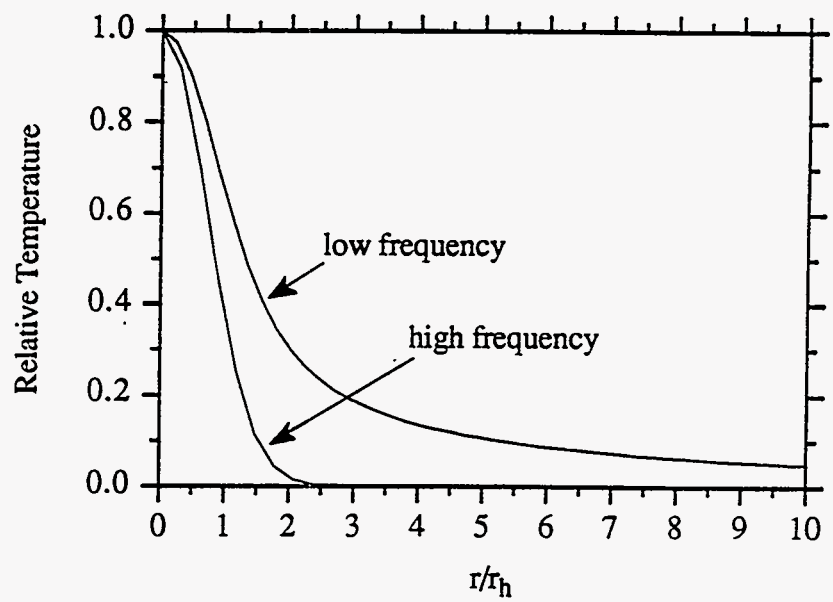

Figure 2.2 Profiles of the temperature in the two frequency extremes.

2.4.2 General solution for the displacement

Now that we have an expression for the temperature profile, it might seem to be a straightforward procedure to calculate the displacement. However, the problem is

complicated greatly by the nature of the boundary conditions. In most cases, the surface is a stress-free boundary and the strain is given by the Duhamel-Neumann relation,

$$T_{ij} = 2\mu S_{ij} + \left(\lambda S_{kk} - (3\lambda+2\mu)\alpha\theta\right)\delta_{ij} . \tag{2.31}$$

While the shear strains simply equal zero at the surface, the longitudinal strains are interrelated and are functions of θ. Since both shear and longitudinal waves are created upon reflection from the surface, the full thermoacoustic equation, (2.2), must be used.

Before attempting to find a rigorous solution, it is worthwhile to examine the relative importance of the terms in (2.2). With a few reasonable assumptions we can reduce the equation to the point where a simple solution exists. After we have calculated the full solution, we will find that the simple formula is remarkably accurate for normal operating conditions. First, at typical operating frequencies, k_t is much greater than k_l. Therefore, we expect the terms involving gradients of $\mathbf{u}$ to exceed the time dependent term. Dropping the latter from (2.2) and expanding the Laplacian to $\nabla\nabla\bullet\mathbf{u} - \nabla\times\nabla\times\mathbf{u}$, we get the following equation for $\mathbf{u}$,

$$(\lambda+2\mu)\nabla\nabla\bullet\mathbf{u} - \mu\nabla\times\nabla\times\mathbf{u} = (3\lambda+2\mu)\alpha\nabla\theta . \tag{2.32}$$

As a further approximation, we ignore the shear terms, leaving

$$\nabla\bullet\mathbf{u} = \alpha'\theta \quad , \quad \alpha' \equiv \alpha\left(\frac{3\lambda+2\mu}{\lambda+2\mu}\right). \tag{2.33}$$

At the surface the axial motion is unconstrained, while radial motion is restricted by the presence of unheated material. Therefore it might seem reasonable to assume that S_{zz} is far greater than S_{rr} and $S_{\phi\phi}$. With this further assumption, the axial surface displacement reduces to

$$\frac{\partial u_z}{\partial z} = \alpha'\theta . \tag{2.34}$$

With these approximations, the surface displacement becomes a simple integration of the thermal expansion through the sample,

$$u_z = \int_0^\infty \alpha' \theta \, dz \ . \tag{2.35}$$

Substituting θ from Section 2.4.1, we get

$$u_z = \frac{\alpha'}{2\pi\kappa} \int_0^\infty \frac{e^{-\sqrt{\beta^2+k_t^2}\, z}}{\beta^2 + k_t^2} \, H(\tfrac{\beta}{2\pi}) \, J_0(\beta r) \, \beta d\beta \ . \tag{2.36}$$

We will show below that (2.36) is nearly exact for all normal operating conditions. Ignoring the shear terms, as we did above, leads to an omission of a small factor in front of the integral. In our experiments we can monitor this displacement in one of two ways: we can measure the total displacement interferometrically, or we can measure the slope of the deformation using a beam deflection technique. These two methods will be compared below after we have justified (2.36) with an exact solution.

To find the full solution, we begin by decomposing the displacement, **u**, into a potential and a solenoidal part

$$\mathbf{u} = \nabla\Phi + \nabla\times\Psi \tag{2.37}$$

with $\nabla\bullet\Psi$ chosen to be zero. The potential, Φ, refers to dilational vibrations, while the vector Ψ represents the shear wave components. Substituting **u** into (2.2) leads to two equations for Φ and Ψ :

$$\nabla^2\Phi + k_l^2\,\Phi = \alpha'\theta \quad , \qquad k_l \equiv \frac{\omega}{\sqrt{(\lambda+2\mu)/\rho}} \tag{2.38}$$

$$\nabla^2\Psi + k_s^2\,\Psi = 0 \quad , \qquad k_s \equiv \frac{\omega}{\sqrt{\mu/\rho}} \tag{2.39}$$

where k_l and k_s are the longitudinal and shear propagation constants. The general solution to these equations parallels that of Section 2.4.1 for the temperature. Therefore, we will only outline the steps here. Since the equation for Ψ is just the vector wave equation for no ϕ-variations, Ψ can be written directly:

$$\Psi = \int_0^\infty B(\beta)\, J_1(\beta r)\, d\beta\, \hat{\phi} \; . \tag{2.40}$$

We choose Ψ_r and Ψ_z to be zero so that the displacement, $\nabla\times\Psi$, has no ϕ-component.

The formula for Φ is a little more complicated since we must include the particular solution that matches $\alpha'\theta(r,z)$. After some algebra we find that the general solution is

$$\Phi = \int_0^\infty \left\{ A(\beta)\, e^{-\sqrt{\beta^2-k_l^2}\, z} + C(\beta)\, e^{-\sqrt{\beta^2+k_t^2}\, z} \right\} J_o(\beta r)\, d\beta \; , \tag{2.41}$$

where $C(\beta)$ is determined by the β-component of the surface temperature given in equation (2.26),

$$C(\beta) \equiv \alpha' \frac{1}{k_l^2+k_t^2}\,\theta_o(\beta) = \alpha' \frac{1}{2\pi\kappa}\, \frac{\beta\, H(\beta/2\pi)}{\sqrt{\beta^2+k_t^2}\,(k_l^2+k_t^2)} \; . \tag{2.42}$$

The general expression for expression **u** is generated from $\nabla\Phi + \nabla\times\Psi$:

$$\mathbf{u} = \int_0^\infty \left\{ -\beta A(\beta) e^{-\sqrt{\beta^2-k_l^2}\, z} + \sqrt{\beta^2-k_s^2} B(\beta) e^{-\sqrt{\beta^2-k_s^2}\, z} - \beta C(\beta) e^{-\sqrt{\beta^2+k_t^2}\, z} \right\}$$

$$\times J_1(\beta r)\, d\beta\ \hat{\mathbf{r}}$$

$$+ \int_0^\infty \left\{ -\sqrt{\beta^2-k_l^2} A(\beta) e^{-\sqrt{\beta^2-k_l^2}\, z} + \beta B(\beta) e^{-\sqrt{\beta^2-k_s^2}\, z} - \sqrt{\beta^2+k_t^2} C(\beta) e^{-\sqrt{\beta^2+k_t^2}\, z} \right\}$$

$$\times J_0(\beta r)\, d\beta\ \hat{\mathbf{z}} \tag{2.43}$$

Now that we have the general form, it remains to calculate the coefficients, A and B, for our particular boundary conditions. The shear and stress at the surface obey

$$T_{rz} = 2\mu S_{rz} = \mu \left(\frac{\partial u_z}{\partial r} + \frac{\partial u_r}{\partial z} \right) = 0\ , \tag{2.44}$$

$$T_{\phi z} = 2\mu S_{\phi z} = 0\ , \tag{2.45}$$

$$T_{\phi r} = 2\mu S_{\phi r} = 0\ . \tag{2.46}$$

The second two conditions are satisfied automatically by our choice for the ϕ dependence of Φ and Ψ. The first equation places the following restriction on A and B:

$$2\beta\sqrt{\beta^2-k_l^2}\, A + (k_s^2 - 2\beta^2) B = -2\beta\sqrt{\beta^2+k_t^2}\, C\ . \tag{2.47}$$

A second equation for A and B comes from the longitudinal boundary condition. The normal stress at the surface is given by the Duhamel-Neumann relation,

$$T_{zz} = 2\mu S_{zz} + \lambda(S_{rr} + S_{\phi\phi} + S_{zz}) - (3\lambda+2\mu)\, \alpha\, \theta_o = 0\ . \tag{2.48}$$

The strains are related to the displacements by [6]

$$S_{rr} = \frac{\partial u_r}{\partial r}, \quad S_{\phi\phi} = \frac{1}{r}\left(\frac{\partial u_\phi}{\partial \phi} + u_r\right), \quad S_{zz} = \frac{\partial u_z}{\partial z}. \tag{2.49}$$

Thus, the boundary condition on **u** is

$$2\mu\frac{\partial u_z}{\partial z} + \lambda\left(\frac{\partial u_r}{\partial r} + \frac{u_r}{r} + \frac{\partial u_z}{\partial z}\right) = (3\lambda+2\mu)\,\alpha\,\theta_o\,. \tag{2.50}$$

Carrying out the derivatives, we get

$$(\beta^2 v^2 - k_l^2)\,A - \beta\sqrt{\beta^2 - k_s^2}\,B + (\beta^2 v^2 + k_t^2)\,C = \alpha'\theta_o \tag{2.51}$$

where v is defined as $2\mu/(\lambda+2\mu) = 2k_s^2/k_l^2$.

We now have two equations for the two unknowns (recall $C(\beta)$ is given by (2.42)) These two equations, along with the general expression for **u**, completely determine the displacement. The solutions for A and B are quite messy in general, but if we restrict our attention to the displacement at z=0, we need not calculate A. Instead, we can use the first boundary condition, (2.47), directly in the expression for u_z to show that

$$u_z(0) = \int_0^\infty \frac{k_s^2}{2\beta} B(\beta)\, J_o(\beta r)\, d\beta \tag{2.52}$$

The derivation of $B(\beta)$ involves too much algebra to repeat here. The result is

$$u_z(0) = \frac{\alpha' k_s^2}{2\pi\kappa} \int_0^\infty \frac{(\beta^2 v^2 - k_l^2)\left[\sqrt{\beta^2 - k_l^2} - \sqrt{\beta^2 + k_t^2}\right]}{(\beta^2 v^2 - k_l^2)(k_s^2 - 2\beta^2) + 2\beta^2 v^2 \sqrt{\beta^2 - k_l^2}\sqrt{\beta^2 - k_s^2}}$$

$$\times \quad \frac{H\left(\frac{\beta}{2\pi}\right)}{\sqrt{\beta^2 + k_t^2}\,(k_t^2 + k_l^2)} J_o(\beta r)\, \beta d\beta \qquad (2.53)$$

This is the exact formula for the surface displacement, the only approximation being the decoupling of the two thermoacoustic equations as mentioned above. The pole in the denominator of the first term, near $\beta = k_s$, represents the value of β at which Rayleigh waves are excited. (In fact, if the denominator is expanded it will be recognized as the Rayleigh characteristic equation for the radial propagation constant at a vacuum interface [7].) In practice, we operate at frequencies where these acoustic effects are negligible.

While it is satisfying to have a completely general form for our numerical work, (2.53) is too complex for physical insight. To better understand the surface displacement, we can examine its low and high frequency limits, much as we did with the formula for θ. For high frequencies (or equivalently, for large-area heat sources) $H(\beta/2\pi)$ cuts off at very small β. Letting β approach zero and rearranging terms leads to

$$u_z(0) = \frac{\alpha'}{k_l^2 + k_t^2} \frac{jk_l - k_t}{\kappa k_t} \frac{1}{2\pi} \int_0^\infty H\left(\frac{\beta}{2\pi}\right) J_o(\beta r)\, \beta\, d\beta \qquad (2.54)$$

The leading terms are precisely those of the one-dimensional formula in Section 2.3. The integral contains the effect of the shape of the heat source. As stated before, k_t always exceeds k_l in practice, so $u_z(0)$ varies as $\alpha'/\omega C$ at high frequencies, and is independent of κ.

For optical heating, where the spot size is on the order of a micron, we can also simplify (2.53). The function H extends out to a range of $\beta \cong 1\ \mu m^{-1}$, far greater than

the magnitude of the acoustic propagation constants under normal operating frequencies. Therefore, over the major part of the range of integration, $\beta >> k_s$ and k_l. Using this approximation gives us

$$u_z \cong \frac{1}{1-.5v^2} \frac{\alpha'}{2\pi\kappa} \int_0^\infty \frac{\beta - \sqrt{\beta^2+k_t^2}}{\sqrt{\beta^2+k_t^2}} \frac{H(\frac{\beta}{2\pi})}{k_l^2+k_t^2} J_o(\beta r)\, \beta d\beta \tag{2.55}$$

This formula is appropriate for all normal operating conditions. It approaches the approximate expansion formula, (2.26), when the frequency is low enough such that k_t is also small (spot size smaller than the thermal diffusion length). This can be demonstrated by multiplying the numerator and denominator by $\sqrt{\beta^2+k_t^2}$ and using a binomial approximation for the radical,

$$u_z \cong \frac{1}{2-v^2} \frac{\alpha'}{2\pi\kappa} \int_0^\infty \frac{1}{\beta^2+k_t^2} H(\tfrac{\beta}{2\pi})\, J_o(\beta r)\, \beta d\beta\,. \tag{2.56}$$

The only difference between (2.56) and the approximate formula is the factor containing v in front. Substituting the Lamé constants back into this factor leads to

$$u_{z_{full}} = \frac{\lambda+2\mu}{2\lambda+2\mu} u_{z_{approx}} \cong \frac{3}{4} u_{z_{approx}} \tag{2.57}$$

Thus, the omission of the shear terms in the approximate formula leads to an overestimation of the surface displacement by about 30%.

At low frequencies, $\beta >> k_t$, (2.56) shows that, as expected, the surface displacement depends solely on the thermal conductivity. Unlike the surface temperature, however, the magnitude of the displacement does not level off to a DC value. The displacement continues to grow until frequencies are reached at which the sample can no longer be treated as semi-infinite in extent. Thus, the displacement method can give rise to

very large signals at low frequencies. However, there will still be a practical lower limit to the frequency because, unlike the temperature, the size of the affected area also continues to increase with frequency. The lower limit will be set by the minimum acceptable resolution.

Figure 2.3 shows the amplitude of the surface displacement as a function of frequency. Also shown for comparison are the surface temperature, previously calculated, and the radial slope, $\partial u/\partial r$. This latter quantity is simply (2.56) with J_0 replaced by βJ_1, and represents the type of signal we can expect in a photothermal deflection experiment. Note that all three quantities have a knee at $r_h = 1/k_t$, above which the displacement methods decay more rapidly. Below the knee, only the absolute value of the displacement continues to improve, the other methods approach a DC upper limit.

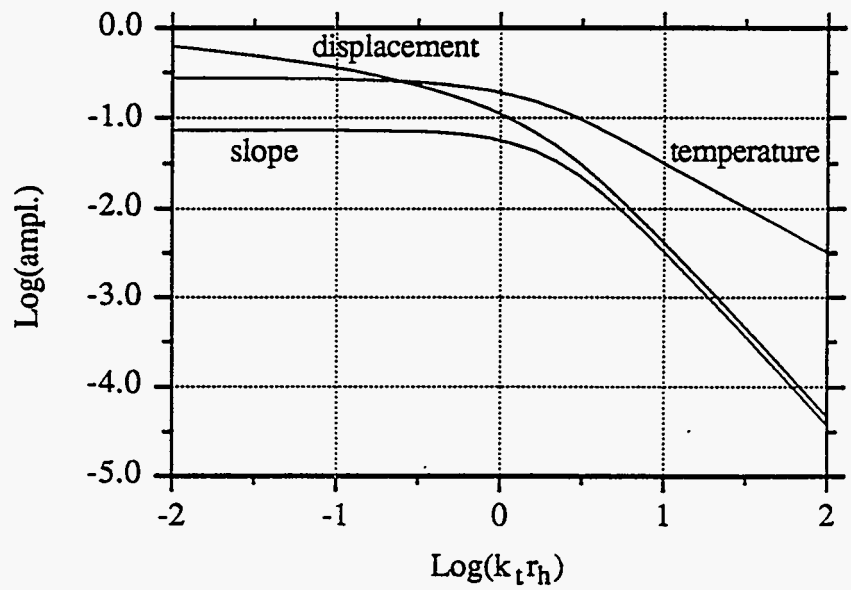

Figure 2.3 Amplitudes of the surface displacement, surface temperature, and slope as a function of the modulation frequency.

To complete the comparison, however, we need to look at the resolution as well. The radii at the half-maximum of these three methods are compared in Figure 2.4. (This definition of the resolution is an arbitrary one, but while the shape of these curves depends

somewhat upon our choice, the overall conclusions remain the same.) We see that the spatial extent of the AC temperature, and to a lesser degree of the slope method, is nearly independent of the operating frequency. The resolution of these methods is determined by the size of the heating spot. The resolution of the displacement method, however, degrades rapidly with decreasing frequency. Hence the improvement in signal strength must be balanced against this decrease in resolution. In the next chapter we will examine the means by which we convert temperature and displacement fluctuations into optical signals. We will then be able to make direct comparisons between the relative strengths of these three methods.

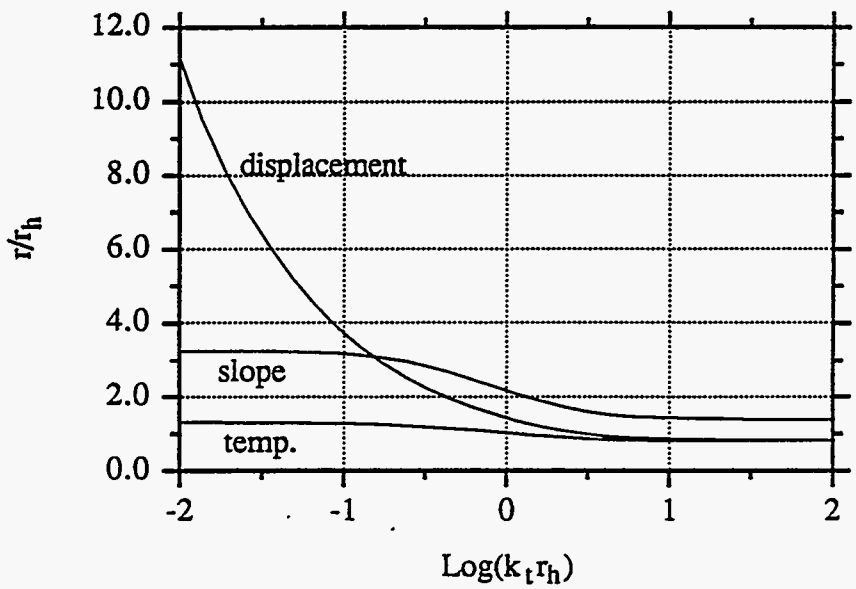

Figure 2.4 Resolution of the three methods as a function of frequency. (Resolution being defined as the radius at which the amplitude of the effect drops by a half.)

2.5 Thermal Effects of the Environment

Thus far, we have assumed that our optical signals are caused entirely by fluctuations in the samples. In practice, however, these experiments are often conducted in

an open environment, leading to the possibility that thermal fluctuations in the air itself might contribute to the signal. While these effects are the basis of mirage and photoacoustic-cell techniques, in our case they represent undesirable spurious signals that can complicate interpretation of our data. This section will give a crude estimate of the relative strengths of these unwanted effects.

The temperature fluctuations in the air are caused by its contact with the heated samples; the amount of heat coming directly from the optical pump is negligible. Therefore we have, once again, a semi-infinite medium heated at its surface. Since the thermal conductivity of air is so poor (0.025 W/m-K [8]), it presents a negligible thermal load on the sample. Thus, we can use the formulas above to calculate the sample's surface temperature, and then invoke continuity of temperature to give us the boundary condition for the temperature profile in the air. As we saw in Section 2.3, the decoupled-equation approximation does not apply in air, so, for an accurate description, we should use the full set of coupled thermoacoustic differential equations. However, since we are only interested in a ballpark estimate of the spurious effect, we will use the approximation anyway.

The temperature profile in the air is of the form

$$\theta_a(r,z) = \int_0^\infty A(\beta)\, J_0(\beta r)\, e^{-\sqrt{\beta^2+k_{ta}^2}\, z}\, d\beta \tag{2.58}$$

with a surface value of $\theta_a(r,0) = \theta_s(r,0)$. The subscripts a and s refer to the air and the sample. Direct comparison of (2.58) with the formula for θ_s, (2.26), gives us $A(\beta)$. Thus

$$\theta_a(r,z) = \frac{1}{2\pi\kappa_s} \int_0^\infty \frac{e^{-\sqrt{\beta^2+k_{ta}^2}\, z}}{\sqrt{\beta^2+k_{ts}^2}}\, H\left(\frac{\beta}{2\pi}\right) J_0(\beta r)\, \beta\, d\beta\,. \tag{2.59}$$

The effects of θ_a are two-fold, both arising from the temperature dependence of the refractive index, n_a. First, gradients in θ_a will cause the air to act as a weak lens. Fortunately, the lensing will not affect our signal as long as we ensure that the entire beam is collected. Thus, the only technique that might is be affected by these thermal gradients is the slope method (another reason why we use the other two techniques almost exclusively).

A second effect is that the optical path length changes when the air is heated. Thus, the interferometric displacement method will be subject to a spurious phase delay. The contribution of the air is

$$i_{sig} \sim \frac{dn_a}{dT} \int_0^\infty \theta_a(r,z)\, dz$$

$$= \frac{dn_a}{dT} \frac{1}{2\pi\kappa_s} \int_0^\infty \frac{H(\frac{\beta}{2\pi})}{\sqrt{\beta^2+k_{ts}^2}\sqrt{\beta^2+k_{ta}^2}} J_o(\beta r)\, \beta\, d\beta \qquad (2.60)$$

The thermal diffusivity of air at room temperature and pressure is 20 mm^2/s, roughly equivalent to that of the solids we will be studying. Therefore the temperature profiles in the air and in the sample are approximately the same, and the comparison of the two contributions reduces to a comparison of dn_a/dT with the thermal expansion coefficient, α_s. Since dn_a/dT is about $9 \times 10^{-7}/°C$ [8], the ambient effect is generally an order of magnitude weaker. In summary, the contributions to the optical signal due to thermal effects of the environment are minor.

Chapter 2 References

1. W. Nowacki, *Thermoelasticity*, Oxford: Pergamon Press, 1962 (Chapter 1).
2. L.D. Favro, S.M. Shepard, P.K. Kuo, and R.L. Thomas, "Mechanisms for the generation and scattering of sound and thermal waves in thermoacoustic microscopes," in *Photoacoustic and Photothermal Phenomena* , Eds. P. Hess and J. Pelzl, Springer-Verlag: Springer Series in Optical Sciences **58**, 1988.
3. R. Stearns, *Photoacoustic Techniques for the Quantitative Characterization of Materials*, Ph.D. Dissertation, Stanford University, 1985.
4. J. Opsal and A. Rosencwaig, "Thermal-wave depth profiling: Theory," *J. Appl. Phys.* **53** (6), 4240 (1982).
5. B.A. Auld, *Acoustic Fields and Waves in Solids*, Vol. 1. New York: John Wiley & Sons, 1973.
6. W. Nowacki, *Thermoelasticity*, Oxford: Pergamon Press, 1962 (Chapter 1).
7. Ivan Tolstoy, *Wave Propagation*, New York: McGraw-Hill, Inc., 1973 (p. 207).
8. *CRC Handbook of Chemistry and Physics*, West Palm Beach, FL: CRC Press, Inc., 1980.

Chapter 3

Experimental Configuration and Sensitivities of Various Detection Schemes

3.1 Introduction

In recent years, a variety of experiments have been designed to monitor one or more of the various photothermal responses. The major limitation in all of these experiments is that the signals are weak. Long signal-averaging times must be used, making photothermal imaging a slow process. This limitation becomes more severe as one pushes for finer resolutions where the optical power per area of the heating and probe spots can become quite large. Eventually, the damage threshold of the sample limits the optical powers and, therefore, the signal strength. In our studies of high-T_c superconductors the power restriction is even tighter since the total temperature increase at the surface (both AC *and* DC) must be kept under a degree. A major goal of this research was to extend the sensitivity of these types of measurements at high resolutions.

To improve the sensitivity we concentrated on four major limitations of the signal-to-noise. First, we minimized the optical noise by using laser diode sources, which can have very low intensity noise, and by using balanced interferometers to eliminate optical phase noise. In high-frequency experiments, additional electronic noise was avoided by modulating the probe laser intensity, rather than using electronic mixers, to lower the signal frequency to the range of the lock-in. Furthermore, we minimized unwanted sample vibrations in the displacement measurements by using the sample surface as the reference for the interferometry. Finally, we made the system flexible so that more than one type of measurement could be performed, allowing a choice of the strongest effect for each

particular sample. In this chapter we present the results of this effort, and compare the signal-to-noise ratios of the various approaches.

We begin with a description of the experimental arrangement, with emphasis on the techniques we use to convert the fluctuations in the sample to fluctuations in our optical probe. This is followed by an analysis of the shot-noise limited sensitivities of each method. In Section 3.4, we compare these methods given certain constraints on the damage threshold and the resolution. We will find that the most sensitive method is a function not only of the material constants, but of our resolution as well, with the displacement methods becoming comparably better as the resolution requirement is relaxed (greater than a few microns).

3.2 Experimental Layout

The photothermal microscope is shown in Figure 3.1, a schematic of which is in Fig 3.2. The optical train headed by the argon-ion laser is used for heating and viewing the sample. An acousto-optic cell modulates the output of the laser up to frequencies as high as a few megahertz. The heating beam then joins the probe beam (output of the diode laser) at the dichroic mirror, which is highly reflective at visible wavelengths and transparent at wavelengths above 700 nm. Finally, both beams are focussed on the sample using one of the objective lenses described in the next section. This portion of the microscope also contains a tungsten-filament microscope lamp for illuminating the sample area under test. A magnified image of the test site, including both laser spots, is projected onto a viewing screen as shown. The noise performances of these components are not critical since they are used strictly for heating and observation. When measuring electrically-heated samples, the argon-ion laser is omitted.

The components of the second optical train, headed by the semiconductor diode laser, determine the noise level of the measurement. We use a diode laser for our probe

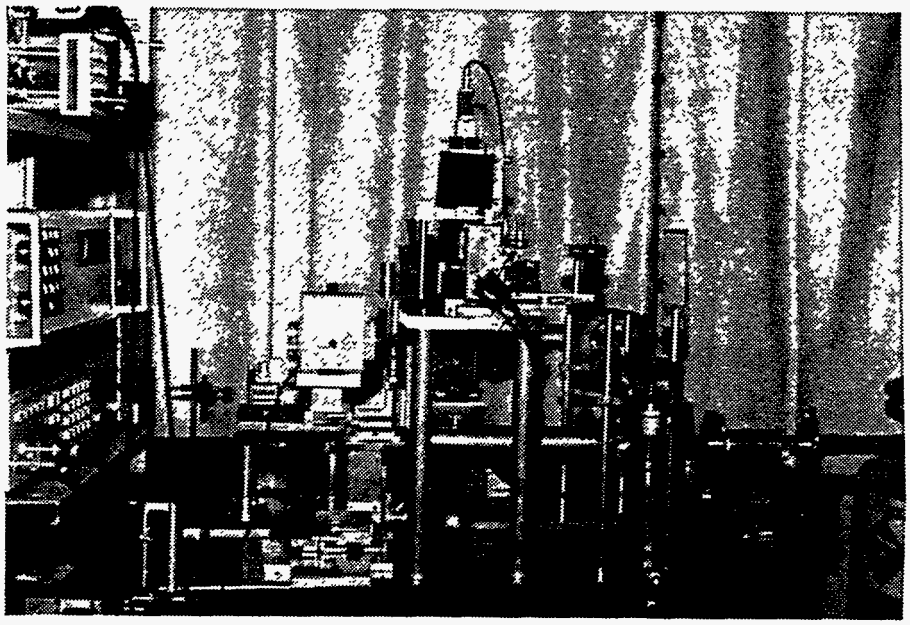

Figure 3.1 Photograph of the photothermal microscope.

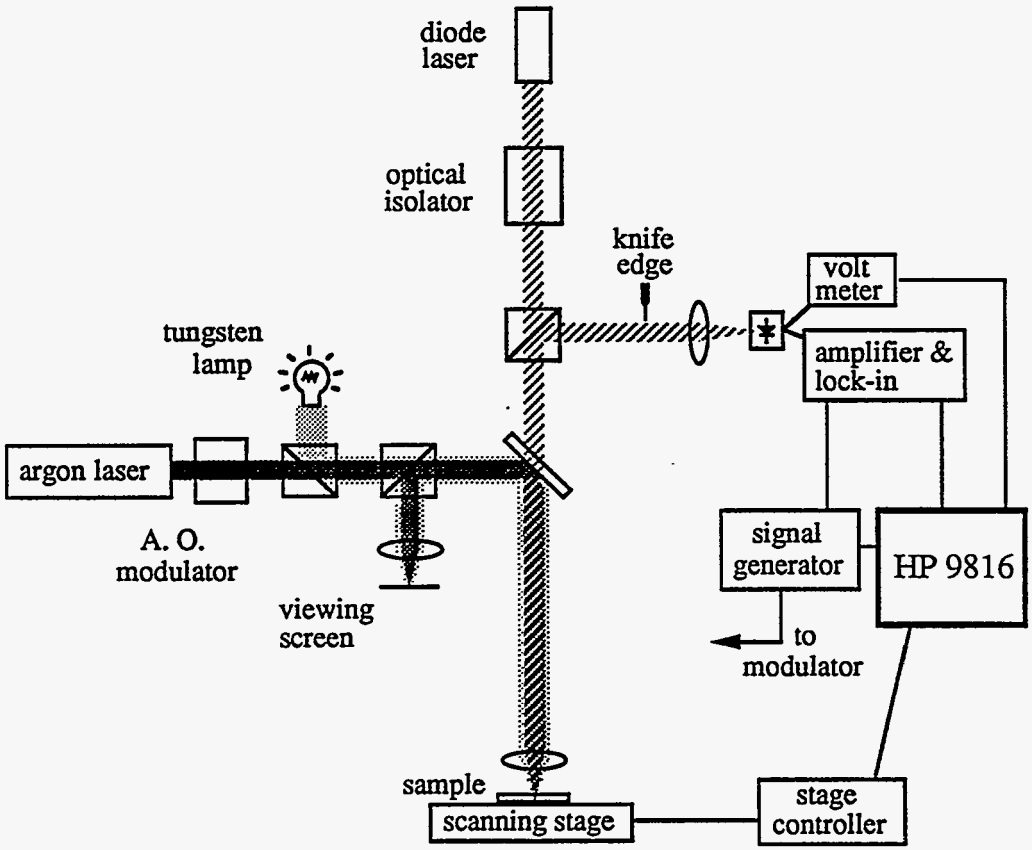

Figure 3.2 Schematic of the microscope.

because of the stability of its output. When driven near its peak power and properly isolated from back-reflected light, it is possible to generate nearly shot-noise limited beams. These lasers have a number of other practical advantages as well, most important of which, perhaps, is the ability to modulate their output power by simply modulating the drive current. Thus high-frequency experiments can be conducted using simple optical mixing, rather than electronic mixing, to downshift the signal into the frequency range of the lock-in amplifier. These features, however, come at a price. The spectral lines of these lasers are much wider than those in typical bench-top lasers; diode lasers have short coherence lengths and poor phase-noise characteristics. This does not affect the reflectivity and the slope experiments, in which only the optical intensity is measured, but can destroy the sensitivity of the interferometric measurements if the path lengths of the interfering beams are not equal. We will return to this point below.

After being reflected from the sample, the probe beam is focussed to a high-speed photodetector. The induced photocurrent drives a load resistor whose value depends on the bandwidth needed for the experiment, the tradeoff being one of signal strength versus speed. Since our particular detector and input amplifier have a combined capacitance of about 8 pF, we chose a load resistance of 50 kΩ to set the rolloff frequency slightly above the range of the lock-in amplifier. The AC component is amplified and sent to an EG&G model 5206 lock-in amplifier. The DC component (or reflectivity) is measured with a separate voltmeter and used to normalize the signals where appropriate. The modulation, signal detection, and DC voltage measurement are all controlled by a Hewlett-Packard Model 9816 computer. The computer also controls a Newport 855 scanning stage upon which the sample is mounted. Thermal images are created by making a point-by-point raster scan over the surface of the sample. The resulting array of signal intensity (or phase) vs. position is then displayed as a three-dimensional line plot on the HP-9816, or as a grey-scale image on a Gould FD5000 video monitor.

3.3 Objective Lenses

The difference between the three types of experiments lies in the focussing element used at the sample. In the reflectivity and the deflection experiments, the probe beam is focussed onto the sample with a standard microscope objective. For the reflectivity measurement, no further components are needed; the temperature-induced intensity modulation is detected directly. To monitor the slope of the heated material, however, the lateral displacement of the reflected beam must be converted to an intensity modulation by placing a knife edge in the path of the beam before the detector lens (see Fig 3.3).

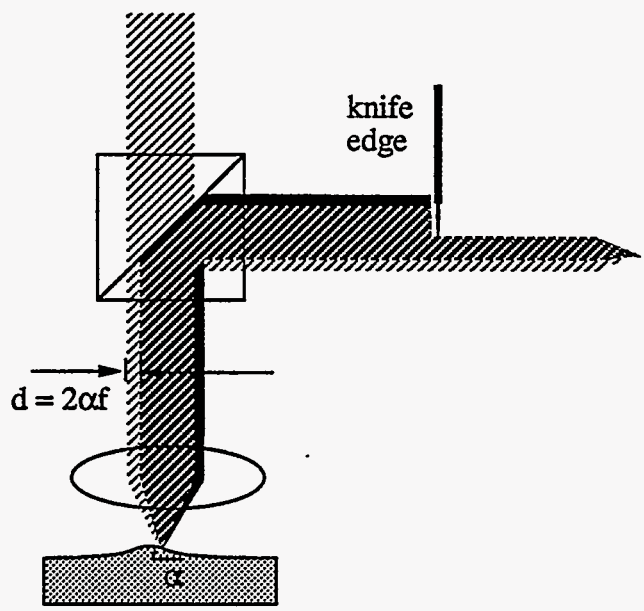

Figure 3.3 The deflection method for the measurement of the surface displacement.

In general, both effects may be present simultaneously, making it necessary to discriminate against one or the other. In the case of the dR/dT measurement, deflection effects are avoided by ensuring that the probe beam sees no apertures between the sample and the detector. This means that both the sample objective and the detector lens must be

underfilled. In the case of deflection measurements, reflectivity fluctuations can be minimized by using a split detector, in place of the knife edge, and detecting the difference between the two halves and dividing by the sum.

In the interferometric experiments, the standard microscope objective is replaced by a beam splitter and a focussing lens. In this work we used two types of splitters, shown in Figures 3.4a and 3.4b. The first approach, which we developed to circumvent vibration problems, use a Wollaston prism as the beam splitter. Shown in Figure 3.4a, the Wollaston prism consists of two birefringent quartz wedges whose optical axes are oriented perpendicularly. Light polarized along the axis of the first wedge experiences an increase in refractive index upon entering the second wedge, while light polarized normal to that sees a decrease. Therefore, a beam polarized at 45° to the prism will split into two equal-intensity beams with an angular separation of $2\Delta n\,\delta$, where δ is the wedge angle, and Δn is the difference in the refractive indices (for quartz $\Delta n \cong 0.01$). These two beams are then focussed to two separate spots on the sample surface.

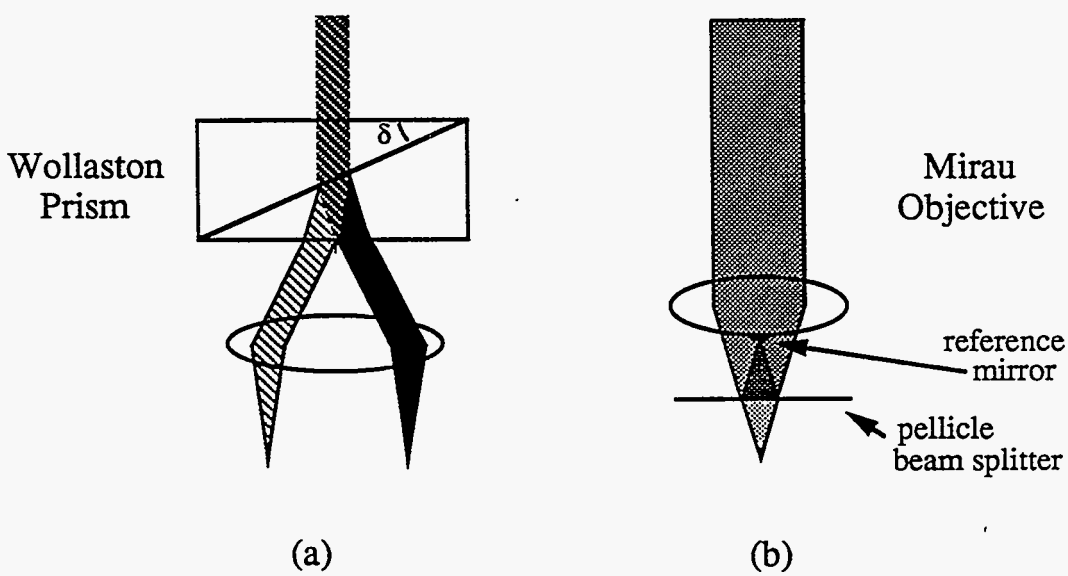

Figure 3.4 The Wollaston and Mirau interferometers used for the measurement of the surface displacement.

When the Wollaston prism is located in the back focal plane of the focussing lens, the two beams converge normally to the sample surface and retrace their paths upon reflection. They recollimate after passing back through the lens, recombine in the prism, and finally, pass through an analyzer to interfere on the photodetector. The great advantage of this arrangement is that both beams pass through the same optical components, as well as reflect off of the sample, making the setup resistant to unwanted vibrations and drift. Displacement experiments based on a Michelson arrangement suffer from component and sample vibrations, and a piezoelectric mirror mount and stabilization circuitry have to be used to reduce the vibration noise [1]. But even despite these modifications to the Michelson interferometer, photoacoustically generated sound can still cause the sample to resonate, obscuring the local thermal response. Our ability to discriminate against these acoustic effects, while retaining full sensitivity to the local thermal expansion, is a fortunate result of the widely differing propagation velocities of these two phenomena. Under normal operating conditions, the reference need only be 10 to 100 microns away from the thermal source for complete isolation. The millimeter-range acoustic vibrations will then affect both spots in unison. Reflecting the reference off of the sample also stabilizes the set-point of the interferometer over the course of a scan on flat materials; sample tilt does not affect our measurement.

Another advantage of the Wollaston prism is that the two optical path lengths are equal when the beams pass through the center of the prism, where they both travel through an equal amount of fast and slow material. Phase-noise problems are thereby avoided, since the two interfering beams are generated by the laser at the same time. The importance of removing the phase noise is demonstrated quite clearly in Figure 3.5. The upper curve is a plot of the measured noise power in a 250 Hz bandwidth (centered at 150 kHz) as a function of path length difference. The path lengths were controlled by translating the Wollaston prism. The data were measured at the points where the static phase difference was $(n+1/2)\pi$ (these would be the normal operating points since they are where the

maximum displacement sensitivity occurs) and normalized by the theoretical shot-noise power. Note that these measurements include all noise sources such as optical intensity and phase noise, sample vibration noise, and Johnson noise of the load resistor.

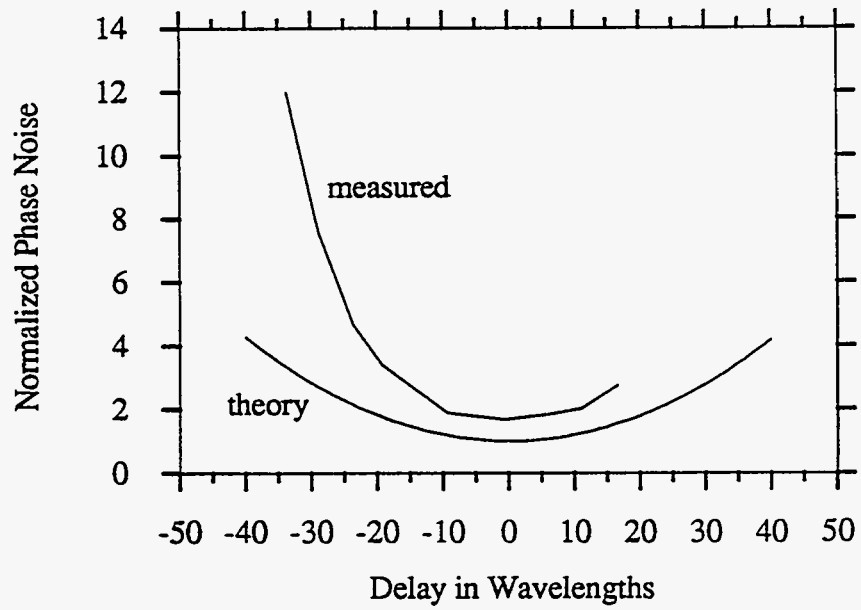

Figure 3.5 Theoretical and measured phase noise in a 250 Hz bandwidth as a function of the static path-length difference.

To check these results we also plotted the theoretical prediction for the phase-noise power of a single Gaussian-mode laser of spectral width D. The intensity noise per Hertz at the detector, due solely to FM quantum noise, is given in Ref. 2 as

$$\frac{N}{P_p} = \frac{D}{2(4\pi f^2 + D^2)} \left\{ 1 - e^{-D\tau}\left(\cos 2\pi f\tau + \frac{D}{2\pi f}\sin 2\pi f\tau\right) \right.$$

$$\left. - \left[e^{-2D\tau} - e^{-D\tau}\left(\cos 2\pi f\tau - \frac{D}{2\pi f}\sin 2\pi f\tau\right)\right] \times \cos(2\omega_0\tau) \right\} \quad (3.1)$$

where P_p is the DC optical power of the probe, ω_o is the optical frequency, f is the detection frequency, and τ is the time delay between the two arms. The laser we used has a coherence length of about 3 mm, for which $D \cong 100$ GHz. We can reduce (3.1) by noting that the spectral width is far greater than the detection frequency, and the time delay is very small. Therefore, if we use small-argument approximations for the sinusoids and exponentials we get for $\omega_o\tau = (n+1/2)\pi$,

$$N_{optical} = \frac{1}{2}\eta P_p D\tau^2 B . \tag{3.2}$$

Here, B is the detection bandwidth and η is the photodetector response (mA/mW). The corresponding photodetector output is

$$P_{detector} = \left[\eta(P_p + N_{optical})\right]^2 R_L \tag{3.3}$$

so that

$$N_{detector} = (\eta P_p)^2 D\tau^2 R_L B , \tag{3.4}$$

where R_L is the load resistance. The shot noise of the detector is given by $2q\eta P_p R_L B$ so that the theoretical noise ratio (for the case where only phase and shot noise are present) has the quadratic form:

$$\frac{N_{total}}{N_{shot}} = 1 + \frac{\eta P_p D}{2q}\tau^2. \tag{3.5}$$

This is the lower curve of Figure 3.5. Clearly, in an unbalanced configuration the phase fluctuations are the dominant source of noise. It is also evident that when the paths are balanced, the interferometer operates near the theoretical limit. The comparably poor measured noise figures at large path differences is likely due to our treatment of the laser as having a single Gaussian mode when, in fact, it has low-level output over a wide range of

frequencies. When a calcite wedge, for which the path length difference was roughly 0.3 mm, was used in place of the Wollaston prism the noise increased by 40 dB.

The other type of interferometer we used, the Mirau objective, is also immune to phase noise effects. Shown in Figure 3.4b, this type of interferometer has a thin-film beamsplitter located halfway between a large-aperture objective and the sample. The reference mirror is a small silver dot printed on the center of the lens. (The size of the mirror need only be about that of the field of view at the focus, or about 100 μm, so that only a small portion of the lens is obscured.) The location of the beam splitter guarantees that the path lengths are equal when the objective is focussed on the sample surface. By combining the beam splitter and reference mirror in one small, rigid package, component vibration is minimized. However, since the reference does not reflect off of the sample photoacoustically generated vibrations can still be a problem.

The output of the Mirau interferometer as a function of the defocussing, dz, is shown in Figure 3.6. This pattern is a combination of two effects which can be easily understood if we ignore diffraction and treat the foci as point sources. When the lens is pulled away from focus by an amount dz, the reflected light appears to emanate from a point 2 dz away. This shift of 2 dz between the two interfering beams gives rise to the rapid cycles every $\lambda/2$. The envelope comes from the mismatch of the wavefront curvatures; the outer rays suffer a smaller total path difference than do the inner rays. If the reflected light is viewed on a screen, one sees circular fringes at the radii where the path-length difference changes by successive π. As dz is increased, more fringes are introduced, causing the total light intensity to fluctuate. Eventually at large dz, there are so many fringes that the interference is washed out. A plot in Figure 3.7, based on this simple point-source model, gives excellent agreement with the measured response. This curve comes from an integration of the interfering wavefronts over the aperture of the lens:

$$I \sim 2\pi \int_{0}^{r_{lens}} \left| e^{-j2k\sqrt{f^2+z^2}} + e^{-j2k\sqrt{(f+dz)^2+z^2}} \right|^2 r\,dr\,. \tag{3.6}$$

Our particular objective has a focal length, f, of 1 cm and an NA of 0.5. From both the measured response and the theoretical curve, it is apparent that the Mirau objective should be operated $\lambda/4$ from the focus for maximum sensitivity. (A more complete analysis of the Mirau objective is given in [3]. The main difference is that the high-spatial-frequency content is exaggerated in the present analysis. The differences, however, are imperceptible for NA's below 0.7)

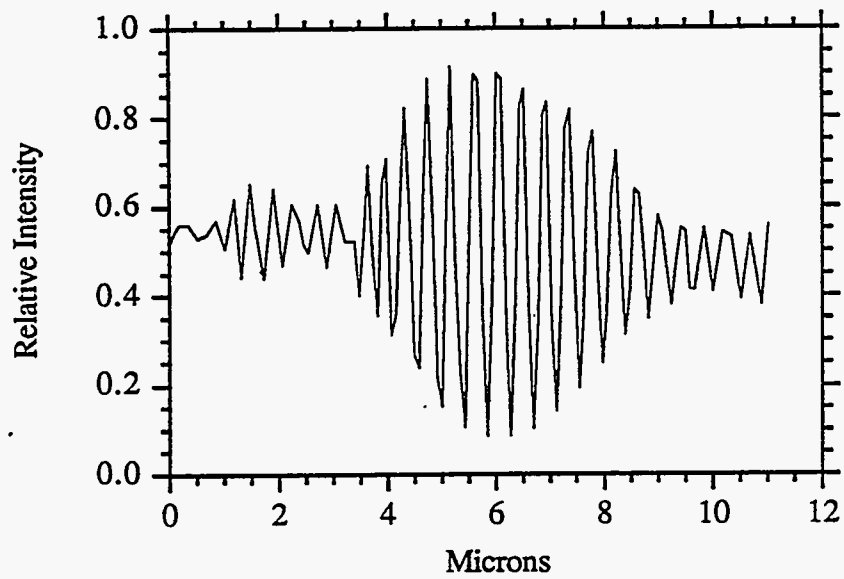

Figure 3.6 Optical intensity at the photodetector measured as a function of the axial position of the Mirau interferometer.

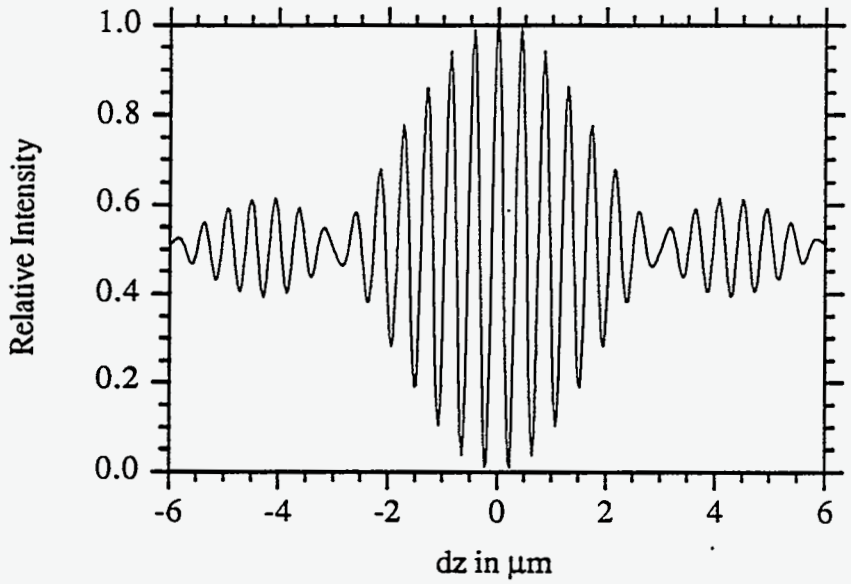

Figure 3.7 Theoretical calculation of the Mirau depth response.

The choice of which type of interferometer to use depends upon the type of sample and the desired resolution. Whenever possible, the differential measurement of the Wollaston prism is preferable since it is insensitive to sample vibrations, and the set point does not drift over the course of a scan. However, the requirement that the prism be in the back focal plane of the lens limits the choice of objectives; back focal planes of high-NA lenses are inaccessible. Although transfer lenses could be introduced to gain access to this plane, it is usually easier to switch to the Mirau objective and to put the effort into damping the sample and aligning the surface precisely.

3.4 Theoretical Sensitivity of the Various Methods

All of the measurement techniques discussed in this thesis involve the conversion of the sample fluctuations to intensity fluctuations of an optical probe. As such, they all suffer

the same types of noise, including amplitude and phase noise of the probe beam, shot noise due to the quantized nature of light, and Johnson, or thermal, noise from the load resistor and amplifiers. The first two types are minimized by using quiet sources and balancing the interferometer paths as discussed above. The final two types, shot noise and Johnson noise, are always present, limiting the ultimate sensitivity of any measurement. In this section we will combine photothermal theory of Chapter 2 with our particular experimental configurations in order to compare the sensitivities of the three methods.

In an ideal set-up, the minimum noise power is

$$N_{shot} + N_{thermal} = 2q\eta P_p R_L B + 4k_B TBF \,. \tag{3.7}$$

We must compare this noise with the signal powers of the various methods. In each of the three techniques (reflectivity, interferometry, slope) the modulation of the probe beam differs. The most straightforward effect is the temperature-induced reflectivity fluctuation, which gives rise to the signal

$$i_{dR/dT} = \eta P_p \frac{dR}{dT}\, \theta_o \cos(\omega_h t) \,, \tag{3.8}$$

where θ_o is the amplitude of the periodic surface temperature at frequency ω_h, and dR/dT is the change in refractive index with temperature. At this point we do not need to know the physical origins for the temperature dependence of the refractive index; we only need to know that such an effect is strong enough to detect. Being that the actual temperature fluctuation at the surface is only a few degrees or so, we can usually assume that the effect is linear.

The displacement signal comes from the phase modulation of the probing arm which is converted to an intensity modulation upon interfering with the reference:

$$i_{disp} \sim \left| E_{ref}\, e^{j\omega t} + E_{sam}\, e^{j(\omega t + 2ku_z \cos\omega_h t + \Delta\phi_{DC})} \right|^2 . \tag{3.9}$$

Here, $\Delta\phi_{DC}$ is the DC phase offset, or set point, between the two arms, k is the optical propagation constant, and u_z is the surface displacement. Expanding, we get

$$i_{disp} \sim E_{ref}^2 + E_{sam}^2 + 2E_{ref}E_{sam}\cos(2ku_z\cos(\omega_h t) + \Delta\phi_{DC}) . \tag{3.10}$$

Under optimal conditions, the power in each arm is the same, $E_{ref} = E_{sam}$. Furthermore, since ku_z is very small we can simplify the above to

$$i_{disp} = \frac{1}{2}\eta P_p [\, 1+\cos(\Delta\phi_{DC}) \,] + \frac{1}{2}\eta P_p \sin(\Delta\phi_{DC})\, 2ku_z\cos(\omega_h t) . \tag{3.11}$$

The first term is the DC power level; this term determines the shot-noise of this method. The second term is the signal. Note that while the signal peaks at $\Delta\phi_{DC} = \pi/4$, the maximum signal-to-shot-noise ratio occurs at the maximum of

$$\frac{S}{N_{shot}} \sim \frac{\sin(\Delta\phi_{DC})^2}{1+\cos(\Delta\phi_{DC})} , \tag{3.12}$$

or at $\Delta\phi_{DC} = \pi$. Although, in theory, there is a factor of 2 improvement at this set-point, the signal becomes vanishingly small at $\Delta\phi_{DC} = \pi$, at which point the Johnson noise actually limits the improvement.

Finally, the slope-detection method involves measuring the lateral displacement of an optical probe beam specularly reflected off of the side of the heated bump. Referring back to Figure 3.3, the lateral displacement of the reflected beam is approximately $2\delta f$, where δ is the slope of the surface. (It should be noted that since the probe beam has a finite spot size it will not always see a simple tilted surface, as assumed, but rather a curved surface if it is near a point-like expansion. The curvature of the surface will distort the beam as well as displace it, but for our purposes we will assume that the signal strength is proportional to the radial slope at the point of detection.) If the reflected beam is centrally located on a split detector, the displacement will give rise to a signal of approximately

$$i_{slope} \cong \frac{\eta P_p}{\pi r^2} \times 2rd = \frac{4\eta P_p}{\pi NA} \delta \cos(\omega_h t) . \tag{3.13}$$

The signal strength is *inversely* proportional to the numerical aperture; for a for given lens aperture, the lateral displacement increases with focal length. Hence, low NA lenses give rise to larger signals. This benefit is offset by the fact that the resolution of the probe beam is directly proportional to the NA. The optimum balance depends on the requirements of the sample being tested. We will return to this point below.

The signal power is $\langle i^2 \rangle R_L$ which gives the following expressions for the signal-to-noise ratio of the three methods:

$$\left(\frac{S}{N}\right)_{dR/dT} = \frac{\frac{1}{2}(\eta P_p)^2 \left[\frac{dR}{dT}\theta_o\right]^2 R_L}{2q\eta P_p R_L B + 4k_B TBF} \tag{3.14}$$

$$\left(\frac{S}{N}\right)_{displ.} = \frac{\frac{1}{2}(\eta P_p)^2 (ku_z)^2 R_L}{q\eta P_p R_L B + 4k_B TBF} \tag{3.15}$$

$$\left(\frac{S}{N}\right)_{slope} = \frac{\frac{8}{(\pi NA)^2}(\eta P_p)^2 \alpha^2 R_L}{2q\eta P_p R_L B + 4k_B TBF} \tag{3.16}$$

Ideally, we would like to operate in a regime where even the thermal noise is negligible. For this to occur we need

$$P_p R_L >> \frac{4k_B TF}{2q\eta} \cong 0.1\ W\Omega . \tag{3.17}$$

The load resistance determines the speed of the detector and has an upper limit of about 50 $k\Omega$ for operating frequencies up to 200 kHz (the range of the lock-in). Therefore, the optical power at the detector must exceed about 20 μW for shot-noise-limited detection. This condition is easily satisfied in all of the non-destructive evaluation experiments. (In

some of the high-T_c superconductor measurements the thermal noise is still significant, because of the need for extremely low laser powers.) Assuming that this condition has been met, the smallest fluctuations we can detect are

$$\theta_{o\,min} = \left(\frac{qB}{\eta P_p}\right)^{1/2} \times 2\left(\frac{dR}{dT}\right)^{-1} \cong 3\times 10^{-3}\ K/\sqrt{Hz}\ , \tag{3.18}$$

$$u_{z\,min} = \left(\frac{qB}{\eta P_p}\right)^{1/2} \times \sqrt{2}\,\frac{1}{k_{opt}} \cong 3\times 10^{-5}\ \text{Å}/\sqrt{Hz}\ , \tag{3.19}$$

$$\alpha_{min} = \left(\frac{qB}{\eta P_p}\right)^{1/2} \times \left(\frac{\pi NA}{2}\right) \cong 1\times 10^{-4}\ \text{Å}/\mu m/\sqrt{Hz}\ . \tag{3.20}$$

The numerical estimates are based on typical operating conditions ($P_p = 1$ mW, $\eta = 0.7$, NA = 0.5, and $\lambda_{opt} = 800$ nm) and a value of 10^{-5}/K for dR/dT. These formulas demonstrate the extraordinary sensitivity of these methods. By carefully removing all but the shot noise, we can measure small fractions of a Kelvin and thousandths of an Angstrom. (It should be emphasized here that these are AC quantities; lock-in detection is essential to limit the noise bandwidth.) This degree of sensitivity is needed, however, because the sample fluctuations are minute as well.

3.5 Comparison of Signal Strengths

If we wish to know which method will give rise to the strongest signal in our particular sample, we need to put these expressions in common terms. Usually, the pump power is restricted by an upper limit on the DC surface temperature. This limit might be a damage threshold or, as in the high-T_c superconductor work, a need for the surface temperature to be the same as the bulk. Furthermore, we need to define our resolution when making a comparison. As we saw in Chapter 2, for example, the displacement

method gives very large signals at low frequencies, but only at the expense of lateral resolution. Therefore, the comparison we seek will be a function of both $\theta_{DC\,max}$ and r_{res}. We will assume that all of the methods use the same probe power so the ηP_p terms can be dropped.

Starting with the reflectivity measurement, the radius of the temperature profile is determined by the size of the heating spot rather than the modulation frequency, so to obtain a resolution of r_{res} we must use a source with $r_h = r_{res}$. Having set the beam radius, the signal is maximum at low frequencies where the DC and the AC temperature changes are equal. Thus, the largest signal we can safely generate is

$$i_{dR/dT} = \frac{dR}{dT}\,\theta_{DC\,max}\,. \tag{3.21}$$

In the displacement method, the optimum operating conditions are not as obvious due to the trade-off between signal strength and resolution. We can either use a large heating spot ($r_h = r_{res}$) and operate at high frequencies to preserve the resolution, or we can use a very small heating spot ($r_h << r_{res}$) and operate at low frequencies. The first approach allows us to use a stronger heating beam since the energy is spread out over a larger area. Its drawback is that the frequency must be in the one-dimensional regime, where the response is weak. The second approach allows us to work in the low-frequency regime where the displacement is quite large, but the smaller heating spot means that less energy can be delivered to the sample in the first place. Using equation (2.56) for the displacement, u_z was calculated for a wide range of spot sizes and frequencies, and the calculations showed that, as one might expect, the signal is greatest between these two extremes. Typically, the best approach is to set $r_h = 0.5 r_{res}$ and use the frequency where $|k_t| r_{res} = 1$. Under these conditions, the integral in (2.56) equals 0.75 giving

$$u_z \cong 0.18\,\frac{\alpha}{\kappa}\,P_h\,, \tag{3.22}$$

where P_h is the pump power. Again, P_h is limited by the maximum allowable DC temperature change. We can relate P_h to $\theta_{DC\ max}$ by using (2.26) for the surface temperature of a heated slab. Assuming a Gaussian source we get

$$P_h = \sqrt{\pi}\left(\frac{r_{res}}{2}\right)\kappa\theta_{DC\ max}\,. \tag{3.23}$$

Thus the largest displacement signal we can generate is

$$i_{disp} = ku_z \cong 0.16\,k\,\alpha\,r_{res}\,\theta_{DC\ max}\,. \tag{3.24}$$

Given an optical wavelength of 800 nm, this expression becomes

$$i_{disp} \cong 1.3\ \alpha\,r_{res}\,\theta_{DC\ max}\,. \tag{3.25}$$

where r_{res} is in microns.

To complete the comparison, we need to calculate the slope signal. The slope method is similar to the reflectivity method in that both amplitude and the resolution level off to finite DC values at low frequencies. Therefore, we can use the DC formula to determine the proper heating spot radius. Equation (2.56) gives the general formula for $u_z(r)$. Replacing J_0 by $-\lambda J_1$ and letting k_t go to zero, we get

$$\frac{\partial u_z}{\partial r} \cong \frac{1}{2-v^2}\,\frac{\alpha'}{2\pi\kappa}\int_0^\infty H\left(\frac{\lambda}{2\pi}\right)J_1(\lambda r)\,d\lambda\,. \tag{3.26}$$

For a Gaussian beam, the integration can be carried out analytically to give

$$\frac{\partial u_z}{\partial r} \cong \frac{1}{2-v^2}\,\frac{\alpha}{2\pi\kappa}\,\frac{P_h}{r}\left[1 - e^{-(r/r_h)^2}\right]. \tag{3.27}$$

This expression peaks at a radius of $r = 1.12\,r_h$ so that the maximum slope is

$$\left(\frac{\partial u_z}{\partial r}\right)_{max} \cong 0.076\,\alpha\,\frac{P_h}{\kappa\,r_{res}} = 0.13\,\alpha\ \theta_{DC\ max}\,. \tag{3.28}$$

This slope corresponds to a signal strength of

$$i_{slope} = \frac{4}{\pi NA} \times 0.13\ \alpha\ \theta_{DC\ max}\,. \tag{3.29}$$

The numerical aperture is related to the resolution of the probe beam. For a uniformly filled lens the radius to the first zero of the Airy diffraction pattern is 0.66 λ/NA. Since we have defined our resolution as the half-maximum radius, we use r = .3λ/NA as our definition of the probe resolution. We further assume that for the slope experiment to have a total resolution of r_{res}, the heating beam must have at least the same resolution as the probe beam. Therefore, we get our final form for the slope signal in terms of the DC temperature limit and the resolution:

$$i_{slope} = 0.7\ \alpha\ r_{res}\ \theta_{DC\ max}\,. \tag{3.30}$$

Let us collect the three expressions for the DC-temperature-limited signal amplitudes for comparison (again, r_{res} is assumed to be expressed in μm),

$$i_{dR/dT} = \frac{dR}{dT}\ \theta_{DC\ max}\,, \tag{3.21}$$

$$i_{disp} \cong 1.3\ \alpha\ r_{res}\ \theta_{DC\ max}\,, \tag{3.25}$$

$$i_{slope} \cong 0.7\ \alpha\ r_{res}\ \theta_{DC\ max}\,. \tag{3.30}$$

Note that the surface displacement and the slope methods are roughly comparable for all samples. Both depend on the thermal expansion coefficient, α, and both increase as the resolution requirement is relaxed. The displacement signal increases at larger r_{res} because we can increase the spot size and lower the frequency; the slope signal increases because we can lower the NA and work with a longer lever arm. The displacement method has one further advantage in that it is a measure of the actual AC temperature fluctuation, as

opposed to the *change* in AC temperature detected by the slope method. Hence, when we image electrically heated samples, the displacement image shows entire heated regions, while the slope method only shows edges.

The reflectivity signal, however, is independent of the resolution. Hence, as we tighten the resolution requirement, it fares comparatively better. Note that at an optical resolution of a micron or so, the comparison between the reflectivity and the displacement methods reduces to simply that of dR/dT vs. α. Both quantities are commonly in the 10^{-6} to 10^{-4} range, so the proper method will depend on the particular sample being studied. For example, in the measurements on silicon and on high-temperature ceramic superconductors, dR/dT was found to be greater than the thermal expansion coefficient, but in the work on graphite and on titanium-coated quartz, dR/dT was negligible and the slope method worked better. In the lower-resolution (10 μm to 50 μm) NDE measurements on silicon, the displacement method works best, as the equations above imply.

3.6 Experimental Check of the Sensitivity

As a check of some of the calculations above, we used the interferometric methods to measure the vibration of a piezoelectric transducer split into halves, one stationary and one active. The DC phase offset was adjusted to maximize the signal ($\Delta\phi_{DC} = \pi/2$). The top trace of Figure 3.8 is the signal for a 10 mV driving voltage across the transducer. We can use this trace to calibrate the transducer. In this case, the DC voltage at the photodetector was 3.5 volts and the AC gain was 450. Using these data in (3.11), we conclude that u_z is 3.4×10^{-3} Å. Therefore the transducer response, in this frequency range, is 0.34 Å/V.

The center trace is the optical-noise floor, measured in a 25 Hz bandwidth, with the transducer turned off. This level corresponds to an equivalent surface vibration of 3.4×10^{-4} Å, which is very close to the theoretical limit of 3.0×10^{-4} Å given by (3.19).

The lowest curve is the level with the laser turned off, or the Johnson noise. For a DC voltage of 3.5 V, the above formulas for the noise predict that the Johnson level should be about 1/50 of the shot-noise level.

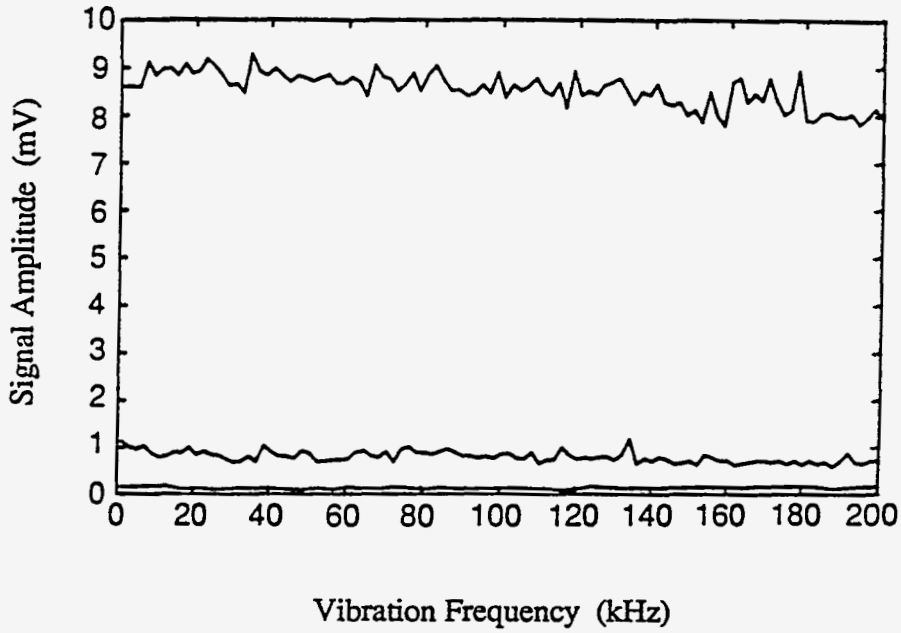

Figure 3.8 Displacement signal for a 3.4×10^{-3} Å vibration (top trace) compared to the optical noise level (center trace) and the Johnson noise level (lower trace). The Wollaston detector was used to measure the displacement.

Finally, the experiment was repeated with the Mirau interferometer to demonstrate the importance of removing the sample vibrations. The measured surface displacement, shown in Figure 3.9, clearly suffers from unwanted sample vibrations. The driving voltage of the transducer in this case is 100 times that used in the top trace of Figure 3.8 so that shot-noise fluctuations are negligible. Instead, we see wild fluctuations in the frequency response with clear resonances beginning at 60 kHz. (Resonances this low in frequency correspond to flexing modes in the large tungsten backing plate upon which the

piezoelectric mirror was mounted.) Unless the sample can be properly damped, resonances such as these overwhelm the response.

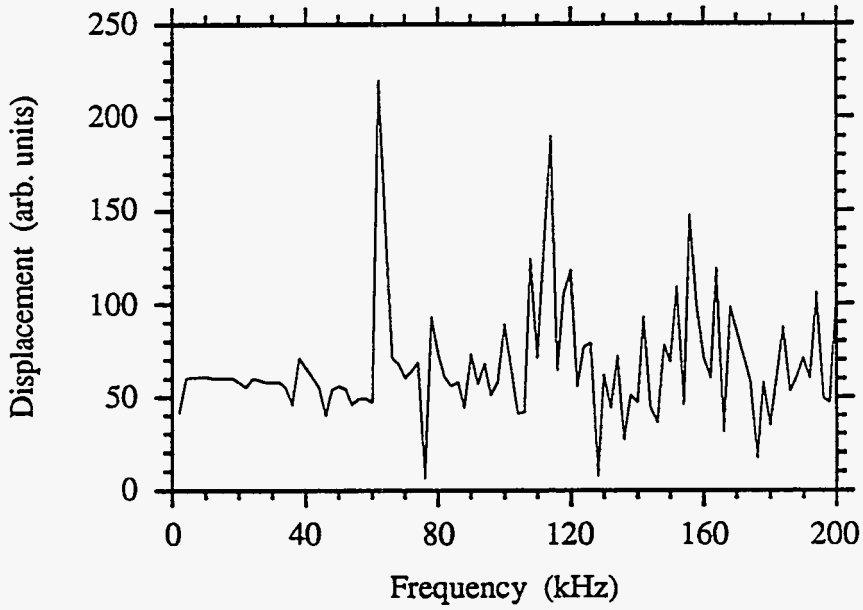

Figure 3.9 Displacement as measured by the Mirau interferometer, clearly demonstrating sample resonances.

Chapter 3 References

1. M.A. Amer, N.M. Olmstead, S Kohn, D. Fournier, and A.C. Boccara, "Photothermal displacement spectroscopy: An optical probe for solids and surfaces," *Appl. Phys. A* **32** (1), 141 (1983)
2. Y. Yamamoto and T. Kimura, "Coherent optical fiber transmission systems," *IEEE J. Quantum Elect* **QE-17**, 919 (1981).
3. Stanley S.C. Chim and G. S. Kino, "The correlation microscope," to appear in May 15 issue of *Optics Lett.*

Chapter 4

Photothermal NDE

4.1 Introduction

Photothermal microscopy finds its greatest applications in the field of non-destructive evaluation (NDE). The usual purpose of these measurements is to locate discontinuities in the thermal properties of the sample. These include surface or sub-surface cracks, poor adhesion and bonding, and delaminations of layered materials. These types of flaws are often undetectable optically, so either thermal or acoustic methods must be employed. An advantage of photothermal techniques is the ability to achieve optical resolution without contacting the sample and without the need for a coupling medium. Unlike acoustic or optical methods, they are also useful for locating electrical flaws through the detection of ohmic heat.

In any photothermal measurement we have two quantities at our disposal, amplitude and phase. Most often, images are based on the amplitude of the temperature as a function of position; defects are detected by their influence on the temperature profile. Phase can be equally valuable, however, since it can be used to measure distances such as the depth of a sub-surface flaw or the thickness of a film in a layered medium. Furthermore, in cases where distances are known accurately, the phase can provide accurate quantitative measurements of the thermal diffusivity, without the need to know the thermal expansion coefficient or the reflectivity. This feature is essential to the work on high-T_c superconductors in Chapter 5.

This chapter presents a sampling of the capabilities of our system, with emphasis on the types of measurements that require high resolution and sensitivity. Most of the

imaging is qualitative, the emphasis being to locate flaws and to compare the relative strengths of the different approaches analyzed in Chapter 3. In the final chapter, we will change the emphasis and concentrate on quantitative measurements of the thermal constants.

4.2 Imaging of Disbonds and Cracks

The principle behind thermal imaging of cracks and delaminations is that breaks in the material hinder heat flow and alter the temperature distribution. For example, if the heat source is located within a thermal diffusion length of a vertical crack, as shown in Figure 4.1a, lateral heat flow is obstructed and the AC temperature on the source side of the crack increases. If the crack is severe enough to act as a perfect insulator, the temperature on the hot side of the crack is identical to that of the system in Figure 4.1b where an image source has been added an equal distance on the other side, in a manner similar to that in electrostatics. For partially transmitting cracks, the magnitude of the image source corresponds to the reflected component of the thermal wave.

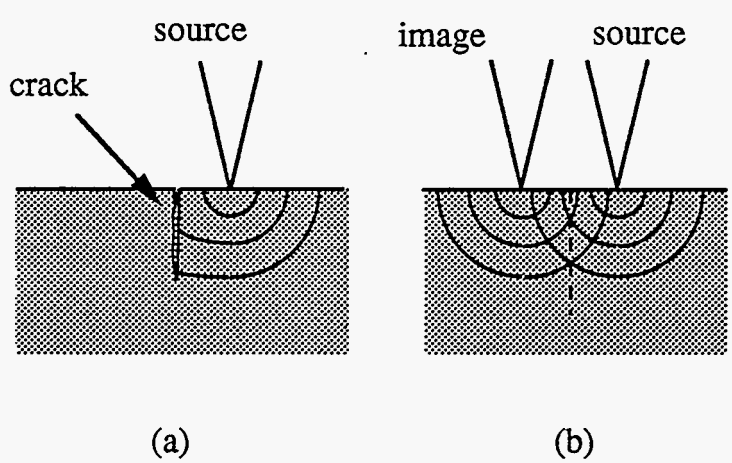

Figure 4.1 Effect of a perfectly-insulating crack on the temperature profile (a). An equivalent system (b).

For the perfectly insulating crack, one might expect the temperature to double as the heating beam approaches it from the side (or merges with its image beam). However, the beam has a finite size so that a portion of it is cut off as it nears the crack. Hence the actual temperature increase is substantially smaller, depending somewhat upon the beam profile and the operating frequency. For accurate predictions, we need to use a modified form of the 3-dimensional theory of Chapter 2. To include vertical cracks in the theory, we recast the equations in Cartesian coordinates and add the image source to the heating function, h(x,y). Delaminations and multi-layered media are also included in the model by adding the appropriate solutions for each layer and matching the boundary conditions at each interface (continuity of temperature and heat flow).

Figures 4.2 and 4.3 show the predicted change in the temperature and displacement at the center of a Gaussian heating spot as it approaches a perfectly insulating vertical crack. We see that the changes are only a few percent, with somewhat larger values at low frequencies. We also note the displacement is affected more than the surface temperature, due to its dependence on the temperature through the bulk.

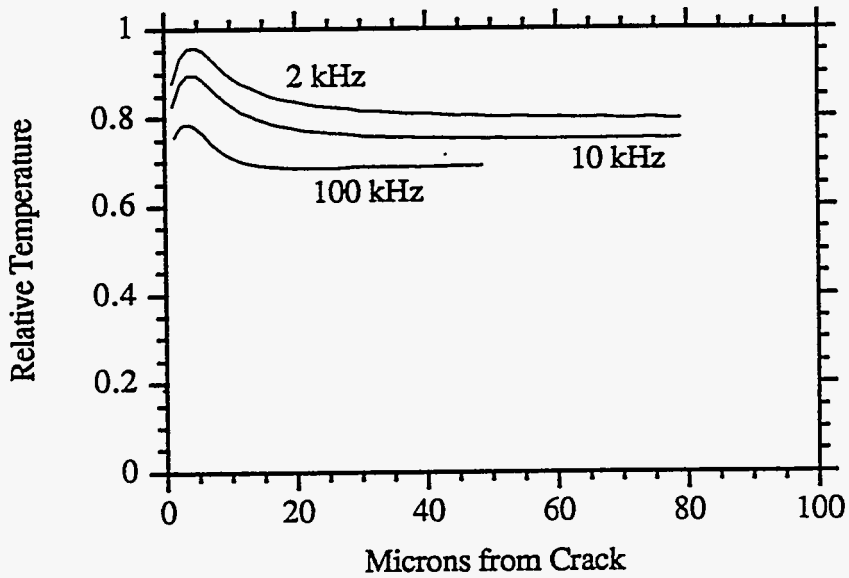

Figure 4.2 Theoretical plot of the AC temperature as the lasers are scanned over a crack.

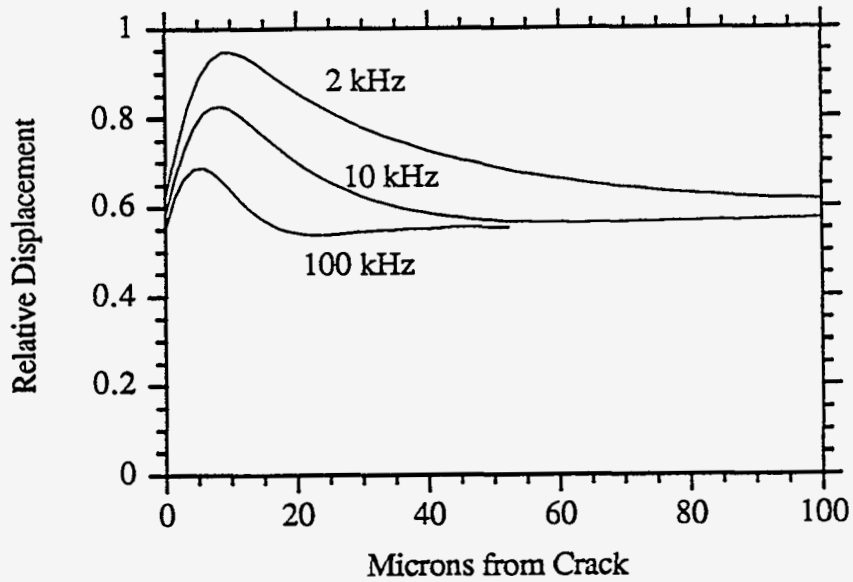

Figure 4.3 Theoretical plot of the AC surface displacement as the lasers are scanned over a crack.

We therefore used the displacement method to measure the effect of a crack and to check the calculations. The "ideal crack" in this case was actually the cleaved edge of a silicon wafer coated with 300Å of chrome-gold to confine the source to the surface. The plots of the signal strength, in Figure 4.4, show about a 20% increase near the edge, in fair agreement with the model both in magnitude and in the frequency behavior.

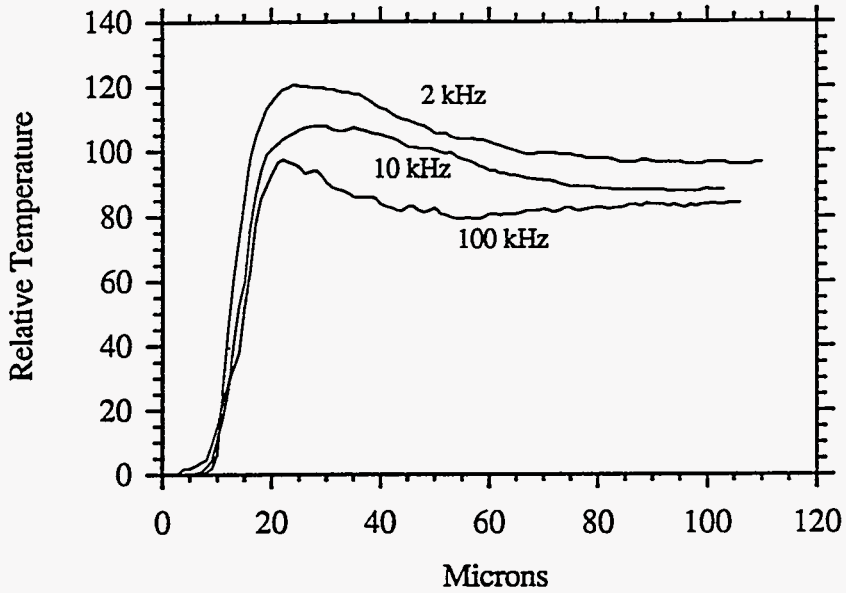

Figure 4.4 Measured surface displacement as the lasers are scanned over a crack.

While the displacement method is more sensitive to vertical cracks, sensitivity is not the only issue. In practice, deep cracks can affect the *acoustic* propagation as well, so that the local thermal expansion is mixed with the long-wavelength sample vibrations. In these situations, the data is difficult to interpret. Figure 4.5 is an example of this point; it is a plot of the measured displacement when scanning over a deep crack in a glass slide using the Wollaston interferometer. To demonstrate the problem more clearly, the heating and probe beams were separated by 10 μm as shown in the figure. The reference beam was a further 100 μm away. As we scan the system over the crack, we see a very small increase in the signal as the heating beam approaches the crack (region 1) followed by a null region where the crack is between the heating and probe beams. When the crack lies between the probe and reference, the signal jumps by a factor of three. Here we are seeing both thermal and acoustic fluctuations. In a 2-D thermal image it would be difficult to sort these two contributions since they depend not only on the location of the crack relative to the probe, but also on the placement and orientation of the reference beam. Although some of the

ambiguity can be removed by switching to a Mirau interferometer, this method has no ability at all to discriminate between thermal and acoustic displacements. Therefore, in the detection of vertical cracks, displacement methods are somewhat limited.

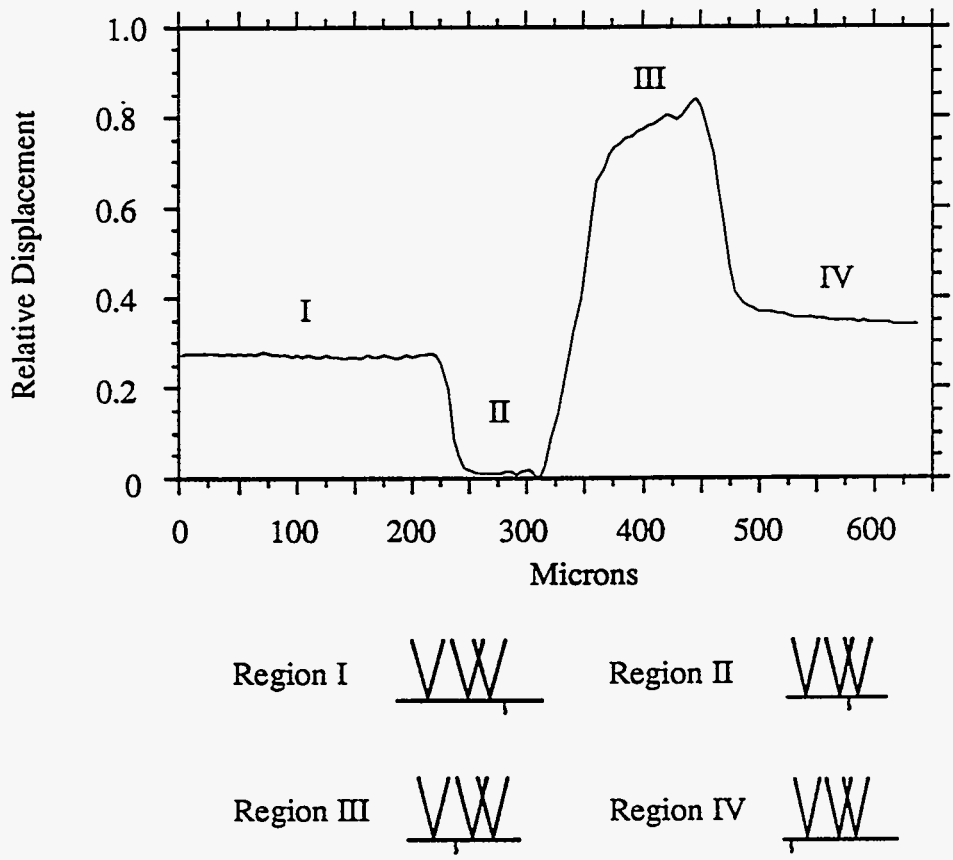

Figure 4.5 Displacement signal, using the Wollaston prism detector, showing the acoustic effects of a crack.

Images based on the change in reflectivity with temperature (dR/dT) do not suffer these effects. Figures 4.6a and 4.6b are 2-dimensional optical (reflectivity) and thermal (dR/dT) images of the ac-plane of a single-crystal Bi-Ca-Sr-Cu-O superconducting fiber. Since this sample was being used to study the anisotropy of the thermal conductivity of Bi-Ca-Sr-Cu-O, it was important to work in a region free of cracks or separations that might

alter the data. These images were taken using a 0.6 NA microscope objective and have an optical (and thermal) resolution of about 1 μm. The entire image is about 35 μm wide with a pixel size of about 1/2 μm.

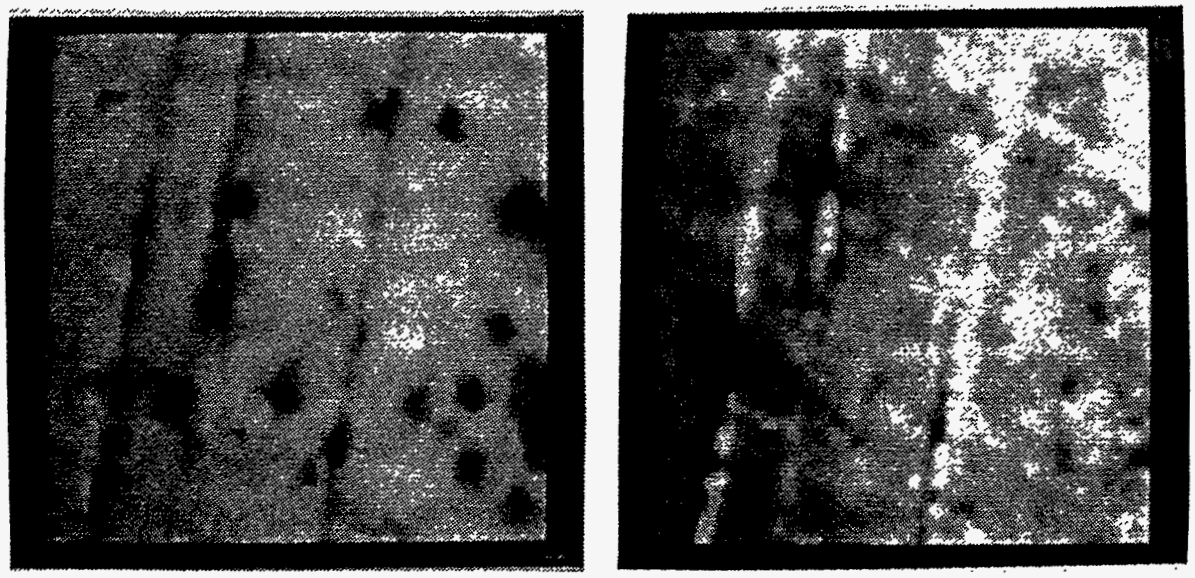

(a) (b)

Figure 4.6 Optical image (left), made by recording the DC component of the reflected probe beam, and photothermal amplitude image (right), using dR/dT method, of the ac-plane in a single-crystal $Bi_2Sr_2CaCu_2O_x$ fiber.

The optical image on the left was made by recording the DC intensity of the reflected probe beam as a function of position. We can clearly see three large vertical scratches (a result of the polishing of the surface) and a number of dark spots caused by excessive laser heating from a previous experiment. The enhanced thermal image on the right contains not only the scratches, but a couple fine horizontal lines as well. These lines subsequently were found to coincide with the ab-planes, implying that they represent fine cracks or separations between the planes. The importance of this measurement is that these

types of flaws were not visible optically, but clearly affect the thermal properties. It is also interesting that the burn marks we saw in the optical image apparently have no effect on the thermal behavior. (As with all measurements in this thesis, simple changes in reflectivity are normalized out of the thermal image).

The surface temperature changes in the vicinity of transverse cracks, or delaminations, in much the same way it does for vertical cracks. Figures 4.7a and 4.7b are optical and thermal images of two types of gold film on a silicon substrate. The film at the top of the image was deposited directly onto the silicon and is easily peeled away, while the lower, I-shaped film has an intermediate 50 Å layer of chrome to improve the adhesion. The thermal images reveal that the poorly bonded film has poor heat transfer, especially at the edges where a small amount of lift-off occurs. (The bright spots along the edge and the jagged nature of the optical image are due to the quantization and extreme magnification of the image. Each pixel represents a 5 μm square.) A more striking demonstration of an adhesion problem is shown in Figure 4.8. Taken in the interior regions of the film, this thermal image reveals a kidney-shaped region of poor bonding caused by a small blister that was completely invisible in the optical image. The image is 50 μm on a side.

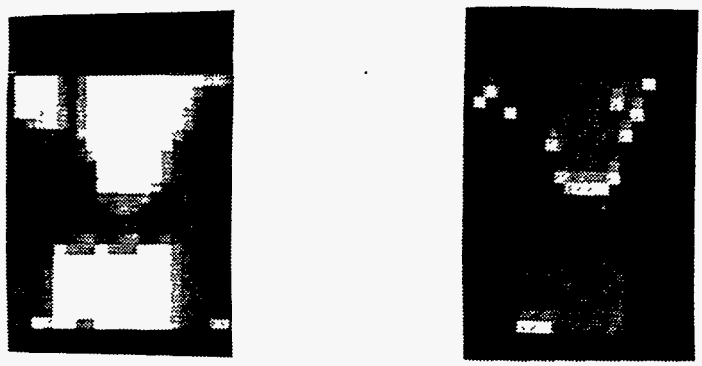

(a) (b)

Figure 4.7 Optical and thermal images of two gold films on a silicon substrate. Edges in the thermal image indicate a lifting off of the film.

Figure 4.8 Thermal image of a blister in the gold film. The blister was undetectable optically.

4.3 Imaging of Electrical Samples

The goal in NDE of electrically heated samples is to map the thermal sources, rather than the thermal inhomogeneities of the material. Variations in temperature reveal those areas where the electrical resistance of current-carrying devices is high. One of the most useful aspects of photothermal microscopy is its unique ability to locate these types of defects.

There are fundamental differences between using internal and external heat sources for imaging. Since the size and number of internal sources are unknown, the resolution of the image is determined solely by the probe beam. This uncertainty complicates the use of Wollaston interferometry since the reference beam could be subject to thermal vibrations in

addition to the sensing beam. The resulting image will be a coherent double exposure, the deconvolution of which is non-trivial. In practice, however, we can usually place the reference in a source-free region by designing the optics so that the probe and reference beams are separated by a sufficiently large distance. The criterion that the separation be much less than an acoustic wavelength ultimately limits the separation, but since λ_{ac} ranges from 15 to 1500 mm over the common range of operating frequencies, this restriction is minor.

There is another complication in electrical NDE that affects the slope method. Unlike the situation with external, laser heating, the hot spots do not remain a fixed distance form the probe. Since the slope method is a measurement of the temperature *gradient*, thermal images of electrically-heated samples will show edges and points but will not give an indication of the absolute AC temperature. The interior regions of large heated areas will generate little or no signal.

As a simple example of electrically-heated imaging, we examined a flawed 250 Å thick nickel film deposited on an oxidized silicon wafer, shown in Figure 4.9a. The film was scratched with a razor blade and then heated at 16 kHz by passing an 8 kHz AC current through it. Because the area of the flawed region is fairly large, a low-resolution displacement method gives the strongest signal. We used the Wollaston interferometer with the probe and reference beams oriented as shown in the figure. The normalized AC thermal expansion image, Figure 4.9b, clearly shows the hot region where the current density is greatest. Figures 4.10a and 4.10b show the same area in a false-color contour plot (red being hot and blue being cold). These two images demonstrate the relationship between heating frequency and resolution. The image on the right was taken at four times the frequency and subsequently has about twice the resolution; the edge of the film is much more sharply defined.

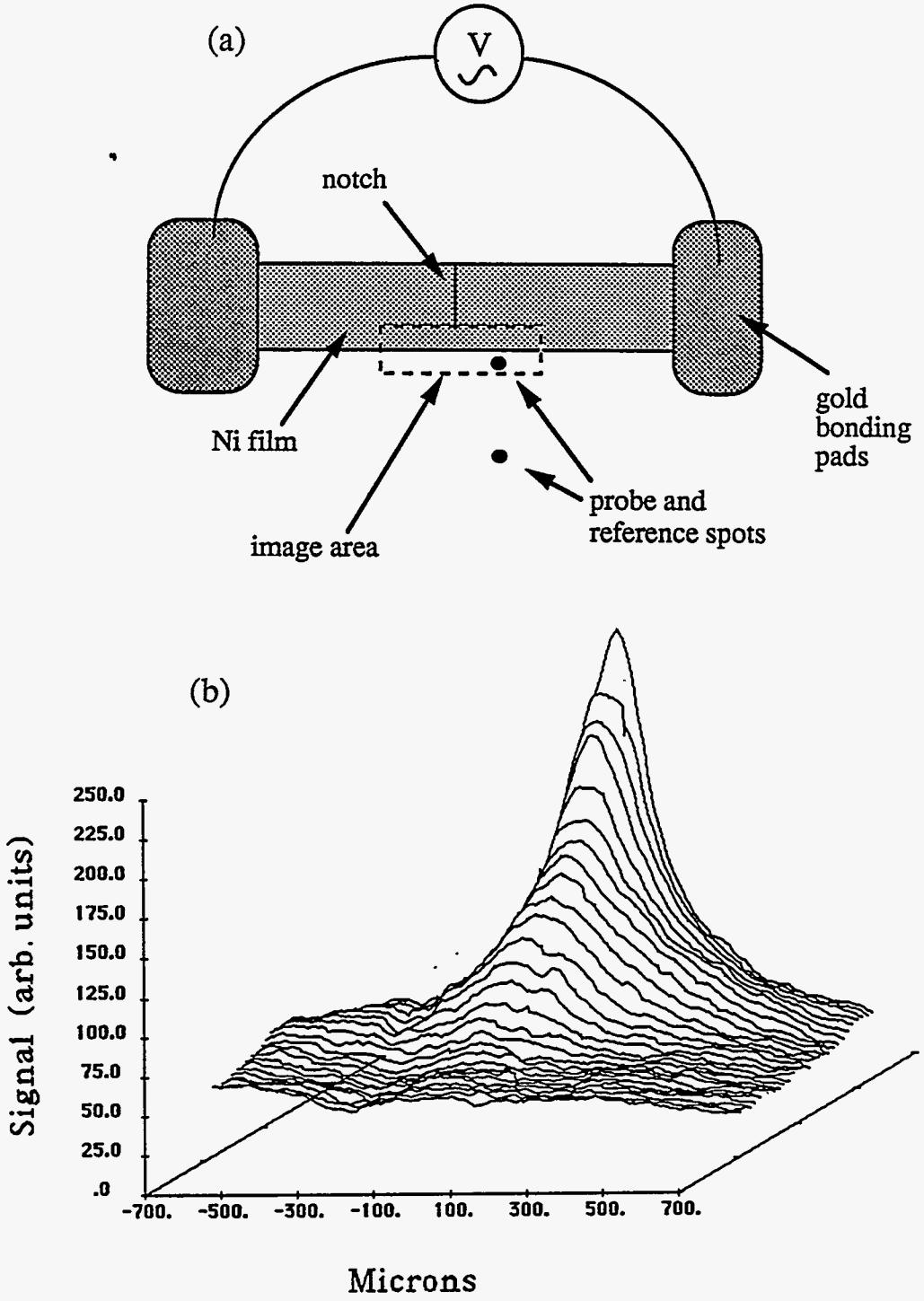

Figure 4.9 Sketch of the sample used in the demonstration of electrical-flaw detection (a), and the measured surface displacement in the vicinity of the flaw (b).

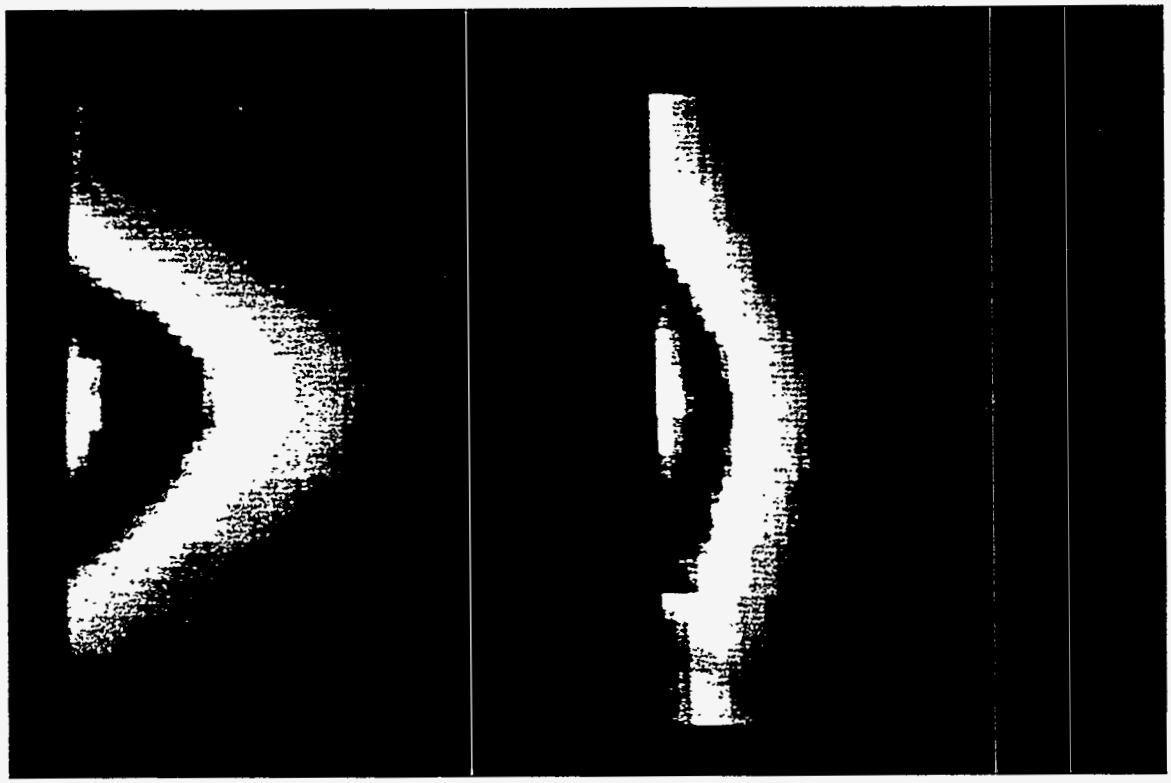

Figure 4.10 Color images showing the extent of the heated region.

Despite some of the practical difficulties of the Wollaston interferometer, the tremendous sensitivity we achieve makes them the method of choice in relatively low-resolution experiments such as these. To generate the images above, the driving voltage was 2 V peak-peak. The resistance of the film increased from 25 Ω to 35 Ω after notching so that about 1/3 of the total power was dissipated in the region of the flaw, an area roughly 200 μm square. Working through the numbers, we find that the peak power density at 16 kHz was roughly 5×10^4 W/m^2.

We can calculate the corresponding temperature fluctuation by using the theory of Chapter 2. Since the thermal wavelength in silicon is only 30 μm at 16 kHz, we were operating in the high-frequency regime. This is confirmed by the 1/f behavior of the peak

signal amplitude, shown in Figure 4.11 (note the roll-off starting at about 3 kHz where $\lambda_{thermal} = 70\ \mu m$). Therefore the one-dimensional formulas apply. Using (2.9),

$$|\theta_o| = \frac{I_o}{\sqrt{\omega C \kappa}}, \tag{4.1}$$

and the values for silicon, $C = 2300\ kg/m^3 \times 710\ J/kg\text{-}K$, $\kappa = 145\ W/m\text{-}K$, we find that the rms fluctuation was only 0.01°C at the hottest spot. The fluctuations in the outer regions were considerably smaller. The surface displacement is similarly calculated to have been only 0.01 Å at the peak.

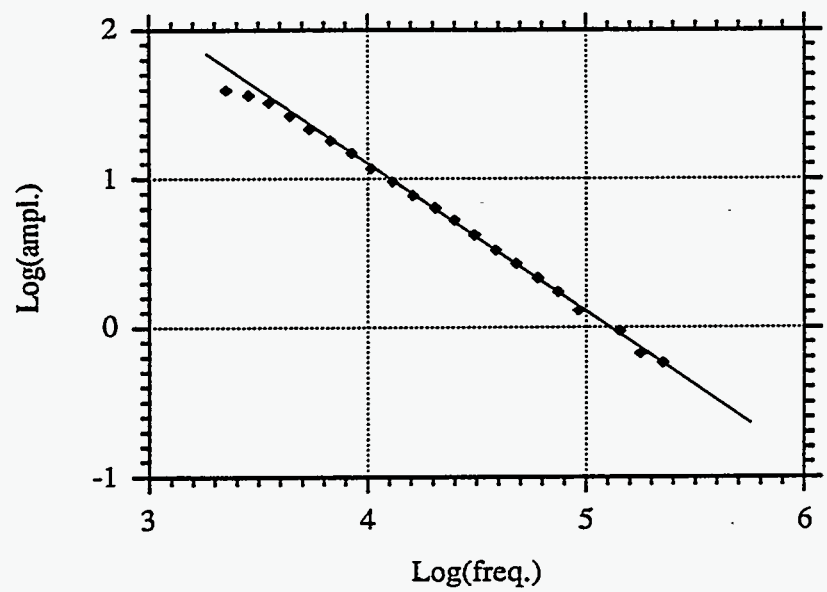

Figure 4.11 Frequency behavior of the surface displacement at the peak shown in Figure 4.9b.

To push the resolution of our thermal images to the optical limit, we need to use higher NA objectives than those used above. We also need to reconsider our choice of experimental method. As mentioned in Chapter 3, we can reduce the optical spot size of the displacement probe by switching to a Mirau interferometer. As we show below,

however, this method still suffers from poor resolution in most materials unless inconveniently high frequencies are used. As is often the case at these resolutions, measurements of dR/dT, rather than thermal expansion, give better results.

Figure 4.12 shows a sketch of the fine bar pattern to be tested. We wish to compare the current flow of the individual strip conductors. The films are aluminum, 300 Å thick, deposited on a silicon substrate (again, a 1000 Å oxide layer was grown on the silicon to confine the current to the film). The bars and gaps are both 6.7 μm wide. Electrical contact is made to the films through large gold pads covering the ends of the strips.

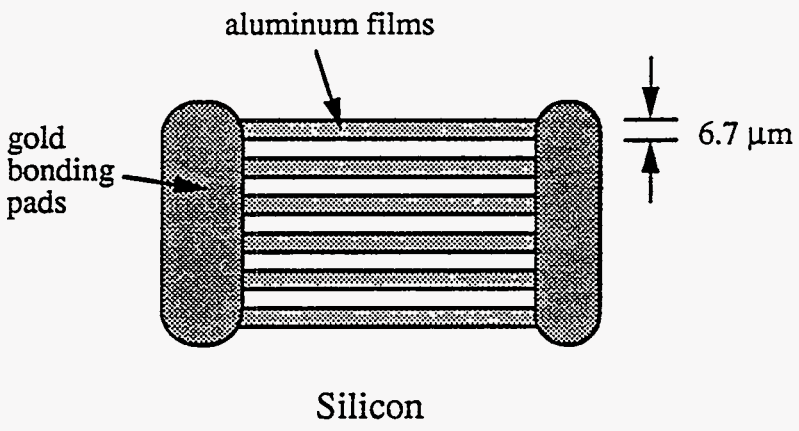

Figure 4.12 Sketch of narrow conducting strips to be imaged at high resolution.

Connecting the pads to a 2.5 V driving source, we generate the dR/dT profiles shown in Figures 4.13. These profiles are a measure of both the surface temperature (rather than displacement) and the temperature sensitivity of the refractive index. The six peaks correspond to the six aluminum strips. At 200 kHz, Figure 4.13a, the diffusion length in silicon is 8.4 μm, so the heat generated by each strip is essentially confined to that strip and individual variations in the current can be seen. In this device, we see that the second and fourth strips carry greater current and thus grow hotter.

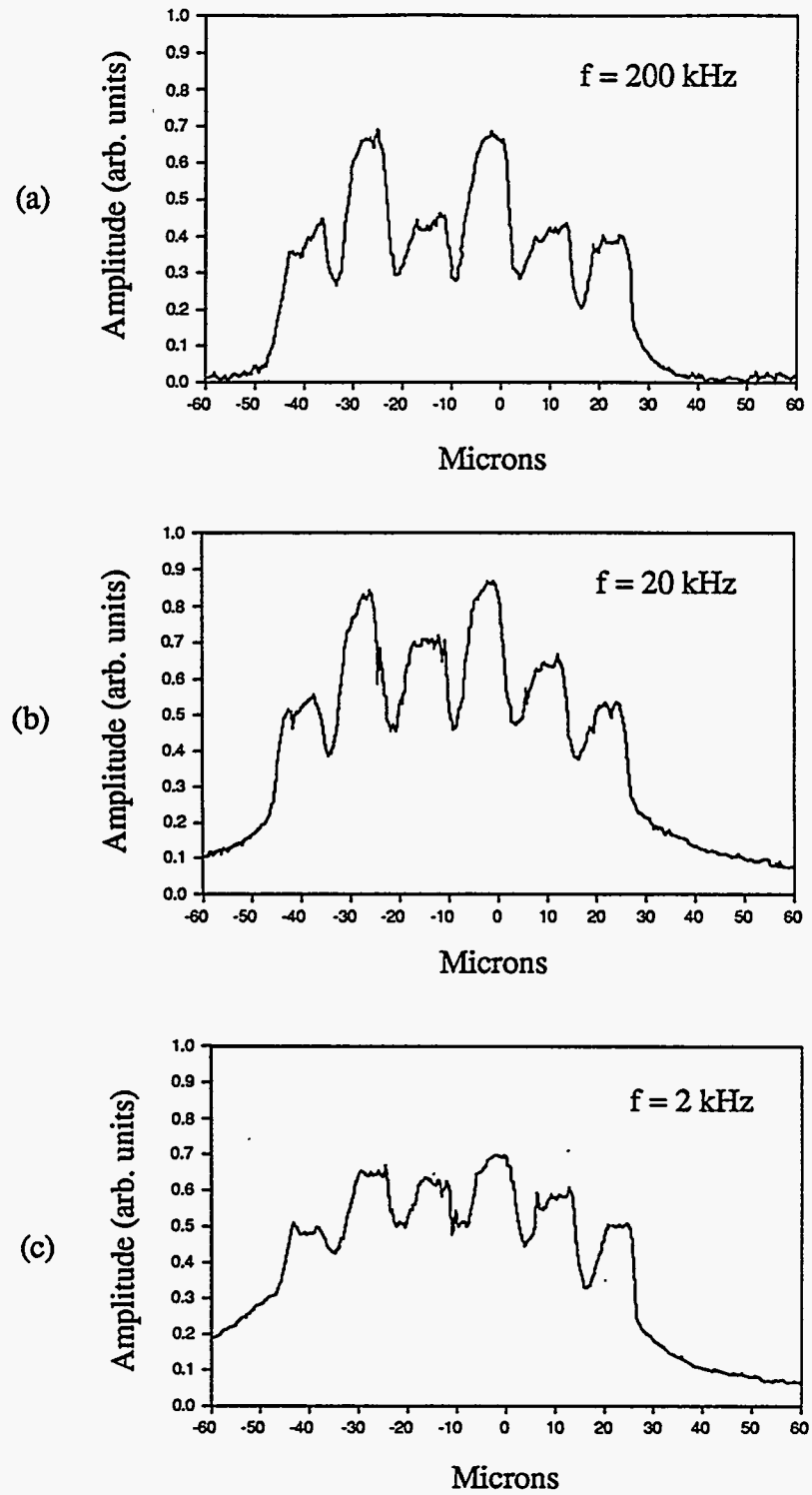

Figure 4.13 Profiles of measured AC reflectivity of the device shown in Figure 4.12. The six peaks correspond to the six conductors.

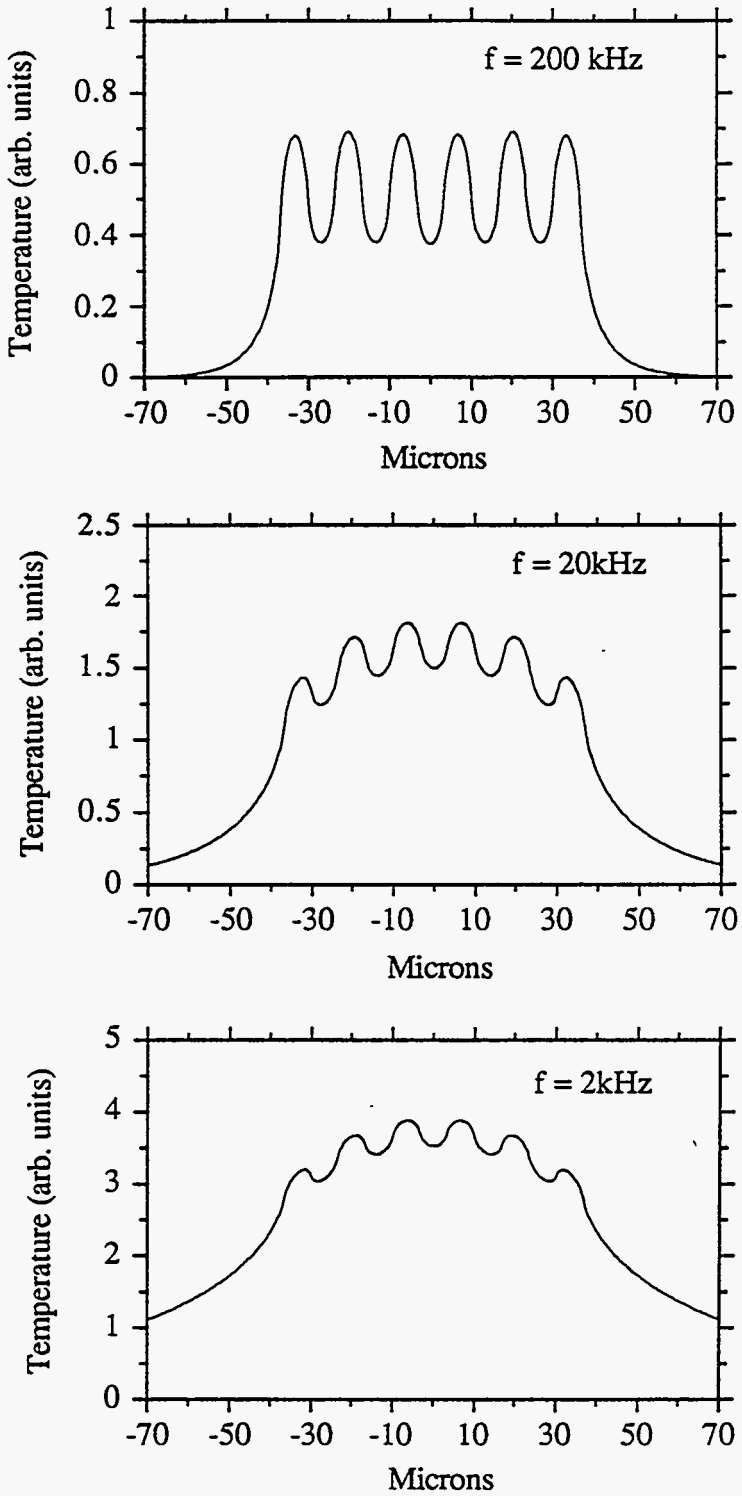

Figure 4.14 Theoretical calculation of the AC temperature profile at the three frequencies.

At 20 kHz, Figure 4.13b, λ_{th} is 26.6 μm and individual differences are less pronounced. The tails at either side of the group decay more slowly and there is an average increase in temperature at the center of the group. These trends continue at 2 kHz, or λ_{th} = 84 μm, (Figure 4.13c) where we completely lose the ability to differentiate the individual conductors. There is no indication that strips 2 and 4 are hotter. The residual peaks that are left are due more to the difference between the dR/dT of aluminum and of silicon than to actual temperature variations.

The theoretical predictions, Figure 4.14, confirm these measurements. The theory is a two-dimensional analogue of that in Chapter 2. We see the gradual diminishing of our ability to isolate individual strips as the frequency is lowered. Differences in dR/dT were not taken into account in this model so we can tell by comparison with Figure 4.13c that the refractive index of aluminum, at this wavelength, is roughly three times as temperature sensitive as the refractive index of silicon. Two-dimensional optical and thermal images are shown in Figure 4.15. We see that the heating is non-uniform along the length of the two hot strips.

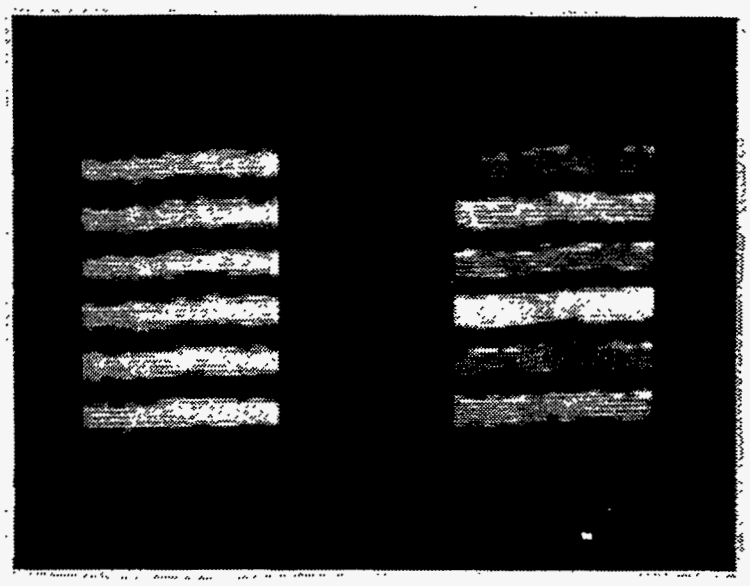

Figure 4.15 Two-dimensional optical (left) and thermal (right) images of the bar pattern.

If the experiment is repeated with an argon-laser probe beam (λ = 514 nm) an interesting change occurs. We see a reversal in the signal profile with the silicon giving rise to large fluctuations while the aluminum appears to be unheated. Figure 4.16 shows the DC optical image and the corresponding photothermal image which has a reversed pattern. The reason lies again in the refractive index sensitivities. Normally, the refractive index of metals is very weakly sensitive to temperature, however, aluminum happens to have a small resonance at 800 nm which means that common GaAlAs laser diodes are particularly well suited for the study of this material.

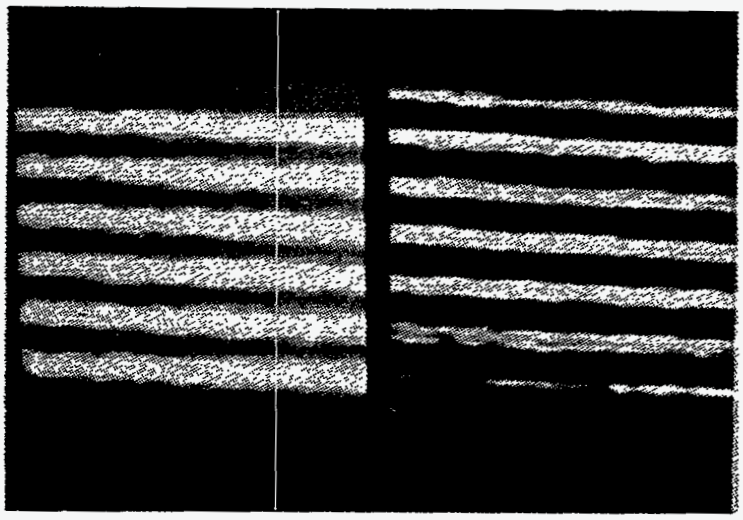

Figure 4.16 Optical and thermal images of the same device as in Figure 4.15 but taken using an argon laser probe rather than the usual diode laser probe. Note that the thermal image is the reverse of Figure 4.15 due to the small dR/dT of aluminum at the argon wavelength.

The theoretical model also predicts large displacement signals at 200 kHz (the top end of the lock-in) that, unfortunately, are too spread out to be of use, as shown in Figure 4.17. The Mirau measurements of Figure 4.18, normalized by the reflectivity, confirm the

prediction. (The sample was mounted in putty on a very sensitive tilt stage in order to damp out acoustic effects and to keep the set-point of the interferometer form drifting over the course of the 100 μm scan.) To obtain resolutions comparable with those of the dR/dT measurement, we would need to operate at about 1.5 MHz and mix down to the frequency range of the lock-in.

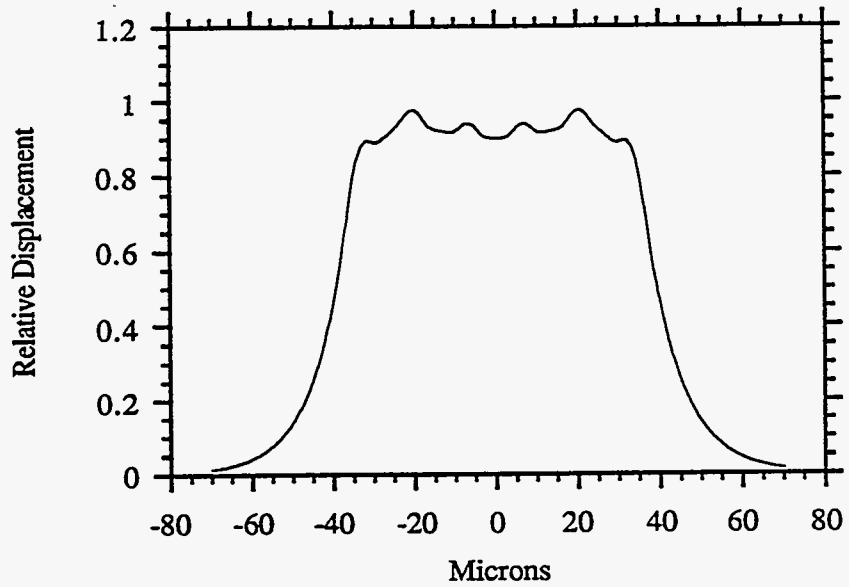

Figure 4.17 Theoretical calculation of the AC surface displacement at 200 kHz.

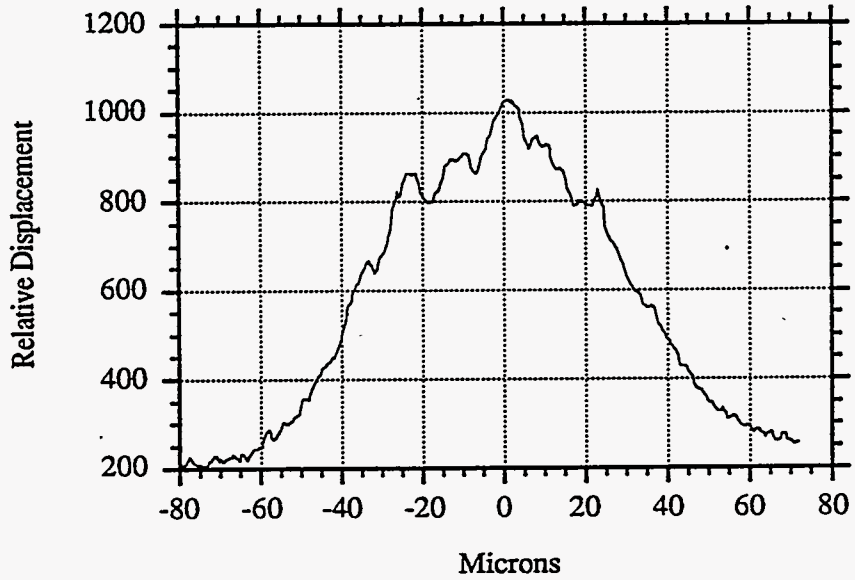

Figure 4.18 Measured displacement (Mirau method) at 200 kHz.

4.4 NDE of Silicon Flip-Chip Devices

We conclude this chapter with an example that requires all of the features of our photothermal probe, namely, its high resolution, high sensitivity, flexibility, and amplitude and phase detection. The challenge is to determine the location of electrical flaws in a silicon flip-chip device, shown in Figure 4.19. The device consists of a silicon substrate and four interconnect chips bonded together by hundreds of 50 μm radius solder bumps. The principle behind this type of architecture is to increase the component densities and shorten the interconnects by allowing direct access to the interior of the wafer rather than through leads run to the edges of the chip. These particular devices were used to test the manufacturing process and consisted of a stitch-work pattern of conducting films connecting the many bumps. They were made by depositing matched sets of bumps on the top and bottom wafers, aligning the wafers, pressing, and heating. After processing, most of the devices had poor electrical properties. The manufacturer wanted to know whether the problems were due to a minority of bad bonds or due to a generally poor process. Also of interest was whether certain regions were more prone to failure (e.g. edges versus the interior) and whether the disbond was due to incomplete bonding of the upper and lower bumps, or due to the bumps being pulled away from the substrate during cool-down. Hence, we need the ability to locate flaws accurately in all three dimensions.

What makes this sample such a challenge for thermal imaging is the small size and close proximity of the solder joints, and the 500 μm of silicon that obscures them. Methods that rely on ambient or surface effects, such as the Mirage or the deflection techniques, would be unable to sort out contributions from individual bumps since these contributions are severely attenuated and overlapping by the time they travel through 500 μm of silicon to the surface. The manufacturer also tried imaging with an IR camera but could not obtain sufficient resolution. What was needed was a method capable of

penetrating the silicon while retaining adequate resolution and sensitivity at the solder interface.

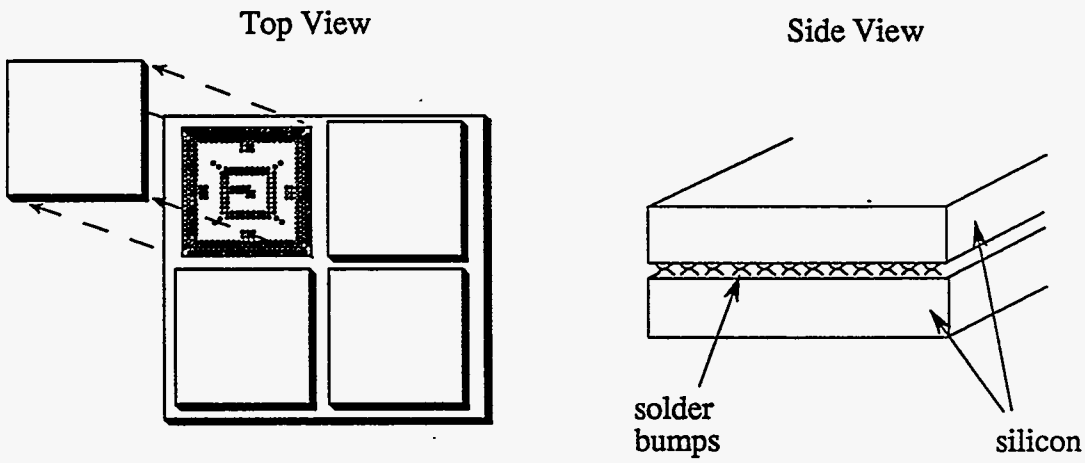

Figure 4.19 Schematic of the silicon flip-chip device.

We actually used two techniques for imaging the bumps at the interface. The mechanical characteristics were evaluated by C-H. Chou, and B. T. Khuri-Yakub [1] using a 50 MHz focussed acoustic microscope operating in water. The focussing is accomplished by a spherical depression in a quartz buffer rod, driven at the other end by a planar transducer. In order to focus through the silicon, a long focal length lens must be used (the acoustic velocity of silicon is six times that of water, requiring a focal length of at least 3.0 mm in water). Furthermore, a low numerical-aperture lens must be used to minimize the distortion of the beam upon changing media (the critical angle is only 10°). In order to isolate the reflections corresponding to the solder-silicon interface from the large reflection at the silicon-water interface, it was necessary to use tone burst excitations and to time gate the desired signal. While not necessary to obtain an image, the image was further improved when the back side of the wafer was polished to reduce the distortions caused by surface roughness.

Figures 4.20a and 4.20b show acoustic images of two sides of a flip-chip. The rows of solder bumps are very clear in this test pattern. On one side (Figure 4.20a), all of the solder bumps are visible as small dark circles where the acoustic reflectivity is low. On the opposite side (Fig 4.20b), however, it is apparent that a large number of bumps are completely disbonded. In this image, we see that only about 70 % of solder bumps make good mechanical contact.

In more successful devices, however, the bumps may appear to be in good mechanical contact but still have poor electrical properties. While the acoustic microscope can locate complete disbonds, it does not have the sensitivity to differentiate between good bonds and partial disbonds. These types of flaws are identified by their low electrical conductivity. We measured the conductivity of the individual bumps by passing an AC current through them and found that the electrical quality can vary dramatically in bumps that pass the acoustic inspection.

The most sensitive photothermal approach for this sample is, once again, the Wollaston interferometer. But rather than measuring surface displacement, which would be subject to the problems stated above, we switched to a 1.3 μm probe beam wavelength, which passes through silicon, to view the solder bumps directly. In this configuration, the optical phase shift is generated mainly by changes in the refractive index of the heated silicon neighboring the bumps. This effect is about ten times as strong as that of the thermal expansion, and extremely small temperature fluctuations can be detected. For example, the refractive index changes by about 1.5×10^{-4}/K, so that at 20 kHz the thermal wavelength is about 25 μm and the minimum detectable solder bump temperature is only $10^{-6}\sqrt{B}$ K. Hence, excessive currents are not necessary to generate the signals we need.

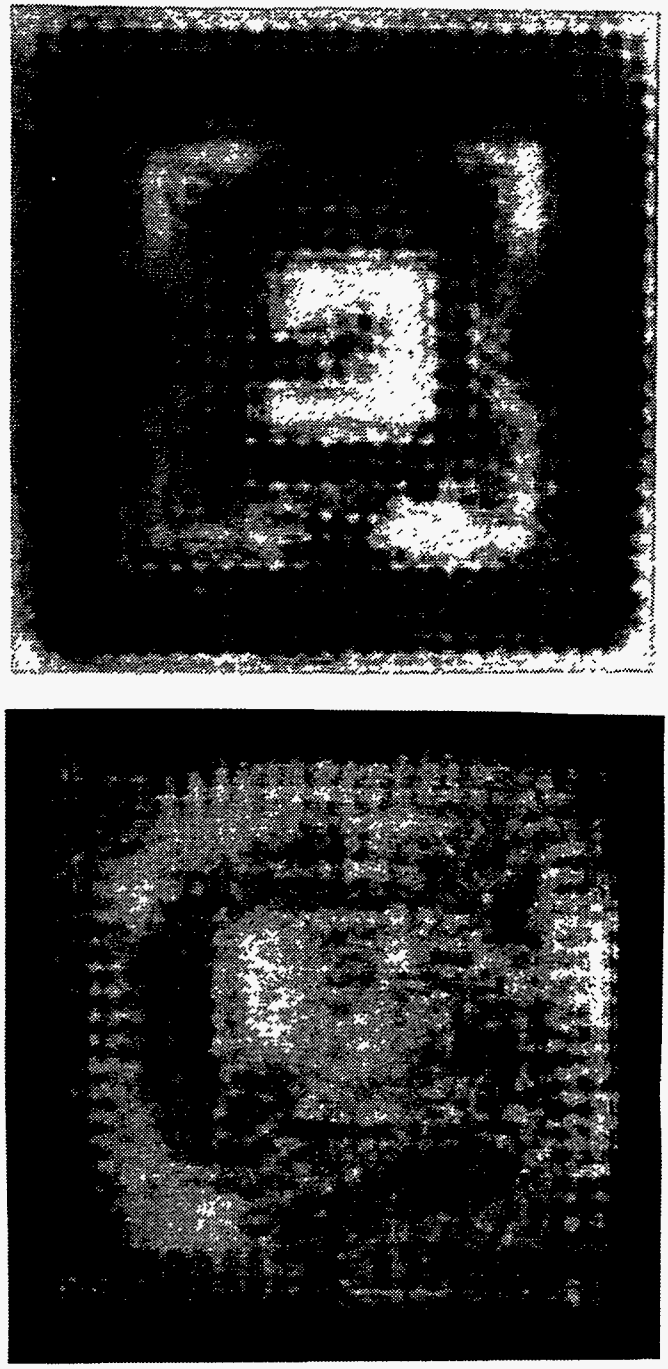

Figure 4.20 Acoustic images of the device. Dark circles represent the good bonds for which the acoustic reflectivity is low.

The results of a thermal scan are shown in Figure 4.21. This is a view of the outer row of bumps along one side of the device. (The top image is a linear grey-scale, the bottom image has had the lower levels enhanced to display the good bonds more clearly.) There are 24 bumps in this region, of which the 7 at the right are not visible because their electrical conductivity was too good to generate sufficient heat. Of the 17 remaining bonds, two in particular stand out, being about ten times hotter than the others. In the acoustic images, all 24 bumps look the same.

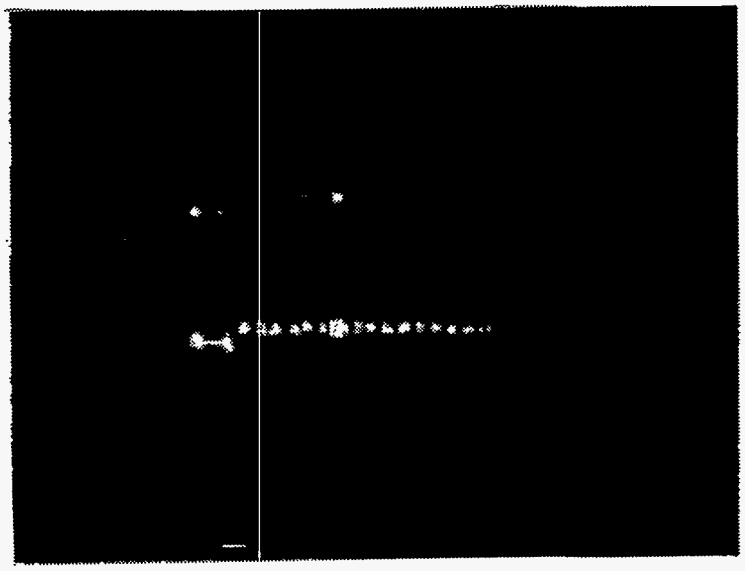

Figure 4.21 Thermal image of a single row of solder bumps.

Information about the depth of a flaw can be learned by examining the thermal signal as a function of frequency. As the heating frequency increases, the signal due to flaws below the silicon-solder interface (for example at the junction of the two halves) will attenuate more rapidly than those due to surface defects. Figure 4.22 shows a series of thermal images in the region near the hot bump in the center of the row. The signals at

Temperature at
40 kHz

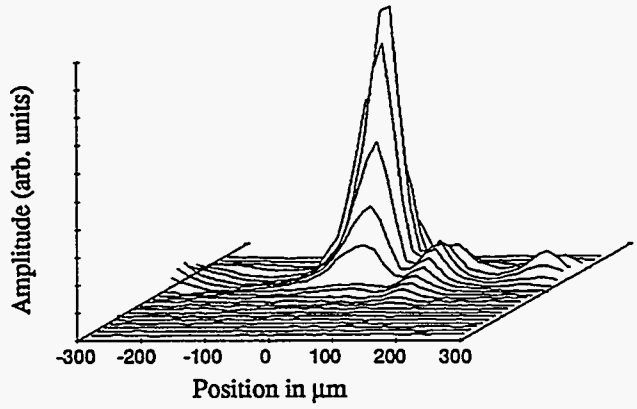

Temperature at
80 kHz

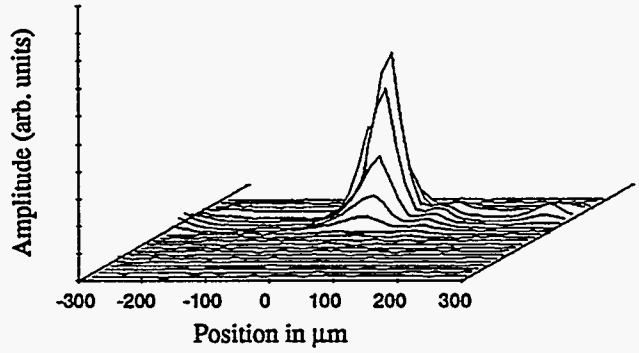

Temperature at
120 kHz

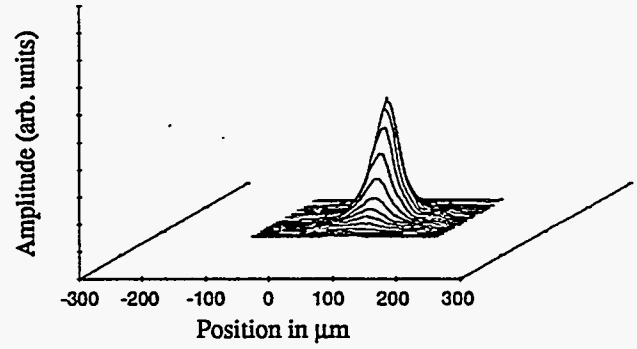

Figure 4.22 Sequence of thermal images of the region near the hot spot in the center of Figure 4.21. Defect at +100 µm is indicative of a subsurface flaw.

-300 μm, 0 μm, and +300 μm vary inversely with frequency, indicative of surface defects, while the flaw at +100 μm, decays more rapidly, indicating that it is located below the surface. At 80 kHz, Figure 4.22c, the bump is completely gone. These plots also demonstrate the high resolution of this photothermal technique; the probe spot size was on the order of a few microns.

We can obtain more quantitative information about the depth of the bond form the phase of the thermal signal, relative to that of the AC source. If the source of the heat is not coincident with the point of detection, there will be a phase lag associated with the thermal-wave propagation. From the theory of Chapter 2, we expect the phase to be proportional to the square root of frequency. For silicon we get

$$\phi = \frac{1}{13.3\,\mathrm{mm}/\sqrt{\omega_h}}\, d = 0.34\, d\sqrt{f} \text{ degrees} \tag{4.2}$$

where d is given in microns and f in kHz. Figure 4.23 shows an example where the phase lag implies that the flaw is 20 μm below the surface. Since the gap between the two substrates is 40 μm we can infer that the source of this flaw is a poor bond between the two solder bumps. Through a combination of amplitude and phase measurements, we were able to determine that the majority of the disbonds were at the solder-silicon interface.

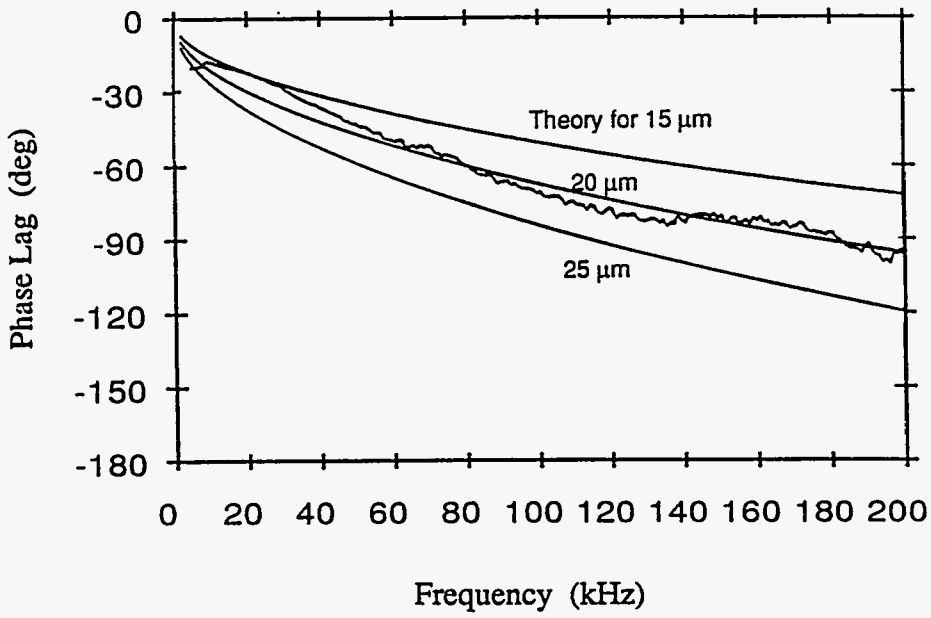

Figure 4.23 Thermal phase lag from a subsurface flaw. Solid lines are the theory for three different depths.

Chapter 4 References

1. J.T. Fanton, C.-H. Chou, B.T. Khuri-Yakub, and G.S. Kino,"Evaluation of solder bonds in a silicon flip-chip device," in *Review of Progress in Quantitative Nondestructive Evaluation* **7**, New York: Plenum Press, 1988

Chapter 5

Photothermal Measurements of High-T_c Superconductors

5.1 Introduction

Thermal conductivity is an important indicator of the scattering mechanisms in a material. In general, the thermal conductivity is determined by the number and type of particles that carry the heat, and the collisions which limit the flow. One of the major sources of collisions is electron-phonon scattering. Since the electron-phonon interaction also plays a critical role in the Bardeen, Cooper, and Schrieffer (BCS) theory of superconductivity, the study of the thermal conductivity of these materials could provide insight into the nature of the superconducting mechanisms.

In the previous chapters we demonstrated the usefulness of photothermal microscopy for measuring thermal properties on a small scale. This ability makes it an attractive technique for studying a new class of materials, the perovskite superconductors with high critical temperatures (T_c). Unlike the work in Chapter 4, however, our goal is not to locate flaws, but rather to study the inherent thermal conductivity of the material itself. By measuring the thermal conductivity as a function of temperature we hope to learn about the nature of the electron-phonon interactions, and hence about the nature of the superconductivity. Since the crystal structure and the electrical properties of these materials are extremely anisotropic, it is important to measure the behavior along each axis independently. However, high-quality, crack-free, single-crystal samples of these materials tend to be quite small (as small as 20 to 50 μm along some axes) and irregularly shaped, posing quite a challenge to the more standard, bulk techniques. The advantage of

the photothermal approach is that it can be used to measure the full, anisotropic conductivity of samples only a few microns on a side.

Another advantage of the photothermal approach is that the measurements are non-contacting and non-destructive. The only side-effects of the laser beams are a small perturbation of the temperature over a volume about 15 microns in radius, and a destruction of some of the superconducting pairs in the region of the absorption of the light (a volume about two microns across and one tenth of a micron deep). Since the temperature fluctuations extend far beyond the optical absorption depth, the thermal properties we measure will be predominantly those of the superconducting state. With such small perturbations, it is possible to conduct photothermal measurements in parallel with other measurements, such as electrical resistivity or magnetic susceptibility. It is even possible to create photothermal images of samples subjected to various currents or fields and thereby record the influence of these upon the thermal behavior. (As we will see below, the thermal conductivity undergoes abrupt changes at T_c.) The non-destructive nature of the measurement is also of great importance when studying rare samples.

Of course, the great benefit of having micron resolution comes at a price. A combination of poor thermal conductivity, poor reflectivity (about 10%), and the need for tightly focussed spots severely limit the acceptable probe power. Since we use a diode thermometer to determine the ambient temperature of the sample, we must keep the total temperature change at the surface (both AC *and* DC) less than a degree in order to be certain of the temperature at the test site. Therefore, we can only use a few microwatts of power to illuminate the sample. Nearly 90% of that is absorbed, and a further 80% to 90% is lost upon returning through the assortment of lenses and beam splitters. This leaves only a small fraction of a microwatt of optical power, with an intensity fluctuation of about one part in ten thousand, at the photodetector. Thus, our signals are extremely weak, even by photothermal standards, and we must average the signal for a second or more. Thermal imaging, consequently, will be very slow. There are a number of practical difficulties to

overcome as well, most of which involve the mechanics of creating a low-temperature, high-vacuum environment in which to conduct the measurements.

We begin this chapter with a brief description of the thermal measurements that have been made on polycrystalline superconductors, as well as some theoretical explanations for the observed behavior. We will be extending these measurements to the study of the anisotropic behavior of single-crystal specimens. To interpret our results, however, we first need to modify the theory of the periodic temperature profile about an optically heated spot to include anisotropy and finite probe beams, as discussed in Sections 5.3 and 5.4; these effects are important in a quantitative analysis. In Section 5.5 we present the results of room temperature measurements of the anisotropic thermal conductivity of Bi-Ca-Sr-Cu-O superconducting crystals. In Sections 5.6 and 5.7, we address the issues involved in taking the measurements down to low temperature. These issues include the high-vacuum environment and the importance of the non-linear terms in the diffusion equation. Finally, in Sections 5.8 and 5.9 we present our results on single-crystal Bi-Ca-Sr-Cu-O, and suggest future research in Section 5.10.

5.2 Motivation

Our interest in the applications of photothermal microscopy to the study of high-T_c superconductors began after unusual behavior of the low-temperature thermal conductivity was reported in the literature [1,2,3]. An example of an early measurement [1] is shown in Figure 5.1. The measured thermal conductivities of $La_{2-x}Sr_xCuO_4$ and $YBa_2Cu_3O_{7-\delta}$ are shown here as a function of temperature. The superconducting Y-Ba-Cu-O material ($\delta \cong 0$), in particular, shows a marked increase in κ below T_c. Subsequent examinations of semiconducting materials ($\delta \cong 1$) showed no such enhancement. Other experiments on polycrystalline Y-Ba-Cu-O and Bi-Ca-Sr-Cu-O materials have reproduced this behavior, but because of the difficulty of obtaining large, single-crystal specimens, there have been

but because of the difficulty of obtaining large, single-crystal specimens, there have been no reported measurements, to our knowledge, of the anisotropic values in a single-crystal material.

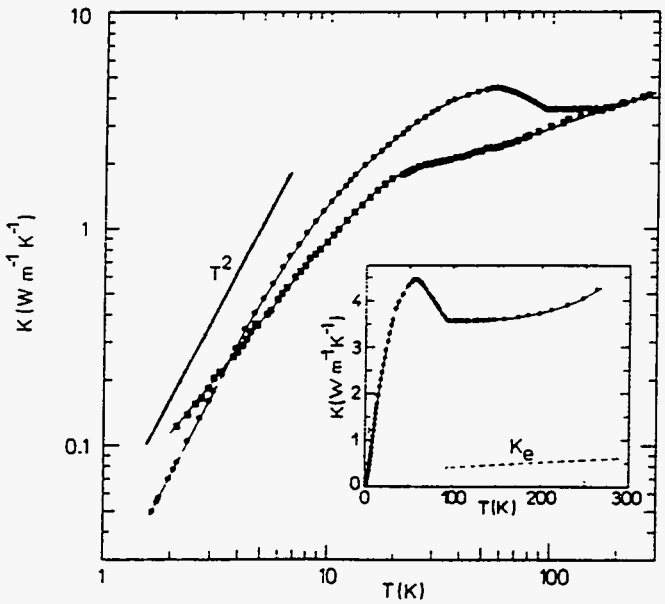

Figure 5.1 Thermal conductivity of $La_{2-x}Sr_xCuO_4$ (squares) and $YBa_2Cu_3O_{7-\delta}$ (circles) as a function of temperature (reprinted with permission from Ref. 1). The inset shows a linear plot for the Y-Ba-Cu-O material and an estimate of the electrical component of the thermal conductivity (dashed line).

The consensus is that this increase is due to an enhancement of the phonon mean free path as the electrical carriers condense into superconducting pairs below T_c. The freezing of the carriers can alter the thermal conductivity in two ways; the electrical component will decrease due to the reduction in the number of carriers, and the lattice component can increase due to the reduction in electron scattering. However, estimates of the electrical component, based on the Wiedemann-Franz law and electrical resistivity

measurements, place it at only about 10% of the total (dashed line in Figure 5.1). Thus the increase in the lattice component predominates. As the material is cooled further, the rapidly decreasing phonon population eventually limits the lattice conductivity.

This interpretation has received theoretical support from a recent analysis [4] applying the BCS theory to the electron-scattering-limited thermal conductivity, as originally put forth by Bardeen, Rickayzen, and Tewordt [5]. Originally developed to explain the drop below T_c in the thermal conductivity of classical superconductors (for which the heat is carried predominantly by electrons), this theory also explains the behavior of the lattice-dominated heat flow in the new superconductors. Figure 5.2, generated from the equations in Ref. 4, shows the predicted form of the lattice thermal conductivity, κ_g, as a function of temperature.

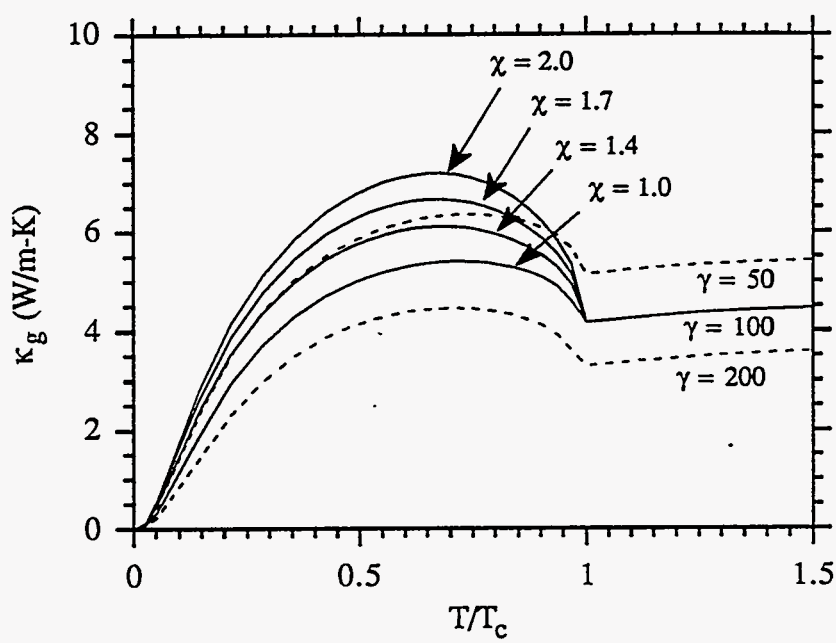

Figure 5.2 Lattice thermal conductivity, κ_g, vs $t = T/T_c$ from BRT theory. γ is proportional to the electron-phonon coupling and χ is the size of the gap relative to that of the BCS theory. (See Ref. 4 for formulae and definition of γ.)

It is worthwhile to examine further the origins of this curve. In their analysis, Tewordt et. al. include the possibility of many sources of scattering, including point defects, sheetlike faults, and grain boundaries, as well as the important electron-phonon interaction. The thermal conductivity, which is normally expressed as $\kappa = 1/3\ Cv\lambda$ where C is the heat capacity, v is the acoustic velocity and λ is the mean free path [6], is modified to include the various frequency dependences of the different scattering mechanisms. Since T_c is well below the Debye temperature, θ_D, they restrict their analysis to acoustic phonons. Using the Debye approximation for the heat capacity they get

$$\kappa_g = \left(\frac{T}{\theta_D}\right)^3 \int_0^{x_{max}} \frac{x^4 e^x}{(e^x - 1)^2} \times \frac{1}{\tau_p(x) + \tau_s(x) + \tau_b(x) + \tau_{el\text{-}ph}(x)}\, dx \qquad (5.1)$$

where $x \equiv \hbar\omega / k_B T$ and the τ's represent the scattering times of the various processes. At temperatures well below θ_D, x_{max} can be taken as infinity.

The first three scattering terms represent the non-electrical effects which affect the overall shape and magnitude of the curve. The effects of the superconducting transition are entirely contained in $\tau_{el\text{-}ph}$. In their analysis of the electron-phonon scattering, the authors show that there are two microscopic parameters that can be adjusted to duplicate observed behavior: the size of the gap relative to that of the BCS theory and the strength of the electron-phonon coupling constant. Thus, by examining the magnitude and the shape of the enhancement in κ_g it may be possible, within the confines of the BCS analogy, to deduce values for the electron-phonon coupling strength. For the Y-Ba-Cu-O data published in the literature, the authors estimate a coupling constant of about 0.5, within the weak-coupling range.

The above analysis assumed an isotropic material. In reality, the high-T_c superconductors are highly anisotropic, consisting of easily peeled layers. The layers are made up of the copper-oxide planes which are responsible for the superconductivity. The

direction normal to the planes, i.e. the c-axis, exhibits much poorer electrical resistivity at room temperature and fails to exhibit superconductivity at low temperatures. Hence the behavior of the thermal conductivity can be expected to differ substantially in these two directions. Although expressions for anisotropic media were not published, the authors state that c-axis data should show very little enhancement since the charge carriers in the ab-plane can absorb or emit only the component of phonon momentum that also lies in the ab-plane. At that time there was no experimental evidence to support this prediction since all published data were of polycrystalline ceramics, for the reasons stated earlier.

Thus we see the benefit of using a photothermal system to conduct anisotropic measurements of the thermal conductivity at low temperatures. However, we are also interested to determine if these effects can be utilized to form images of superconducting regions. If the change in the photothermal signal is strong enough, we have a possible means of observing the transition on a micron scale. Additionally, the non-contacting and flexible nature of the photothermal measurement would allow us to conduct other experiments in parallel with it. Thus we could test the influence of various fields or currents (perhaps even using electrical heating as the source), conduct magnetic susceptibility or resistivity measurements simultaneously, or perhaps even run the converse experiment to examine the effect of the local heating (or optical absorption) on the electrical flow.

5.3 Anisotropy

The thermal and acoustic theory of Chapter 2 was valid for isotropic materials. Since the crystal structure of the high-T_c superconductors is highly anisotropic, however, it is likely that both the temperature profiles and the displacements will be anisotropic. Fortunately, we need only consider the equations for surface temperature since we will be working exclusively with the dR/dT method in this chapter. A completely general

extension of the acoustic theory would be formidable since both the excitation (temperature profile) and the material response (expansion coefficients) are anisotropic. (However, the assumptions that led to the simplified expansion-only formula for the displacement in Chapter 2, (2.36), could still be applied to give an expression good to within a scale factor.)

We begin with Fourier's law for heat conduction in its most general form,

$$J_i = -\sum_{j=1}^{3} \kappa_{ij} \frac{\partial\theta}{\partial x_j} . \tag{5.2}$$

The thermal conductivity is a second rank tensor for any arbitrary coordinate system. Since it is symmetric, however, we can find a coordinate system where the off-diagonal terms are zero. In this frame we have

$$\mathbf{J} = -\kappa_x \frac{\partial\theta}{\partial x}\hat{\mathbf{x}} - \kappa_y \frac{\partial\theta}{\partial y}\hat{\mathbf{y}} - \kappa_z \frac{\partial\theta}{\partial z}\hat{\mathbf{z}} . \tag{5.3}$$

From symmetry arguments, it is clear that this coordinate system corresponds to the crystal axes.

To obtain the diffusion equation, we also need the equation of continuity. Since the heat capacity is a scalar quantity, this equation is unchanged,

$$\nabla \bullet \mathbf{J} = -C\frac{\partial\theta}{\partial t} . \tag{5.4}$$

Taking the divergence of (5.3) and using (5.4) to eliminate **J**, we get

$$\kappa_x \frac{\partial^2\theta}{\partial x^2} + \kappa_y \frac{\partial^2\theta}{\partial y^2} + \kappa_z \frac{\partial^2\theta}{\partial z^2} = C\frac{\partial\theta}{\partial t} . \tag{5.5}$$

Assume that the z-direction is normal to the surface of our semi-infinite sample. We can recover the isotropic form of the diffusion equation by re-scaling the axial dimensions to

$$x' \equiv \sqrt{\frac{\kappa_z}{\kappa_x}}\, x, \quad y' \equiv \sqrt{\frac{\kappa_z}{\kappa_y}}\, y, \quad z' \equiv z \tag{5.6}$$

giving us

$$\frac{\partial^2\theta}{\partial x'^2} + \frac{\partial^2\theta}{\partial y'^2} + \frac{\partial^2\theta}{\partial z'^2} = \frac{C}{\kappa_z}\frac{\partial\theta}{\partial t}, \tag{5.7}$$

or

$$\nabla'^2\theta = \frac{1}{D_z}\frac{\partial\theta}{\partial t}. \tag{5.8}$$

The completion of the boundary-value problem is just the Cartesian analogue of Chapter 2 with one important distinction - the excitation in the primed coordinate system is no longer circularly symmetric. Proceeding, we assume a solution of the form

$$\theta(x',y',z') = \int_{-\infty}^{\infty} A(s,p)\, e^{-j2\pi x's}\, e^{-j2\pi y'p}\, e^{-\sqrt{(2\pi s)^2+(2\pi p)^2+k_t^2}\, z}\, ds\,dp \tag{5.9}$$

with k_t being defined as the thermal propagation constant in the z-direction, $k_t^2 = j\omega/D_z$. We find A(s,p) by matching the thermal boundary conditions at z=0, as in Chapter 2. The result is

$$A(s,p) = \frac{H(-s,-p)}{\kappa_z\sqrt{k_t^2+(2\pi s)^2+(2\pi p)^2}} \tag{5.10}$$

where H is the 2-dimensional Fourier transform of the heating profile in the primed system. As in Chapter 2, it is convenient to assume a Gaussian profile for the heating beam since it has a well behaved transform and is a very good approximation of the actual profile. Let

$$h(x,y) = \frac{P_h}{\pi r_h^2} e^{-\frac{(x^2+y^2)}{r_h^2}} . \tag{5.11}$$

In the primed system this is

$$h(x',y') = \frac{P_h}{\pi r_h^2} \left[e^{-\frac{k_x}{k_y}\frac{x'^2}{r_h^2}} \times e^{-\frac{k_y}{k_z}\frac{y'^2}{r_h^2}} \right] \tag{5.12}$$

which transforms to

$$H(s,p) = \frac{P_h \kappa_z}{\sqrt{\kappa_x \kappa_y}} e^{-(\pi\sqrt{\kappa_z/\kappa_x}\, r_h s)^2} e^{-(\pi\sqrt{\kappa_z/\kappa_y}\, r_h p)^2} . \tag{5.13}$$

Thus the anisotropic surface-temperature profile is given by

$$\theta_o(x',y') = \frac{P_h \kappa_z}{\sqrt{\kappa_x \kappa_y}} \int_{-\infty}^{\infty} \frac{e^{-(\pi r_{hx} s)^2} e^{-(\pi r_{hy} p)^2}}{\sqrt{k_t^2 + (2\pi s)^2 + (2\pi p)^2}} e^{-j2\pi x's} e^{-j2\pi y'p} \, ds\,dp \tag{5.14}$$

where $r_{hx} \equiv \sqrt{\kappa_z/\kappa_x}\; r_h$ and $r_{hy} \equiv \sqrt{\kappa_z/\kappa_y}\; r_h$. By recasting our equation in the new scaled coordinate system, we have recovered a form similar to that for an isotropic material heated by an elliptical Gaussian beam.

Because (5.14) is similar to an isotropic formula, we can draw on the conclusions of Chapter 2 to predict the behavior of (5.14). For example, we showed in Chapter 2 that the shape and size of the heating beam are irrelevant in the low-frequency behavior at distances far from the origin. Therefore, in the primed system the contour lines of phase and amplitude should approach circles at large radii. Thus, in the real coordinate system

we expect the anisotropy in the phase and amplitude to be greatest at large radii (and low frequencies). Furthermore, the slope of the phase along the two axes should approach the ratio of the scaling constants, $\sqrt{\kappa_x/\kappa_y}$. In regions close to the heat source, the temperature profile should follow that of the heating beam. Therefore, in the real coordinate system we should see circular contour lines near the origin, regardless of the anisotropy.

Figures 5.3 a-f show the calculated amplitude and phase contours for low-frequency (ω/D_x, ω/D_y << spot size), mid-frequency (ω/D_x < spot size < ω/D_y), and high-frequency (ω/D_x, ω/D_y >> spot size) cases. An anisotropy of 6 to 1 and a Gaussian radius of 1.5 μm were assumed. As expected, the anisotropy shows up most clearly at low frequencies and large radii. Hence, this is the regime in which we will conduct our experiments. At high frequencies or small radii the contour lines are circular.

An interesting artifact that occurs at high frequencies is that ellipticity of the phase contours reverses, with the phase lag being smaller in the direction of *poor* conductivity. This reversal may seem counter-intuitive, but since it occurs entirely within the radius of the heating spot, the phase does not represent a propagation delay in the same sense as above. We see a smaller lag along the y-axis because regions separated by Δy are isolated from each other due to the severe exponential decay in that direction. Thus, strips of Δy track the heating beam closely and suffer little phase lag (albeit they have very small amplitudes). Heat flow along the x-axis, however, is attenuated much less. Thus, regions from farther away contribute to the overall temperature, both increasing the amplitude and contributing to an overall greater phase lag. This reversal is quite subtle and would be very difficult to detect experimentally since it all happens within the radius of the pump beam. To detect such an effect, we would need to use a probe with much finer resolution than the pump. Furthermore, small imperfections in the circular symmetry of the pump beam would mask the reversal.

An important point to consider about the low frequency regime, where we will be operating experimentally, is that the temperature decays *faster* than 1/r in the direction of

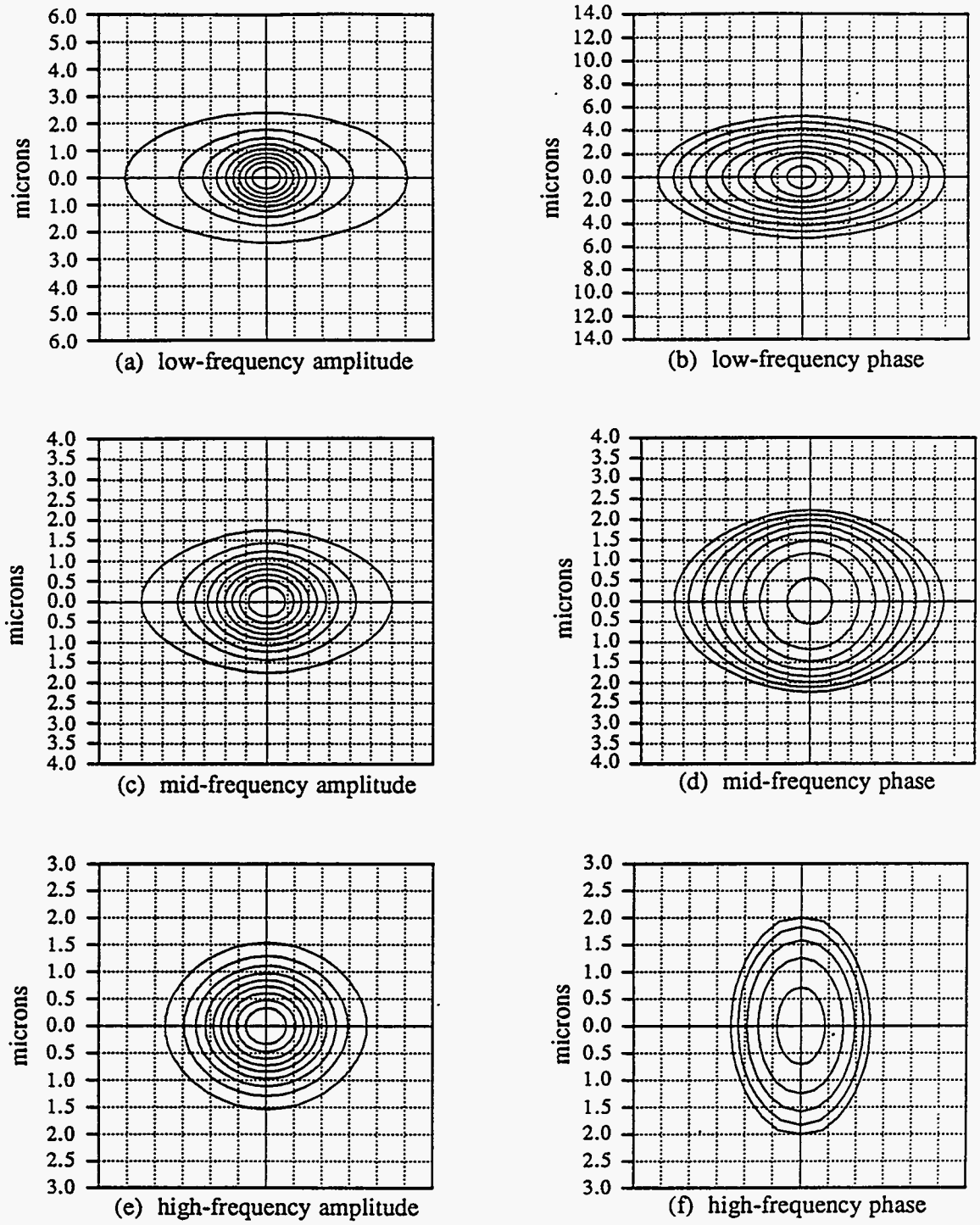

Figure 5.3 Theoretical amplitude and phase contours of the temperature profile in an anisotropic medium. The conductivity in the x-direction is assumed to be six times that in the y-direction. The source is a Gaussian beam with a radius of 1.5 μm.

poor conductivity because the heat preferentially flows in the perpendicular direction. When measuring along this axis we will have to place the heating and probe beams very close together. They must be closer, in fact, than they would if the conductivity were equally poor in *all* directions. At low frequencies, the practical limit to the separation is determined not by the actual values of the thermal constants, but by the anisotropy. This is demonstrated explicitly in Figure 5.4 where the temperature profiles along both the high- and low-conductivity axes are shown, along with the profile for an isotropic material.

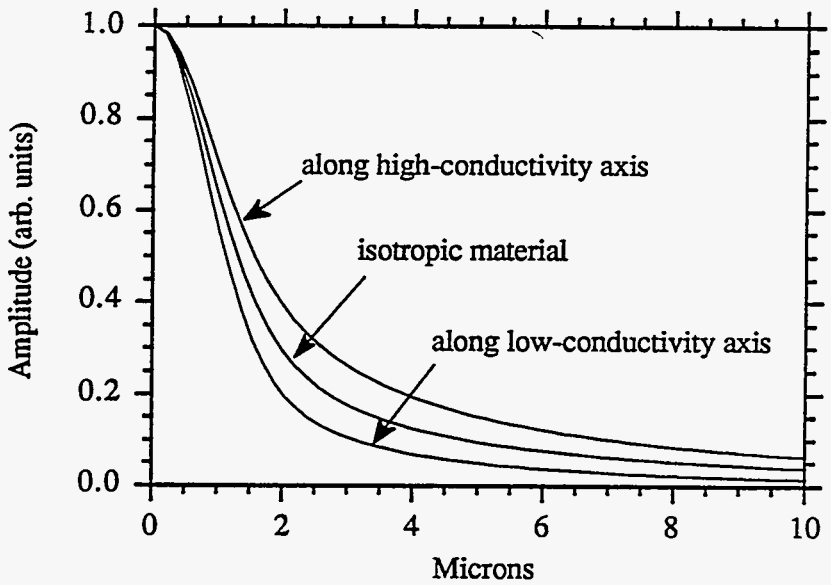

Figure 5.4 Radial dependence of the temperature profile along both axes of an anisotropic material (first and third curves) and in an isotropic material (center curve).

5.4 Spot-Size Effects

Since the area of the probe beam is often comparable to that of the source, we cannot assume that we are measuring the temperature at a fixed point. Instead, our signal represents the *average* change in reflectivity over the area illuminated by the probe beam. Thus we need to calculate a weighted average of $\theta_o(x,y)$. Assuming that the probe spot is Gaussian with radius r_p, our dR/dT signal will be

$$i_{sig} = \eta \frac{dR}{dT} \frac{P_h P_p}{\pi r_p^2} \int_{-\infty}^{\infty} \theta_o(x,y)\, e^{-\frac{(x-x_o)^2}{r_p^2}} e^{-\frac{(y-y_o)^2}{r_p^2}} dx\, dy \tag{5.15}$$

where the center of the probe is located at (x_o,y_o), and η is the photodetector conversion efficiency. While an expression for i_{sig} can be found by substituting $\theta_o(x,y)$ from (5.14) and grinding out the integration, the simple way to solve for i_{sig} is to note that (5.15) is a convolution integral. Since the convolution of two Gaussians is a third Gaussian with radius equal to the sum of the original radii, we can write the solution directly. Thus our final expression for the photothermal signal generated by a Gaussian heating beam of power P_h and radius r_h and detected with a probe of power P_p and radius r_p is

$$i_{sig} = \eta \frac{dR}{dT} \frac{P_h P_p}{\sqrt{\kappa_x \kappa_y}} \int_{-\infty}^{\infty} \frac{e^{-(\pi r_{mx} s)^2} e^{-(\pi r_{my} p)^2}}{\sqrt{k_t^2 + (2\pi s)^2 + (2\pi p)^2}}\, e^{-j2\pi x_o' s}\, e^{-j2\pi y_o' p}\, ds\, dp \tag{5.16}$$

where

$$r_{mx} \equiv \sqrt{\frac{\kappa_z}{\kappa_x}} \sqrt{r_h^2 + r_p^2}$$

$$r_{my} \equiv \sqrt{\frac{\kappa_z}{\kappa_y}} \sqrt{r_h^2 + r_p^2}$$

$$x_o' \equiv \sqrt{\frac{\kappa_z}{\kappa_x}}\, x_o, \qquad y_o' \equiv \sqrt{\frac{\kappa_z}{\kappa_x}}\, y_o$$

$$k_z^2 = j\,\frac{\omega C}{\kappa_z}$$

We use this expression in all of our data reduction. In practice, the expressions are evaluated numerically using the FFT algorithms outlined in the appendix.

We see that the probe size increases the apparent heating spot by 50% when, as is the usual case, $r_h = r_p$. This effect, combined with the need for close proximity in the direction of poor conductivity, causes the phase data to depart significantly from the simple $f^{1/2}$ behavior of point source measurements. Thus it is essential to include these effects in a quantitative analysis.

5.5 Room-Temperature Results

Now that we have a more complete theoretical model, we are ready to undertake a quantitative analysis of the anisotropic thermal conductivity. We begin with a rigorous study of the thermal conductivity at room temperature. We get a strong indication that the thermal properties may be highly anisotropic from simple photothermal amplitude measurements (dR/dT) of polycrystalline Y-B-Cu-O films. Figures 5.5a and 5.5b show

the optical reflectivity and the photothermal response of a 40 μm-square area. The thermal image shows far greater fluctuations in intensity, indicating that the orientation of the individual crystallites plays a major role in the amplitude of the photothermal signal. With an amplitude image alone, however, it is impossible to determine whether these fluctuations are due to changes in κ, or to changes in dR/dT. To separate these two effects we need to use an amplitude-insensitive measurement. Thus, for quantitative analysis we work with *phase*.

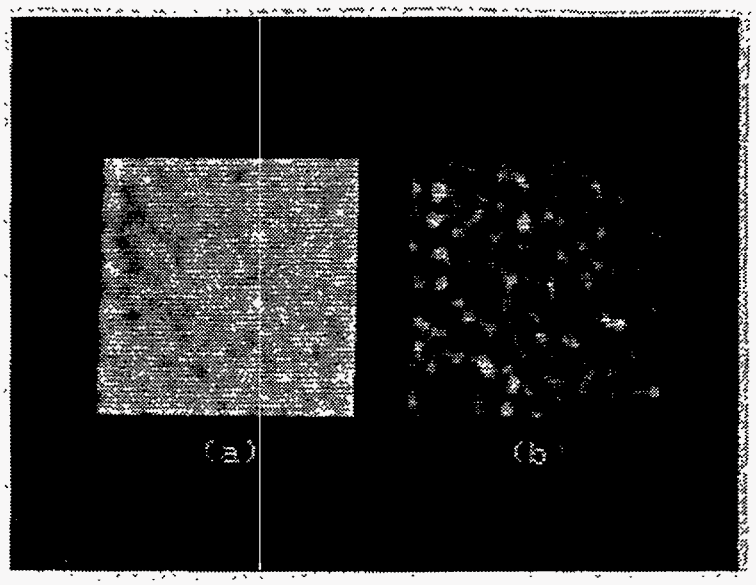

Figure 5.5 Optical image (left), made by recording the DC component of the reflected probe beam, and photothermal amplitude image (right), using dR/dT method, of a thin polycrystalline film of Y-Ba-Cu-O.

Our phase measurement technique is sketched in Figure 5.6. We separate the heating and probe beams by a fixed amount and measure the propagation delay as a function of frequency. The phase lag is roughly

$$\phi_{thermal} \cong \sqrt{\frac{\omega}{2D}}\,\Delta x \tag{5.17}$$

where D is the thermal diffusivity in the direction of the separation. (Of course, the full formula in Section 5.4 is actually used to reduce the data.) The only unknown parameter in this expression is D, thus the phase delay directly specifies the thermal diffusivity.

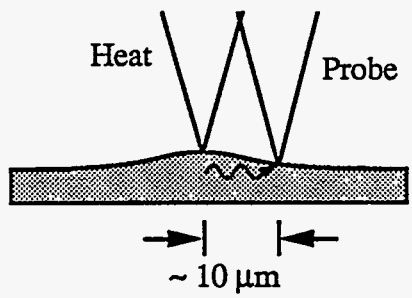

Figure 5.6 Schematic of the phase measurement.

The ideal spot separation, Δx, depends on the spot size. We prefer to use large separations so that the size and shape of the spots is irrelevant. At very large separations, however, we sacrifice too much signal to 1/r decay. As we saw in Section 5.2, the decay is especially severe in the direction of poor conductivity. In practice, we usually place the probe at about the 10%-amplitude contour line. For high-T_c superconductors, this corresponds to a separation of about five or six spot widths (10 to 15 μm) in the high-conductivity direction, and only about two or three in the poor direction.

To test our theory and methods, we measured the thermal anisotropy of crystalline quartz since it has already been well characterized by bulk methods. In order to confine the heating to the surface of the crystal, we deposited a 50 Å layer of titanium on the ac-face. Titanium has a relatively poor thermal conductivity for a metal (22 W/m-K compared to, for example, 240 W/mK for aluminum) so it does not act as a thermal short circuit. For this

sample, the thermal expansion of the quartz gave rise to larger signals than the dR/dT of the titanium. Therefore, we used the slope method to infer the temperature.

The phase lag we measured, shown in Figure 5.7, closely followed straight lines. The phase data in these plots represent the true thermal phase lag across a spot separation of 9 μm. Extraneous phase effects, such as photodetector and amplifier lags, and acoustic propagation delay in the Bragg cell, have been removed by subtracting a calibration curve, generated by turning off the probe, removing the optical filters, and measuring the phase of the reflected heating beam. The spot separation was determined by scanning the two beams across a sharp edge or step in reflectivity (such as a patterned silicon wafer) and recording the reflected intensities as a function of position. There is about a 0.5 μm uncertainty in the separation due to the size of the spots and jitter in the scanning actuators.

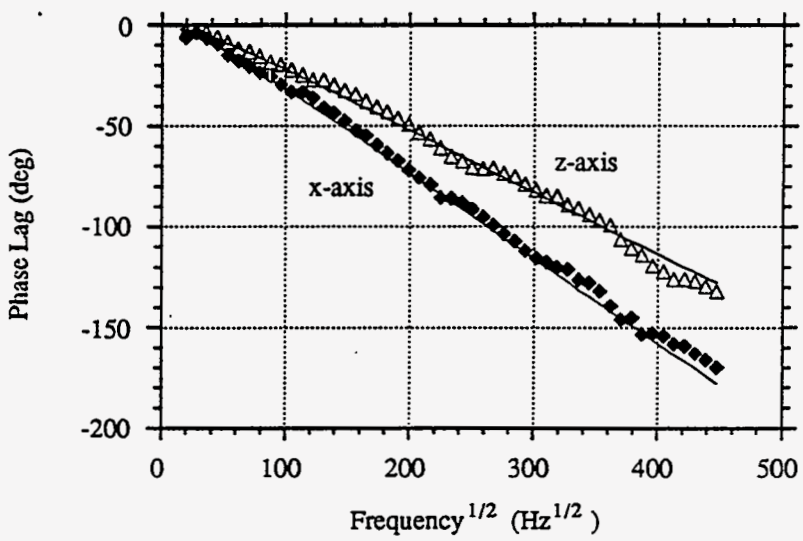

Figure 5.7 Measured thermal phase lag along both axes of single-crystal quartz. Solid lines are the theory using the published values for κ and C [7].

Also shown in Figure 5.7 are the theoretical phase plots using values of κ and C from the literature [7]. We see that our measurements agree within a few percent, thereby confirming our methods.

(Incidentally, many photodiodes exhibit a subtle behavior that is not widely appreciated, but profoundly affects the calibration. The phase lag, or speed, of these devices is not necessarily constant over the entire active area; regions near the edge tend to be slower. One must avoid the temptation to bypass the optics and simply shine the heating beam directly into the detector; the calibration will be in error unless the beam is actually focussed to the center of the device. These errors are severe enough to affect the interpretation of the data.)

Turning to the high-T_c superconductors, we studied two types of bismuth samples: single-crystal chips grown in a strong temperature gradient to align the crystal [8], and single-crystal fibers grown by the laser-heated pedestal growth method [9]. The chips are similar to mica in that they tend to form large thin sheets of material in the ab-directions. The fibers were grown such that the ab-planes ran along the length of the fiber. To examine the c-axis in either sample, the crystals were embedded in epoxy and mechanically polished to optical smoothness. Figure 5.8 shows photomicrographs of the ac-planes in both types of sample. (Thermal scans of the fiber were also presented in Chapter 4.) As is evident in the photos, crack-free regions are of the order 20 to 50 μm wide (although as we showed in Figure 4.6, not all cracks are visible optically).

The results of a typical frequency sweep on the ab-face of a single-crystal chip are shown in Figure 5.9a. The spot separation was 11 μm and the temperature was inferred by the dR/dT method. In these materials this effect is fairly strong, on the order of 10^{-4} /K, and gives rise to signals much larger than those obtained by the slope method. The solid line is a theoretical fit assuming a diffusivity of 2.0 mm^2/s. The measurements were repeated on the ac-face with the spot separation oriented along the edge of the Cu-O planes. The results, Figure 5.9b, agree with those from the ab-face as expected. (The data is

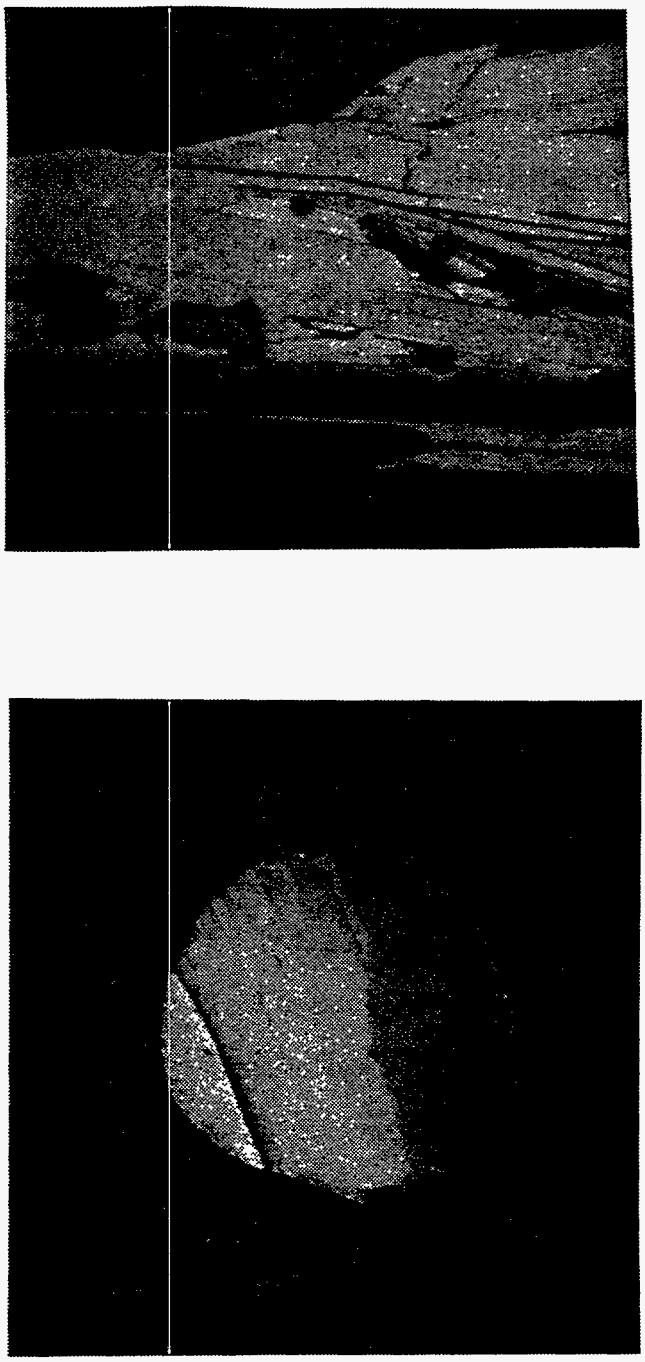

Figure 5.8 Photomicrographs of the ac-plane of a typical single-crystal Bi-Sr-Ca-Cu-O chip (top) and a single-crystal fiber (bottom).

somewhat smoother because higher laser powers were used and the separation was slightly smaller.)

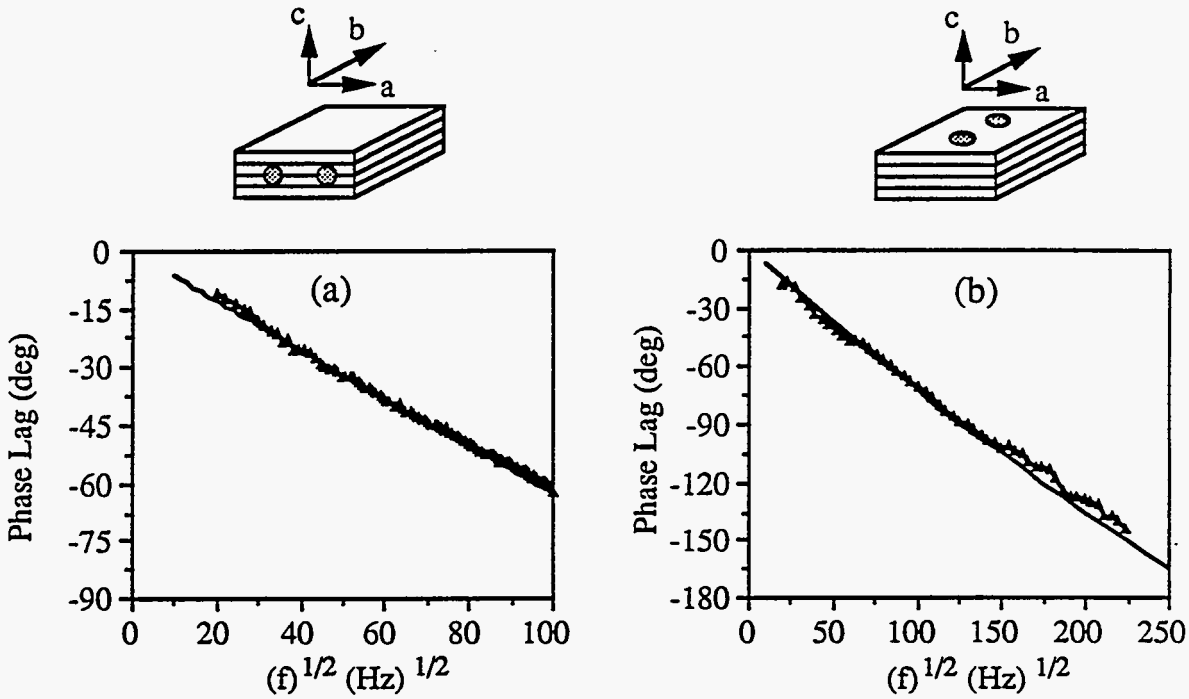

Figure 5.9 Room-temperature thermal diffusivity along the Cu-O planes of single-crystal Bi-Sr-Ca-Cu-O. Figure 5.9a is data from the ab-face; Figure 5.9b is from the ac-face.

It should be noted that for the data taken on the ac-face, the probe beam was polarized in the direction of the ab-planes. When the polarization was oriented along the c-axis, the magnitude of the signal dropped by a factor of eight. Hence, like so many other properties of these crystals, the dR/dT effect is extremely anisotropic. This is in contrast to the simple reflectivity which, at optical frequencies, is fairly uniform [10]. Thus the variations in the thermal image of the polycrystalline sample, Figure 5.5, are due as much to the random orientations of the exposed crystallites as they are to thermal changes. We

expect that these types of variations could be reduced by using a circularly-polarized probe beam.

We determined the thermal anisotropy of single-crystal Bi-Sr-Ca-Cu-O by rotating the ac-plane of the fiber by 90° and conducting measurements along the c-axis. The results, shown in Figure 5.10, fit the theory for a diffusivity of 0.3 mm^2/s. Thus we measure a large anisotropy of about 6 to 1. Note the strong upward curvature of the data due to the finite size of the probe beam. As indicated above, we needed to use a very small spot separation, about 4.5 μm, because of the large anisotropy. Hence the phase departs significantly from the point-source behavior. Physically, the curvature sets in when the frequency reaches the point at which the thermal wave is significantly attenuated across the width of the optical spots. Above this frequency, contributions from the outer regions of the spots diminish, and the apparent spot separation decreases.

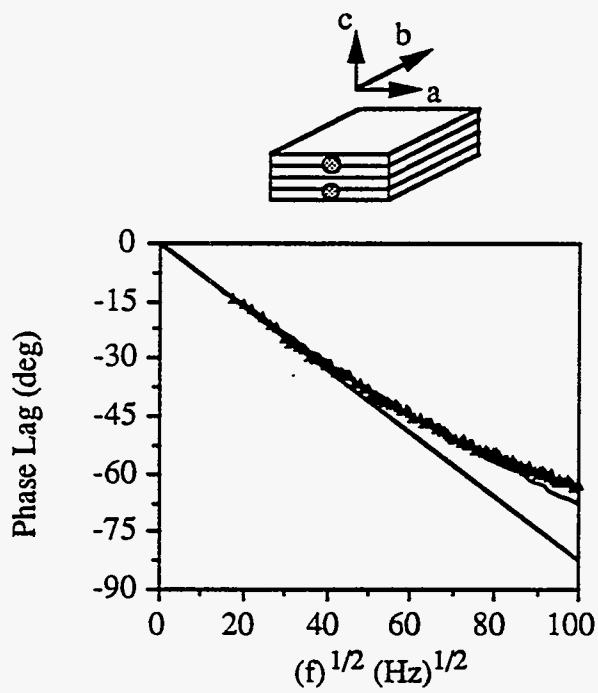

Figure 5.10 Room-temperature thermal diffusivity across the Cu-O planes of single-crystal Bi-Sr-Ca-Cu-O. Solid lines are the point-source theory (straight line) and the full three-dimensional theory (curved line).

Measurements along the c-axis of the single-crystal chips exhibited similar diffusivities. The variation from measurement to measurement was about 30%, due mostly to uncertainties in the spot separation. For a 4.5 μm separation, a 0.5 μm uncertainty gives rise to a 10% error in the separation, Δx, or a 20% error in the diffusivity since $D \sim \Delta x^2$. We used larger separations for the ab-plane measurements, which consequently were more consistent.

Figure 5.11 shows an alternative measurement of the anisotropy that we conducted to further verify our values. In this measurement we kept the frequency fixed and measured the phase lag as a function of the crystal orientation. The results agree well with the anisotropic model using the axial diffusivity values calculated above.

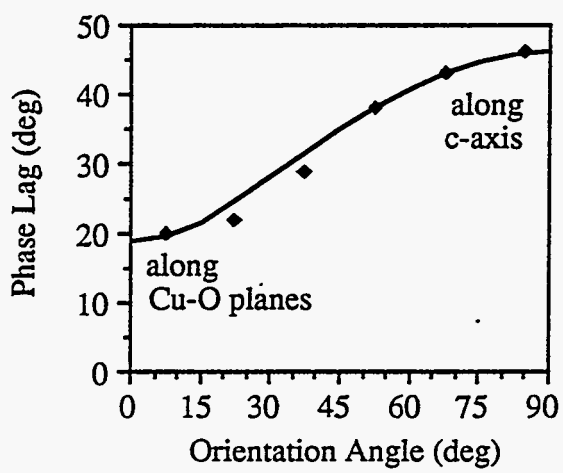

Figure 5.11 Phase lag in the ac-plane as a function of the crystal orientation. Solid line is from 3-D theory using the axial values of D determined above.

5.6 Non-Linear Effects at Low Temperatures

The next step in the study of high-T_c superconductors, and indeed the driving motivation, is to observe the photothermal behavior at the transition to the superconducting state. Before we proceed, however, we need to reconsider some of the assumptions of our photothermal theory. So far, we have assumed that the thermal conductivity (or diffusivity) and the heat capacity are independent of temperature. Below the Debye temperature (~ 180K), however, the heat capacity drops rapidly. The thermal conductivity of the ceramic materials was shown to be strongly temperature dependent as well. We need to determine the importance of this behavior in our measurement.

A general treatment of thermal diffusion at low temperatures leads to a non-linear differential equation for the temperature profile. However, since we work with very small temperature fluctuations, the non-linear terms can be ignored. We derive here the general form of the diffusion equation and examine the limits of the linearized theory.

As in Section 5.2, we begin with Fourier's law and the continuity equation, this time explicitly showing the temperature dependence of C and κ. We denote the total temperature by T, reserving θ for the AC component later;

$$\mathbf{J} = -\kappa(T)\,\nabla T \tag{5.18}$$

$$\nabla \bullet \mathbf{J} = -C(T)\frac{\partial T}{\partial t} \tag{5.19}$$

Notice that κ and C are *not* included in the differentiation. The reason κ is not included is obvious when one considers the case of an inhomogeneous material at constant temperature; terms like $\nabla\kappa T$ would lead to heat flow between two different materials at the same temperature. The time derivative in the continuity equation does not include C since the heat capacity is defined as the differential dependence of the internal energy upon the

temperature, $C \equiv \partial U/\partial T$. A change in C does not, by itself, involve a release (or storage) of energy.

In general, we should also consider that there can be more than one type of carrier involved in the transport of heat. The thermal conductivity actually consists of both a lattice component and an electrical component,

$$\kappa \equiv D_e C_e + D_p C_p . \tag{5.20}$$

Likewise, the heat capacity has, in general, two components

$$C \equiv C_e + C_p . \tag{5.21}$$

However, even in metals the lattice term is usually much greater at temperatures above a few Kelvin [11].

We proceed with the derivation of the diffusion equation in the usual way by taking the divergence of the heat flow to get

$$\nabla \bullet \mathbf{J} = \nabla \kappa \bullet \nabla T + \kappa \nabla^2 T . \tag{5.22}$$

We can write

$$\nabla \kappa = \frac{\partial \kappa}{\partial T} \nabla T , \tag{5.23}$$

and thereby simplify (5.22), leaving a non-linear diffusion equation of the form

$$\nabla^2 T + \left(\frac{1}{\kappa(T)} \frac{\partial \kappa(T)}{\partial T} \right) (\nabla T)^2 = \frac{C(T)}{\kappa(T)} \frac{\partial T}{\partial t} . \tag{5.24}$$

The new term involving $(\nabla T)^2$ enormously complicates the solution. In general, the heat flow will be a function of the heat intensity as well as κ and C, requiring that we have an accurate knowledge of not only the material parameters, but the laser powers and the

reflectivities as well. Over most of the temperature range we are spared these problems, however, because we actually work with very small perturbations in T:

$$T \equiv T_o + \theta \tag{5.25}$$

where θ is the component due to the laser heating (about 1° C).

The thermal constants, κ and C, can be expanded in Taylor series of the form

$$C(T) = C(T_o) + \left.\frac{\partial C}{\partial T}\right|_{T_o} \theta . \tag{5.26}$$

For T_o between about 30 K and room temperature, the first order terms are negligible due to the small magnitude of θ. For example, at very low temperatures we might expect C to be proportional to T^3 for which case the derivative term is negligible as long as $3\theta << T_o$. (One possible exception to the small-derivative approximation is the discontinuity of the electrical component of the heat capacity at T_c due to the onset of pair formation. However, this discontinuity is small and our differentiation is averaged over a degree. Therefore the contribution of the discontinuity should be minor and, if detected at all, should only appear in a one Kelvin range about T_c.) Similar arguments hold for the magnitude of the non-linear term in (5.25). With small perturbations, the squared non-linear term is relatively unimportant.

Hence the linear diffusion equation is still a valid model of the heat flow for our particular circumstances. It should also be noted that the critical quantity we will be measuring is

$$\frac{C}{\kappa} = \frac{C_e + C_p}{C_e D_e + C_p D_p} \tag{5.27}$$

from the right-hand side of (5.24). In the next few sections we refer to the inverse of this quantity,

$$D = \frac{C_e D_e + C_p D_p}{C_e + C_p} \cong \frac{C_e}{C_p} D_e + D_p , \tag{5.28}$$

as the thermal diffusivity even though it is actually a weighted average of the electrical and lattice components. The ambiguity is removed when we convert this quantity to the total thermal conductivity by multiplying by C_p.

To test the limits of the linearized theory, the non-linear diffusion equation was examined numerically (using a finite differencing scheme) for a simple example that assumed an isotropic medium and a spherical heat source. It was found that the non-linear term has little effect until it reaches a large fraction of the Laplacian term, especially when examining the temperature far form the source. Physically, the non-linear term tends to give rise to higher harmonics which die out even faster than the fundamental because of the dispersive nature of the exponential decay.

5.7 The Low-Temperature Environment

As briefly noted in the introduction, there are a number of practical issues to address when taking this experiment to low temperatures. Of primary concern are the formation of ice on the sample and the measurement of the ambient temperature. This section briefly describes our approach to these and other problems.

The severity of the ice accumulation can be appreciated by considering some simple gas kinetics. At pressures where the mean free path of the gas molecules exceeds the chamber dimensions (i.e., below about 10^{-4} Torr), the average number of collisions with the walls per area is [12]

$$J = \frac{1}{4} n \langle v \rangle \tag{5.29}$$

where n is the number density and <v> is the average velocity. After a few hours of pumping, the majority of the gas in the chamber is water vapor that has outgassed from the walls of the chamber [12]. Assuming that every collision with a cold surface results in adhesion, ice will accumulate at a maximum rate of

$$\frac{dx_{ice}}{dt} = \frac{JM}{\rho} \cong 36\frac{P}{R_o\rho}\sqrt{\frac{M}{T}} \quad \text{in MKS} \tag{5.30}$$

where P is the pressure, M is the molecular weight, ρ is the density, and R_o is the universal gas constant. For water vapor at 100 K, we get an accumulation rate of

$$\frac{dx_{ice}}{dt} = 1.0 \times 10^6 \, P \; \mu m/hr \tag{5.31}$$

where P is in Torr. Clearly, for a measurement that takes place over a range of a few microns we cannot tolerate buildup of much more than about a micron of ice. Since the experiment takes about 2 or 3 hours to complete, we need to obtain pressures of slightly less than 10^{-6} Torr, a very difficult task for a system that cannot be baked out before each run (to avoid damaging the samples).

We were able to achieve the necessary vacuum using the system shown in Figure 5.12. The heart of the system is an R. G. Hansen and Associates liquid-helium-cooled cryostat which we needed to modify considerably to reach 10^{-6} Torr. The standard vacuum shroud was replaced by a simple cylinder to reduce the surface area and the number of o-rings, and all brass and aluminum parts were replaced by stainless steel. An 8 liter/sec Varian ion pump, connected to the system by a short length of 1" diameter stainless-steel tubing, provided the high vacuum. A rough vacuum was achieved with a separate sorption pump. Both pumps are ideally suited for our needs because they are vibration free and introduce no pumping oils into the environment. With this system we were able to obtain vacuums of slightly less than 2×10^{-6} Torr at room temperature after about 24 hours of pumping. At room temperature, the pumping rate is limited by the conductance of the

relatively narrow exhaust port (not the pumps themselves), however, at low temperatures the cool interior walls of the chamber begin to act as cryopumps and the pressure drops to about 5×10^{-7} Torr.

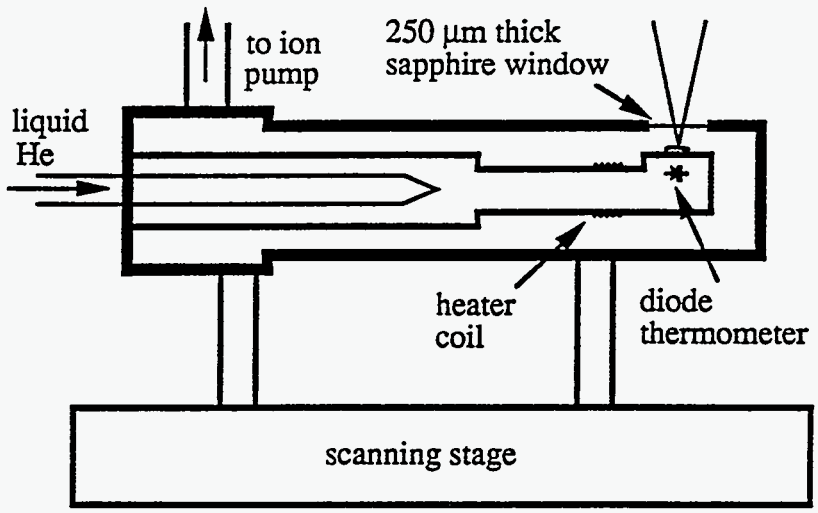

Figure 5.12 Schematic of the high-vacuum cryostat.

Optical access to the sample was provided by a thin window in the vacuum shroud. The issue when designing the window is how to minimize the distortion and maintain the highest possible resolution (cover-slip-corrected microscope objectives account for this distortion but are infeasible because of their short working distances). We chose sapphire for the window material because of its high mechanical strength; a half inch diameter pane only 250 μm thick withholds the vacuum and enables us to achieve diffraction-limited spot sizes using lenses with NA's as high as 0.3. At higher NA's, the distortion of the window outpaces the improvement in the diffraction limit.

Finally, we need to consider how to measure and control the bulk temperature of the sample. The system is cooled by flowing liquid helium through the inside of the cold finger. Temperature control is provided by a silicon diode sensor and a heater coil controlled by a Scientific Instruments Series 5500 automatic controller. To minimize the

temperature difference between the sample and the sensor, we imbedded the diode in the copper sample mount directly below the sample. We verified the accuracy of the background temperature measurement in three ways: by comparing two diodes placed at different locations on the cold finger, by comparing the diode readings with those of a platinum resistance thermometer placed where the sample would normally sit, and by measuring the temperature of a liquid nitrogen bath. These calibrations confirmed that, down to about 30 K, the temperature reading was within a degree of the actual surface temperature of the mount.

The sample was fixed to the sample mount with a thin layer of thermal grease. Even though we verified that the surface temperature of the mount is measured accurately, there is the possibility that thermal radiation from the warm walls of the vacuum shroud might heat the sample excessively. However, a quick calculation removes our concern; the radiative flux impinging upon the top of the sample is

$$J = \sigma T^4 = 460 \text{ W/m}^2 \tag{5.32}$$

Assuming a worst-case thermal conductivity of only 0.5 W/mK, we find that there will be about a 1° drop for every millimeter of material. The majority of the samples are far thinner.

There is one additional problem with the present system that affects our data. As the cryostat is cooled over the 300° range of the experiment the cold finger contracts considerably, causing the sample to drift both laterally and vertically. As a result, the optics must be frequently adjusted to keep the sample in focus. Since the integration time of the signal is long, this disruption creates a small, but noticeable, amount of ripple in the data. An automatic focus is currently being added to the microscope to minimize this problem.

5.8 Low-Temperature Thermal Conductivity of Single-Crystal Bi-Sr-Ca-Cu-O Materials

We begin this section with our results on the Cu-O planes of an 88 K-phase $Bi_2Sr_2CaCu_2O_x$ chip. Figure 5.13 shows the thermal phase lag measured across 11 μm of the ab-face. Using the three-dimensional theory of Section 5.3 we can convert the phase to D_{ab}, shown in Figure 5.14. The diffusivity is fairly constant from room temperature down to about 100 K, at which point it rises rapidly. The small fluctuations that occur on a scale of one or two degrees are the result of the motion of the sample mount as discussed above.

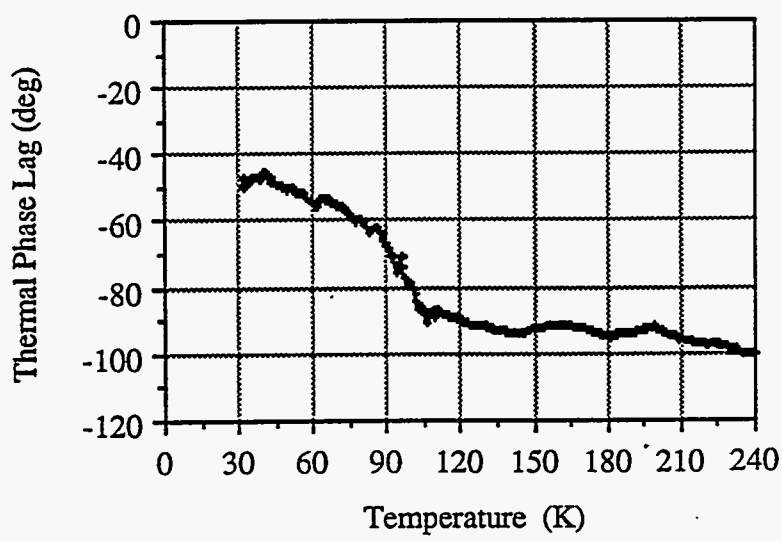

Figure 5.13 Thermal phase lag, as a function of temperature, along the Cu-O planes of an 88 K - phase Bi-Sr-Ca-Cu-O chip.

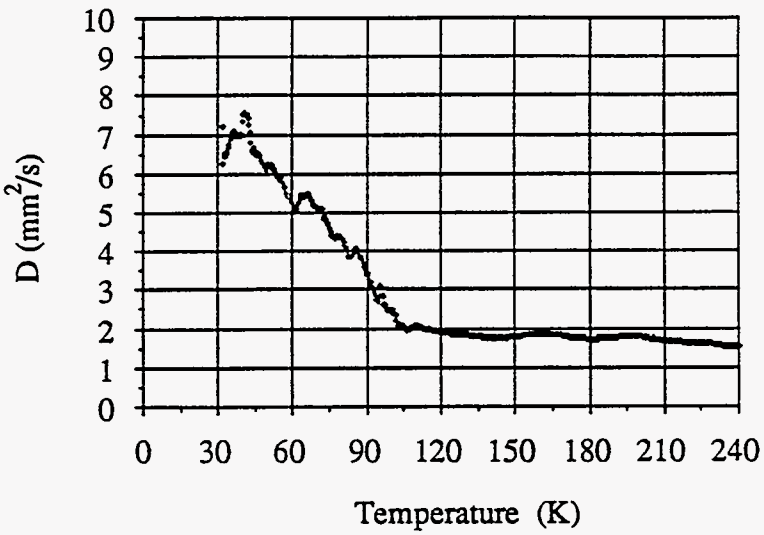

Figure 5.14 Thermal diffusivity, as a function of temperature, along the Cu-O planes of an 88 K - phase Bi-Sr-Ca-Cu-O chip.

To extract the thermal conductivity from this data, we need to know the heat capacity. Although in theory, the upper and lower frequency limits of the surface temperature can yield two independent measurements of κ and C (c.f. (2.9) and (2.30)), a photothermal determination of the heat capacity is impractical due to the poor signal-to-noise ratio, the complicated behavior of dR/dT, and the relatively weak, square-root dependence of the high-frequency data on C. Switching to a displacement method introduces another degree of freedom but, unfortunately, also introduces another unknown, namely the thermal expansion coefficient, $\alpha(T)$. Therefore we need to use heat capacity data determined by other means. We use the lattice values published by two independent research groups [13,14] which were in fairly good agreement. Higher temperature data (>110 K) were extrapolated from the low temperature results by fitting the curves with a weighted average of Debye and Einstein modes, as outlined in [14]. Since the heat capacity is a smooth

function of temperature (and a *scalar* quantity) the precise shape of the curve does not affect our conclusions about the existence of an enhancement. It does, however, determine to some degree the size and shape of the enhancement.

With this in mind, we present the thermal conductivity data in Figure 5.15. The data indicate a fairly strong enhancement below T_c. The size of the increase is stronger than that reported in most of the polycrystalline studies, as might be expected since our measurement is sensitive only to the heat flow in the superconducting direction. The scattering from grain boundaries and the mixture of crystal orientations in polycrystalline samples could moderate the effect.

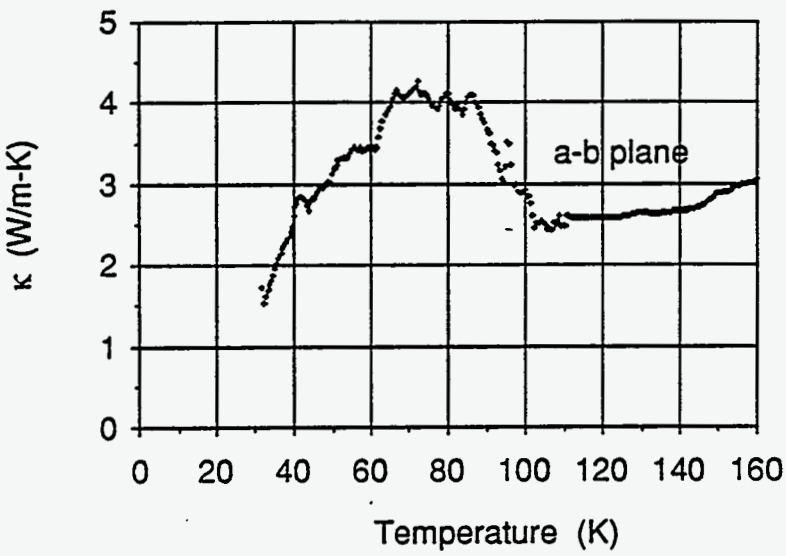

Figure 5.15 Thermal conductivity as determined from the diffusivity data of Figure 5.14 and published heat capacity curves [13,14].

Measurements on other Bi-Ca-Sr-Cu-O samples show varying amounts of enhancement. The 88K-T_c batch, measured above, exhibited pronounced enhancements (a second example is shown in Figure 5.16) while measurements on some of the lower T_c phases, as well as samples with visible signs of surface imperfections or contamination,

showed little or no effect. Since this measurement takes place in only a few cubic microns, it is essential to maintain the integrity of the sample and the vacuum throughout the experiment.

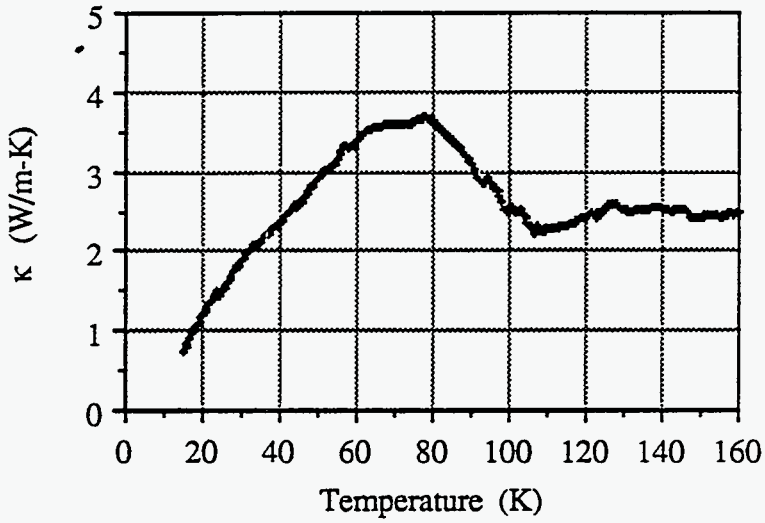

Figure 5.16 Thermal conductivity of the Cu-O planes measured on a second specimen from the same 88 Kelvin T_c batch as above.

To complete the anisotropy measurement on the 88 K T_c material, we embedded a sample in epoxy with the ac-plane exposed and mechanically polished it to optical smoothness. After careful examination under both our photothermal microscope and a polarized-light optical microscope, we isolated a small crack-free region in which to conduct the measurement at low temperature. In several runs, the thermal conductivity along the c-axis failed to show an enhancement below T_c, instead it decreased monotonically with temperature. We therefore conclude that the enhancement in the phonon mean free path is indeed limited to directions along the Cu-O planes, in accord with

the explanation put forth in Section 5.2. Figure 5.17 shows the full, anisotropic thermal conductivity of this material from 30 K to room temperature. To our knowledge, these results are the first reported measurements of the low-temperature anisotropic thermal conductivity in these materials.

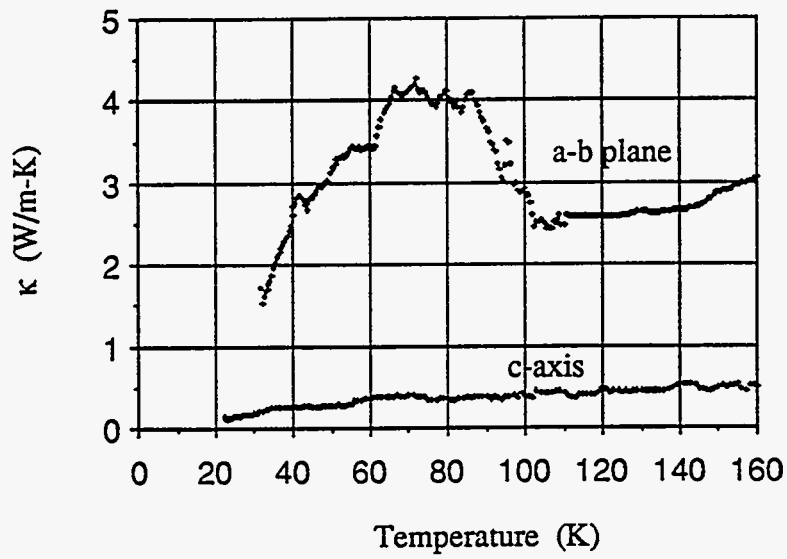

Figure 5.17 The anisotropic thermal conductivity of the 88 K - phase Bi material.

5.9 Behavior Above T_c

There remains a puzzling aspect of the thermal conductivity. The onset of the enhancement in the thermal conductivity seems to appear as much as 12 K *above* T_c. This surprising behavior is even more pronounced in the photothermal amplitude data, shown in Figure 5.18. Here we see an abrupt, 3-fold increase in the signal, beginning at least 12 K above T_c. The existence and location of the peak is the same in every measurement of this material.

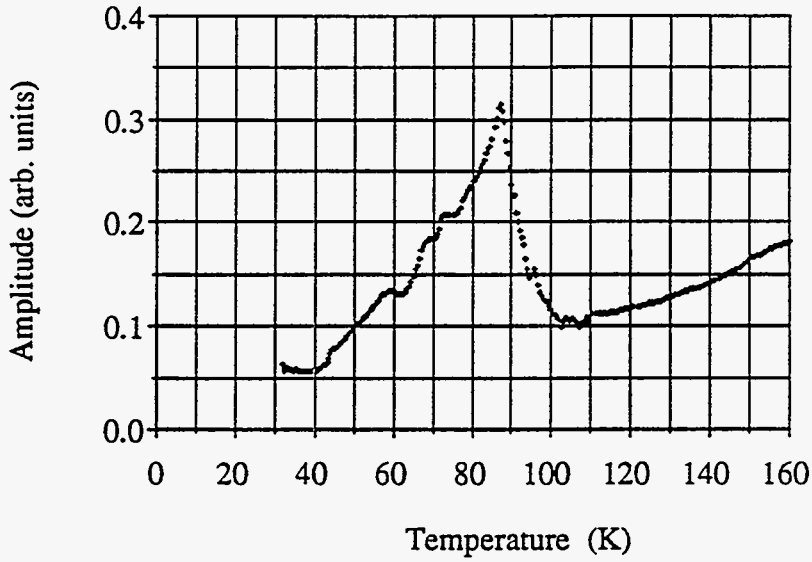

Figure 5.18 Amplitude of the photothermal signal, as a function of temperature, from the Cu-O planes of 88 K - phase Bi-Sr-Ca-Cu-O.

Unlike the phase, which depends only on D, the amplitude signal is a complicated function of D, κ_z, and dR/dT. We can reduce some of the complexity with the proper choice of operating conditions. Before we detail the behavior of these peaks, however, we should cite our experimental evidence that they are not artifacts of the measurement. We need to establish that they represent changes in the material itself (and not in its environment), and that the ambient temperature measurement is correct.

The primary concern, in a surface measurement such as this, is that the peaks may be caused by a condensation of one of the gases in the chamber. Operating at such a phase transition could alter the temperature profile since part of the input power would be consumed as latent heat. The reflectivity could be altered as well if the optical absorption of the condensate were great enough (although it is by no means obvious how such a film could give rise to the shape of the peaks we see). We repeated these measurements in a variety of ways to test the hypothesis that the ambient gas plays a role.

Since a gas will continue to condense once the temperature has dropped below its boiling point, the effects of the condensate should vary with the speed with which we conduct the experiment. Both the size and location of the peak, however, proved to be independent of the temperature sweep rate. Furthermore, the peaks were the same when measured during the initial cool-down and in a subsequent warm-up after a one hour rest at very low temperatures. We saw no signs of accumulation.

The most convincing evidence that the photothermal changes are linked to the sample, however, comes from the measurement of other phases of Bi-Sr-Ca-Cu-O. By testing samples with different transition temperatures we found that the peaks generally coincide with the superconducting transition. For example, Figure 5.19 shows the measurement on a 72K-phase chip. To date, we have found only one sample that showed no peak, shown in Figure 5.20; the photothermal amplitude changes abruptly at the transition temperature (about 80 K) but instead of increasing, the signal vanishes below the transition. It is unclear why this particular sample should behave so differently, but we include it here as a further demonstration that the peaks are sample-dependent.

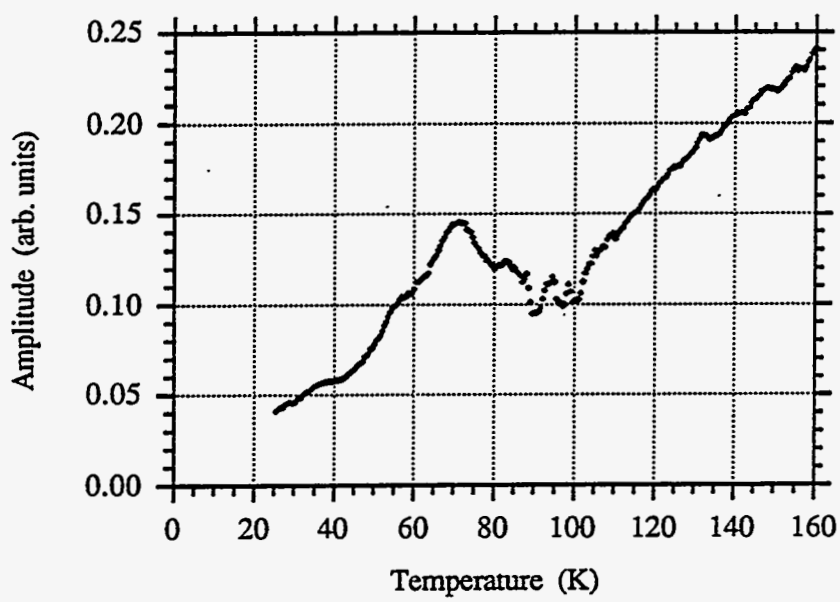

Figure 5.19 Amplitude of the photothermal signal from the Cu-O planes of an 72 K - phase Bi-Sr-Ca-Cu-O chip.

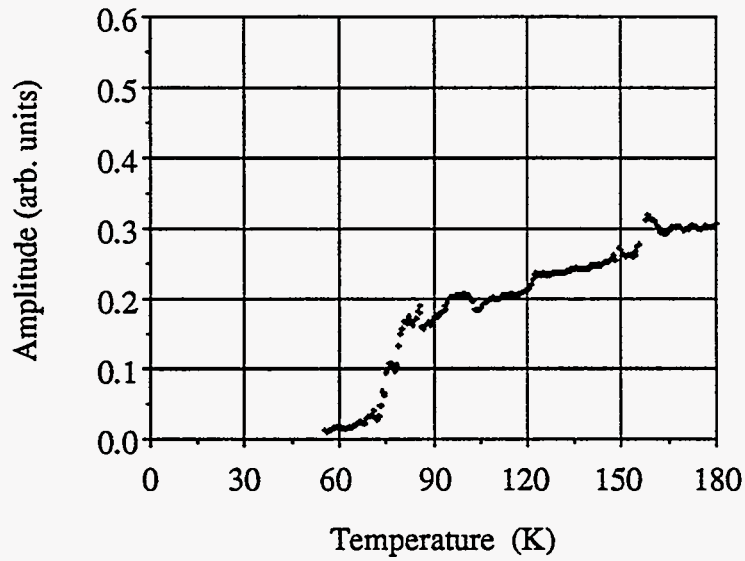

Figure 5.20 Amplitude of the photothermal signal from the Cu-O planes of an 80 K - phase Bi-Sr-Ca-Cu-O chip. This was the sole specimen that failed to exhibit a peak at T_c.

It remains to be shown that the thermometer is accurate and that the changes in the photothermal signal really do occur at the indicated temperatures. Note that if the photothermal changes actually were occurring below T_c, the surface temperature of the sample would have to be at least 12 K *cooler* than measured. However, all of the possible sources of discrepancy, such as blackbody radiation, excessive pump or probe power, or poor thermal contact to the sample mount, lead to errors in the wrong direction; they all tend to make the surface *hotter* than the bulk. Furthermore, we usually conduct the photothermal measurement during the cooling cycle so that any thermal lags of the sample or support structure would, again, cause the actual temperature to be higher than the readings.

Finally, any remaining doubt was removed by conducting a simultaneous measurement of the electrical resistivity and modulated reflectance. On the surface of a bismuth chip we deposited four gold films to be used as the leads in a four-point resistance measurement (see Figure 21). The heating and probe beams of the photothermal

experiment were focussed to the surface between the second and third leads, thereby assuring that the temperature was identical for the two measurements (or at least the photothermal measurement was not in a colder region). The results are plotted in Figure 5.21. Once again, the photothermal signal peaks at the transition temperature, with changes clearly beginning at least 10K above T_c. (The absolute measurement in this particular run is somewhat suspect due to the number of layers of electrical isolation and the heat leakage through the wires.)

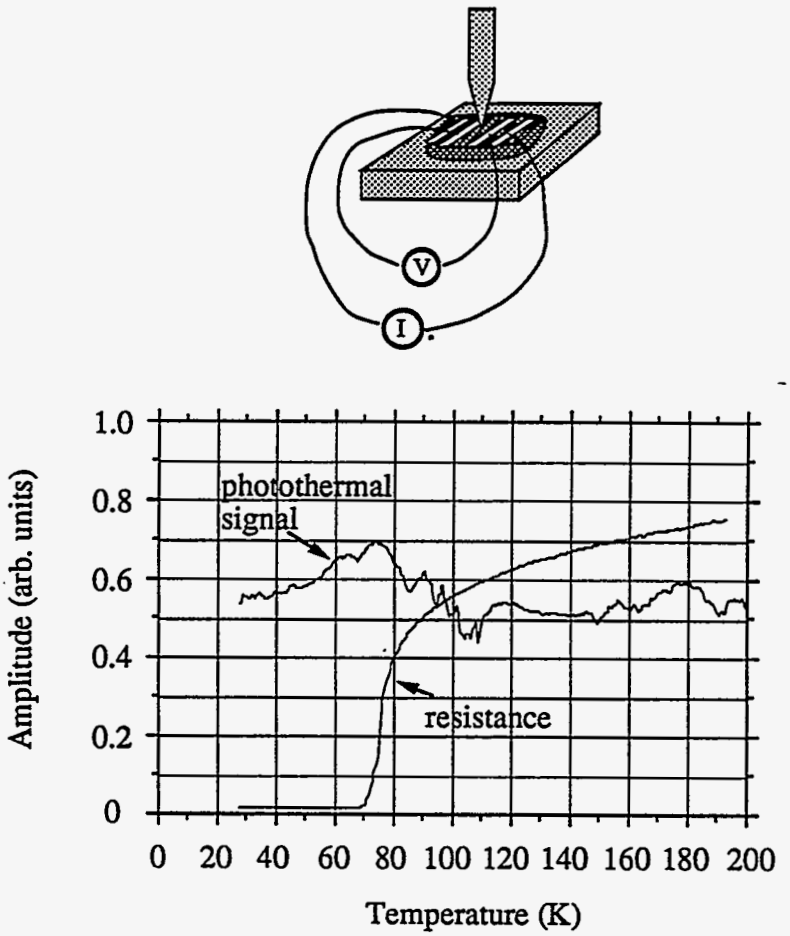

Figure 5.21 Simultaneous measurement of the resistivity and the photothermal amplitude.

Hence the peaks in the photothermal amplitude must represent changes in the samples themselves above T_c. We can further determine the cause by observing the low-frequency behavior. From (5.16) we know that the amplitude depends on three material quantities, the conductivity, the diffusivity, and dR/dT. For the point of discussion, consider the point-source approximation for the surface temperature when illuminating the ab-face of the material,

$$i_{sig} = \eta P_h P_p \frac{dR}{dT} \frac{1}{\kappa_c} e^{-(1+j)\sqrt{\omega/2D_{ab}}\, r} \tag{5.33}$$

Since the conductivity in the c-axis direction, κ_c, shows no abrupt changes at T_c, we can conclude that the peaks can only depend on D_{ab} and dR/dT. By making the two beams coincident (r=0) or by using an extremely low value for ω, we can also remove the dependence on D_{ab}. Under this condition we find that the peaks in the amplitude curve are still large; therefore we conclude that the peaks are predominantly due to a change in dR/dT. This conclusion is further supported by the observation of peaks in the c-axis measurements.

Note that these effects would not be visible in a simple measurement of the reflectivity. The photothermal signal is a differential signal, representing a minute change in the slope of the reflectivity as a function of temperature. While we cannot yet explain the physical origins of this effect, it should be emphasized that the actual change is very small, less than one part in 10^4. Even though the optical photon energy far exceeds the binding energy of the pairs, the rapid variation of the normal-electron density, as well as the pair density, with temperature below T_c could conceivably lead to changes of this order. The size of the peaks in the 88K-phase sample as well as the vanishing of the signal in the 80K-phase sample were found to be independent of the probe or pump wavelengths, ruling out optical resonance phenomena as the cause.

It should also be noted that while the behavior is quite consistent within samples from the same batch, there is some variation in the magnitude of the peak between batches. Furthermore, those batches that exhibit the strongest change in dR/dT also tend to show the strongest enhancement in the thermal conductivity, although some degree of amplitude change is seen even in the complete absence of a detectable conductivity enhancement. Since the area of the probe spot is highly localized, it is possible that the amplitude could respond to the transition in cases where structural flaws or inhomogeneities of the material mask the thermal conductivity enhancement over the course of the 10 to 15 μm of propagation in the phase measurement.

The reason for the onset of photothermal changes above T_c is still unknown, but there is evidence for high-temperature changes in other types of measurements. Both the magnetic susceptibility and the resistivity of these materials can depart from that of a normal material at temperatures well above T_c. For example, the resistivity curve in Figure 5.21 departs from a normal, linear behavior at about the same temperature where photothermal changes begin. This "excess conductivity" has been studied in Y-Ba-Cu-O compounds by other groups in an attempt to determine the dimensionality of the superconductivity in these materials [15,16].

A likely cause for these effects is thermodynamic fluctuations. Due to thermal fluctuations in the macroscopic wavefunction, Ψ, there is a finite probability of pairing at temperatures above T_c. In Ref. 17, it was shown that the critical temperature range, $|T - T_c|$, where the fluctuations are significant ($\langle(\delta\Psi)^2\rangle$ greater than $\langle|\Psi|^2\rangle$) varies inversely with the coherence length, with the precise relation depending on the dimensionality and the impurity content of the superconductor. For conventional superconductors, which have coherence lengths on the order of 100 Å to 1000 Å, millions of pairs overlap, and the statistical significance of fluctuations is minor. The critical temperature range is between 10^{-7} to 10^{-14} T_c. However, it was shown that the critical regions in these two-dimensional

superconductors, which have coherence lengths on the order of 15 Å in the ab-plane and 2 to 3 Å along the c-axis, can be a significant fraction of T_c.

Since these fluctuations can occur over a large temperature range they may be the cause of the high-temperature photothermal behavior. A small amount of pairing above T_c could result in an enhancement of the thermal conductivity through the same process already hypothesized, although it is unclear why these effects do not appear in the polycrystalline Y-Ba-Cu-O data. Subsequent examinations of more samples may reveal a material or processing dependence.

These fluctuations could also be the source for the dR/dT changes above T_c. Currently, work is underway on an assortment of samples which exhibit varying amounts of non-linear magnetic and electric behavior above T_c to determine if these effects correlate with the onset of the photothermal amplitude peak.

5.10 Suggestions for Future Research

Our studies of the high-temperature superconductors are just a beginning. While we have measured a large enhancement in the thermal conductivity below T_c and even larger changes in the modulated reflectance, further research is needed to determine the source of this behavior. The reflectivity variations are particularly interesting since they were unexpected and since they may be strong enough to serve as a contrast mechanism in the imaging of inhomogeneous materials.

To begin with, the sample-drift problem needs to be addressed. The current experimental procedure, whereby the focus is manually adjusted using the projection system as the feedback, is tedious and prone to errors. As of this writing an automatic focussing system is being added to the microscope. This will remove the ripple in the data caused by the manual adjustments. The sample may still drift laterally, but since the samples are homogeneous over tens, or even hundreds, of microns, this is a lesser

problem. If necessary, the lateral drift can be corrected using a CCD camera and an edge-location technique in conjunction with the mechanical scanner.

Another weak link in our conductivity measurement is the reliance on published values of the heat capacity. Before we undertake a quantitative analysis of the enhancement, we should have heat capacity data for the same sample. Currently, Kapitulnik and Ryu [18] are conducting thermal measurements on single-crystal materials using miniature thermocouples and heaters. These should provide the information we need.

The origins of the photothermal amplitude changes at T_c are still unknown but are likely due to the strong derivatives in the normal and superconducting carrier densities below T_c. It would be interesting to study the behavior of the amplitude as the sample is driven normal by a large magnetic field. The early onset of the photothermal peak, as well as the thermal conductivity, could be a result and thermodynamic fluctuations in the wavefunctions. If so, we have discovered a sensitive means for measuring these effects. As mentioned in the preceding section, studies are currently underway to determine if the early onset of the photothermal changes is related to high-temperature anomalies in the resistivity or magnetics susceptibility.

Finally, we have yet to capitalize on our imaging capabilities at low temperatures. Room temperature images of polycrystalline Y-Ba-Cu-O films showed that the photothermal amplitude varies enormously between individual crystallites. A sequence of such images near T_c should reveal the different phases present in the material. The same measurements could also be made on samples believed to be single-crystal to test for irregularities. If the measurements are extended to include the efforts of external fields and currents, the possibilities of imaging inhomogeneities grows further.

Chapter 5 References

1. C. Uher and A. B. Kaiser, "Thermal transport properties of $YBa_2Cu_3O_7$ superconductors," *Phys. Rev. B* **36** (10), 5680 (1987).
2. D.T. Mirelli, J. Heremans, and D.E. Swets, "Thermal conductivity of superconductive Y-Ba-Cu-O," *Phys. Rev.* B **36** (7), 3917 (1987).
3. C. Uher and W.-H. Huang, "Thermoelectric power and thermal conductivity of neutron-irradiated $YBa_2Cu_3O_{7-\delta}$," *Phys. Rev. B* **40** (4), 2694 (1989).
4. L. Tewordt and Th. Wölkhausen, "Theory of thermal conductivity of the lattice for high-T_c superconductors," *Solid State Comm.* **70** (8), 839 (1989).
5. J. Bardeen, G. Rickayzen, and L. Tewordt, "Theory of the Thermal Conductivity of Superconductors," *Phys. Rev.* **113** (4), 982 (1959).
6. C. Kittel, *Introduction to Solid State Physics, 5th Ed.*, New York: John Wiley & Sons, 1976 (p. 143).
7. Dwight E. Gray, Ed. *American Institute of Physics Handbook, 3rd Ed.*, New York: McGraw-Hill, Inc., 1972 (4:158).
8. D.B. Mitzi, L.W. Lombardo, A. Kapitulnik, S.S. Laderman, and R.D. Jacowitz, "Growth and properties of oxygen- and ion-doped $Bi_2Sr_2CaCu_2O_{8+\delta}$ single crystals," *Phys. Rev. B* **41** (10), 6564 (1990).
9. R.S. Feigelson, D. Gazit, D.K. Fork, and T.H. Geballe, "Superconducting Bi-Ca-Sr-Cu-O fibers grown by the laser-heated pedestal growth technique," *Science* **240**, 1642 (1988).
10. J.H. Kim, I. Bozovic, D.B. Mitzi, A. Kapitulnik, and J.S. Harris, Jr., "Optical Anisotropy of $Bi_2Sr_2CaCu_2O_8$," *Phys. Rev. B* **41** (10), 7251 (1990).
11. Neil W. Ashcroft and N. David Mermin, *Solid State Physics*, Philadelphia: Holt, Rinehart and Winston, 1976 (p. 463).

12. C.M. Van Atta, *Vacuum Science and Engineering*, New York: McGraw-Hill, Inc., (1965).

13. R. A. Fisher et al, "Specific heat measurements on superconducting Bi-Ca-Sr-Cu and Tl-Ca-Ba-Cu oxides: Absence of a linear term in the specific heat of Bi-Ca-Sr-Cu oxides," *Phys. Rev. B.* **38** (16), 11942 (1988).

14. Daniel Eckert, *Chaleur Specifique a Basse Temperature des Oxydes Supraconducteurs a Haute Temperature Critique* $YBa_2Cu_3O_{7-\delta}$, $Bi_2CaSr_2Cu_2O_8$, $Tl_2CaBa_2Cu_2O_8$, *et de Quelque Phases Voisines*, Ph.D. dissertation, University of Geneva, 1989.

15. P.P. Freitas et al, "Thermodynamic fluctuations in the superconductor $Y_1Ba_2Cu_3O_{9-\delta}$: Evidence for three-dimensional superconductivity," *Phys. Rev. B* **36** (1), 833 (1987).

16. M. Ausloos and Ch. Laurent, "Thermodynamic fluctuations in the superconductor $Y_1Ba_2Cu_3O_{9-y}$: Evidence for two-dimensional superconductivity," *Phys. Rev. B* **37** (4), 611 (1988).

17. Aharon Kapitulnik, M.R. Beasley, C. Castellani, and C. Di Castro, "Thermodynamic fluctuations in the high-T_c perovskite superconductors," *Phys. Rev. B* **37** (1), 537 (1988).

18. A. Kapitulnik and S. Ryu, private communication.

Appendix

Numerical Evaluation of the Temperature and Displacement Profiles

The photothermal theory of Chapter 2 and Chapter 5 led to transform relations for the temperature and surface displacement of a semi-infinite medium heated by a local, periodic source. This appendix will discuss some of the issues involved when evaluating these expressions numerically. The discussion will be limited to Cartesian formulas of Chapter 5; the simpler cylindrically symmetric formulas of Chapter 2 are solved in a similar fashion with the exception that they involve one-dimensional Hankel transforms rather than two-dimensional Fourier transforms.

The equations to be evaluated are

$$\theta(x,y,0) \sim \int_{-\infty}^{\infty} \frac{H_x(s)\, H_y(p)}{\sqrt{k_t^2 + (2\pi s)^2 + (2\pi p)^2}}\, e^{-j2\pi x s}\, e^{-j2\pi y p}\, ds\, dp \tag{A.1}$$

$$u_z(x,y,0) \sim \int_{-\infty}^{\infty} \frac{H_x(s)\, H_y(p)}{k_t^2 + (2\pi s)^2 + (2\pi p)^2}\, e^{-j2\pi x s}\, e^{-j2\pi y p}\, ds\, dp \tag{A.2}$$

where H_x and H_y are the x and y spatial Fourier transforms of the heating beam profile (the heating profile is assumed to be separable in x and y as it is with, for example, Gaussian sources). If the sample is homogeneous, H_x and H_y are usually treated as Gaussian and the appropriate analytic expressions are substituted into the integrals. When analyzing the profile near a vertical crack, the crack is assumed to run in the y-direction so that only H_x is

affected. H_x is found by taking a Fast Fourier Transform (FFT) of the truncated Gaussian profile added to its image, as shown in Figure A.1.

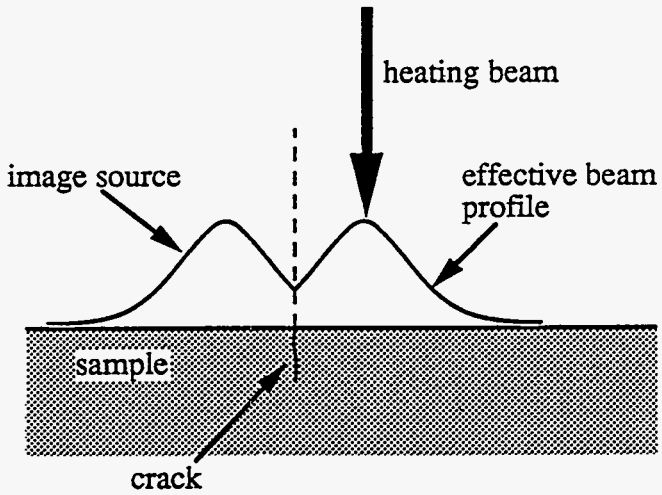

Figure A.1 Cross section of the effective beam profile for heating near a thermally-insulating crack. The profile in the y-direction is Gaussian.

Having obtained H_x and H_y, the temperature and displacement profiles can, in principle, be obtained from a simple two-dimensional FFT of the integrand. However, there is a major drawback to this approach - the number of sample points needed for an accurate transform can be prohibitively large. To avoid aliasing, the sample points in an FFT must cover the entire finite ranges in both the space and the spatial frequency domains, as shown for one dimension in Figure A.2. From the figure it is apparent that the number of sample points we need is

$$N \geq \frac{W_x}{\Delta x} = W_x W_s \tag{A.3}$$

where W_x and W_s are the full widths of the temperature (or displacement) profile and its transform. For a Gaussian beam, W_s is determined by the exponential term, $e^{-(\pi r_h s)^2}$, in $H_x(s)$ where r_h is the radius of the heating spot (see (5.16)). Therefore, $W_s \cong 6/\pi r_h$.

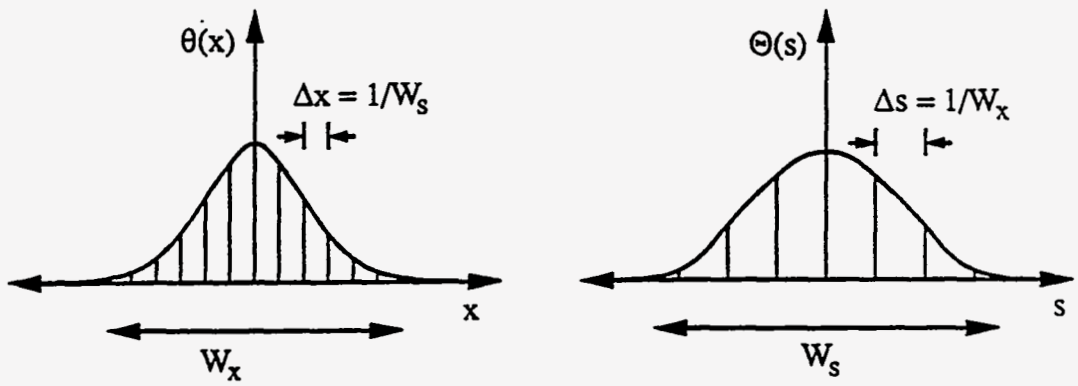

Figure A.2 The space and the spatial frequency domains involved in the transform expressions. The minimum number of sample points is determined by the widths of both domains.

At high frequencies ($k_t r_h > 1$) the temperature and displacement profiles are only slightly wider than the spot radius. Thus the minimum number of points we need is about

$$N \geq 60/\pi \cong 20 \text{ points.} \qquad \text{(high-frequency regime)} \qquad (A.4)$$

Since the total number of points needed in the two-dimensional FFT is N^2, this approach will work quite well in the high-frequency regime. Trouble occurs, however, whenever $k_t r_h < 1$ as in the work on high-T_c superconductors. In this case the profiles in the spatial domain and the spatial frequency domain have greatly differing widths and N gets quite large. For example, if the frequency is low enough, the temperature and displacement profiles have a $1/x$ dependence which has tails that extend far beyond those of a Gaussian. The spatial extent is determined not by the spot size but by the exponential decay of the

thermal wave. Since the amplitude of the thermal wave decays as $e^{-|k_t|r_h/\sqrt{2}}$, $W_x \cong 20/k_t$. Thus the condition for N is

$$N \geq \frac{40}{k_t r_h} . \qquad \text{(low-frequency regime)} \qquad (A.5)$$

In calculations where the thermal wavelength is longer than a few spot widths, the number of points in the two-dimensional FFT can approach 10^5 or even 10^6.

To accelerate the computations, we can sacrifice some of the generality of our solution. We are usually interested in the temperature profile along one axis. For example, we characterize anisotropic media by separating the heating and probe beams along each crystal axis in three separate experiments. By defining the line joining the heating and probe beams as our x-axis, we can set y to zero. Thus our transform relation takes the form

$$\theta(x,y,0) \sim \int_{-\infty}^{\infty} H_x(s)\, e^{-j2\pi x s} \int_{-\infty}^{\infty} \frac{H_y(p)}{\sqrt{k_t^2 + (2\pi s)^2 + (2\pi p)^2}}\, dp \quad ds \qquad (A.6)$$

With the removal of the $e^{-2j\pi py}$ term, the integrand in the p-domain becomes smooth and standard integration routines can be used. The solution is then completed with a *one*-dimensional FFT over the s-domain. The advantage to this approach is that routines designed for integration can use far fewer points that what was required for the FFT. A further advantage is that the p-integrals need only be evaluated once at any given frequency. Afterwards, the temperature or displacement profiles can be evaluated quickly for successive values of H_x (for example, as the beam is scanned towards a crack).

92 JUL 17 PM 2:32